NASA/CR-1998-208698

Input Shaping to Reduce Solar Array Structural Vibrations

Michael J. Doherty and Robert H. Tolson
Joint Institute for Advancement of Flight Sciences
The George Washington University
Langley Research Center, Hampton, Virginia

August 1998

The NASA STI Program Office ... in Profile

Since its founding, NASA has been dedicated to the advancement of aeronautics and space science. The NASA Scientific and Technical Information (STI) Program Office plays a key part in helping NASA maintain this important role.

The NASA STI Program Office is operated by Langley Research Center, the lead center for NASA's scientific and technical information. The NASA STI Program Office provides access to the NASA STI Database, the largest collection of aeronautical and space science STI in the world. The Program Office is also NASA's institutional mechanism for disseminating the results of its research and development activities. These results are published by NASA in the NASA STI Report Series, which includes the following report types:

- TECHNICAL PUBLICATION. Reports of completed research or a major significant phase of research that present the results of NASA programs and include extensive data or theoretical analysis. Includes compilations of significant scientific and technical data and information deemed to be of continuing reference value. NASA counter-part of peer reviewed formal professional papers, but having less stringent limitations on manuscript length and extent of graphic presentations.

- TECHNICAL MEMORANDUM. Scientific and technical findings that are preliminary or of specialized interest, e.g., quick release reports, working papers, and bibliographies that contain minimal annotation. Does not contain extensive analysis.

- CONTRACTOR REPORT. Scientific and technical findings by NASA-sponsored contractors and grantees.

- CONFERENCE PUBLICATION. Collected papers from scientific and technical conferences, symposia, seminars, or other meetings sponsored or co-sponsored by NASA.

- SPECIAL PUBLICATION. Scientific, technical, or historical information from NASA programs, projects, and missions, often concerned with subjects having substantial public interest.

- TECHNICAL TRANSLATION. English-language translations of foreign scientific and technical material pertinent to NASA's mission.

Specialized services that help round out the STI Program Office's diverse offerings include creating custom thesauri, building customized databases, organizing and publishing research results ... even providing videos.

For more information about the NASA STI Program Office, see the following:

- Access the NASA STI Program Home Page at ***http://www.sti.nasa.gov***

- E-mail your question via the Internet to help@sti.nasa.gov

- Fax your question to the NASA Access Help Desk at (301) 621-0134

- Phone the NASA Access Help Desk at (301) 621-0390

- Write to:
  NASA Access Help Desk
  NASA Center for AeroSpace Information
  7121 Standard Drive
  Hanover, MD 21076-1320

NASA/CR-1998-208698

Input Shaping to Reduce Solar Array Structural Vibrations

Michael J. Doherty and Robert H. Tolson
Joint Institute for Advancement of Flight Sciences
The George Washington University
Langley Research Center, Hampton, Virginia

National Aeronautics and
Space Administration

Langley Research Center
Hampton, Virginia 23681-2199

Prepared for Langley Research Center
under Cooperative Agreement NCC1-104

August 1998

Available from the following:

NASA Center for AeroSpace Information (CASI)
7121 Standard Drive
Hanover, MD 21076-1320
(301) 621-0390

National Technical Information Service (NTIS)
5285 Port Royal Road
Springfield, VA 22161-2171
(703) 487-4650

Abstract

Structural vibrations induced by actuators can be minimized through the effective use of feedforward input shaping. Actuator commands are convolved with an input shaping function to yield an equivalent *shaped* set of actuator commands. The shaped commands are designed to achieve the desired maneuver and minimize the residual structural vibrations.

Input shaping was extended for stepper motor actuators through this research. An input-shaping technique based on pole-zero cancellation was used to modify the Solar Array Drive Assembly (SADA) stepper motor commands for the NASA/TRW Lewis satellite. A series of impulses were calculated as the ideal SADA output for vibration control and were then discretized for use by the SADA actuator. Simulated actuator torques were used to calculate the linear structural response and resulted in residual vibrations that were below the magnitude of baseline cases.

The effectiveness of input shaping is limited by the accuracy of the modal identification of the structural system. Controller robustness to identification errors was improved by incorporating additional zeros in the input shaping transfer function. The additional shaper zeros did not require any increased performance from the actuator or controller, and the resulting feedforward controller reduced residual vibrations to the level of the exactly modeled input shaper despite the identification errors.

Table of Contents

ABSTRACT ____ iii

TABLE OF CONTENTS ____ iv

LIST OF FIGURES ____ vi

LIST OF TABLES ____ x

NOMENCLATURE ____ xi

1 INTRODUCTION ____ 1

1.1 POLE-ZERO CANCELLATION THEORY 2

1.2 EXAMPLE OF STRUCTURAL VIBRATION CONTROL: THE LEWIS SPACECRAFT 2

1.3 OVERVIEW OF RESULTS 3

2 POLE-ZERO CANCELLATION VIBRATION CONTROL THEORY ____ 6

2.1 DISCRETE TIME SYSTEM DESCRIPTION 6

2.2 ROBUSTNESS AND MULTIPLE-MODE CONSIDERATIONS 8

2.3 TIME DOMAIN IMPLEMENTATION 11

2.4 EXTENSION OF POLE-ZERO CANCELLATION FOR STEPPER MOTORS 12

2.5 SELECTION AND IMPLEMENTATION OF VIBRATION CONTROL SEQUENCES 13

3 EXAMPLE OF STRUCTURAL VIBRATION CONTROL ____ 17

3.1 OVERVIEW OF LEWIS SPACECRAFT 17

3.2 LEWIS SPACECRAFT DYNAMIC MODEL 29

3.3 DETERMINATION OF TARGET MODES 33

4 SIMULATIONS AND RESULTS 42

4.1 JITTER ANALYSIS METHOD 42

4.2 BASELINE SIMULATIONS AND JITTER ANALYSIS RESULTS 46

4.3 SHAPED INPUT SIMULATIONS AND RESULTS 57

4.4 SUMMARY OF RESULTS 79

5 CONCLUSIONS 82

5.1 CURRENT RESULTS 82

5.2 RECOMMENDATIONS FOR FUTURE RESEARCH 83

REFERENCES 86

APPENDIX A: STEPPER MOTOR DESCRIPTION 88

APPENDIX B: MODAL FREQUENCIES OF LEWIS FINITE ELEMENT MODEL 95

APPENDIX C: COMPARISON OF JITTER ANALYSIS RESULTS 97

List of Figures

FIGURE 2.1: SYSTEM BLOCK DIAGRAM 6

FIGURE 2.2: EXAMPLE SYSTEM POLES IN THE *Z*-PLANE 9

FIGURE 2.3: EXAMPLE SYSTEM POLES AND SHAPER ZEROS IN THE *Z*-PLANE 10

FIGURE 2.4: EXAMPLE IMPULSE AMPLITUDES 12

FIGURE 2.5: EXAMPLE IMPULSE AMPLITUDES AND STEP SEQUENCE APPROXIMATIONS 13

FIGURE 2.6: EXAMPLE TIME –ADJUSTED STEP SEQUENCE APPROXIMATIONS 13

FIGURE 3.1: LEWIS SPACECRAFT 17

FIGURE 3.2: LEWIS SPACECRAFT ORBITAL OPERATIONS 18

FIGURE 3.3: SPACECRAFT DIMENSIONS (INCHES) 21

FIGURE 3.4: PAYLOAD INSTRUMENT MODULE PLAN VIEW 22

FIGURE 3.5: SOLAR ARRAY WING ISOMETRIC VIEW 24

FIGURE 3.6: TYPE 2 STEPPER MOTOR CUT-AWAY VIEW 25

FIGURE 3.7: TYPE 2 STEPPER MOTOR EXTERNAL VIEW 26

FIGURE 3.8: FOUR-DOF STEPPER MOTOR MODEL DIAGRAM 31

FIGURE 3.9: MOTOR STEPPING OPERATION PARAMETERS 32

FIGURE 3.10: SADA #1 *Y*-ROTATION (INPUT) – HSI *X*-ROTATION (OUTPUT) FRF 36

FIGURE 3.11: SADA #1 *Y*-ROTATION – HSI *X*-ROTATION RANKED MODES (1) 37

FIGURE 3.12: SADA #1 *Y*-ROTATION – HSI *X*-ROTATION RANKED MODES (2) 38

FIGURE 3.13: PAYLOAD INSTRUMENT *X*-ROTATION FRF MAGNITUDES 39

FIGURE 3.14: PAYLOAD INSTRUMENT *Y*-ROTATION FRF MAGNITUDES 41

FIGURE 4.1: JITTER ANALYSIS EXAMPLE (1) 44

FIGURE 4.2: JITTER ANALYSIS EXAMPLE (2) 44

FIGURE 4.3: SINGLE STEP TORQUE TIME PROFILE 48

FIGURE 4.4: CSRS TORQUE TIME PROFILE, 3.16 PPS 48

FIGURE 4.5: HSI *X*-ROTATION RESPONSE TO CSRS TORQUE INPUT 49

FIGURE 4.6: HSI *Y*-ROTATION RESPONSE TO CSRS TORQUE INPUT 50

FIGURE 4.7: MATS TORQUE TIME PROFILE, 200 PPS 52

FIGURE 4.8: HSI *X*-ROTATION RESPONSE TO MATS TORQUE INPUT 53

FIGURE 4.9: HSI *Y*-ROTATION RESPONSE TO MATS TORQUE INPUT 54

FIGURE 4.10: HSI *X*-ROTATION BASELINE JITTER LEVELS 55

FIGURE 4.11: LEISA *X*-ROTATION BASELINE JITTER LEVELS 55

FIGURE 4.12: HSI *Y*-ROTATION BASELINE JITTER LEVELS 56

FIGURE 4.13: LEISA *Y*-ROTATION BASELINE JITTER LEVELS 56

FIGURE 4.14: SYSTEM POLES IN THE *Z*-PLANE (*T*=1.14 SECONDS) 61

FIGURE 4.15: SADA TORQUE TIME PROFILE FOR VCS #1 62

FIGURE 4.16: HSI *X*-ROTATION RESPONSE TO VCS #1 63

FIGURE 4.17: HSI *Y*-ROTATION RESPONSE TO VCS #1 64

FIGURE 4.18: HSI *X*-ROTATION JITTER ANALYSIS RESULTS (3.5-SECOND WINDOW) 67

FIGURE 4.19: LEISA *X*-ROTATION JITTER ANALYSIS RESULTS (3.5-SECOND WINDOW) 68

FIGURE 4.20: HSI *Y*-ROTATION JITTER ANALYSIS RESULTS (3.5-SECOND WINDOW) 69

FIGURE 4.21: LEISA *Y*-ROTATION JITTER ANALYSIS RESULTS (3.5-SECOND WINDOW) 70

FIGURE 4.22: SYSTEM POLES AND VCS #2 ZEROS IN THE *Z*-PLANE (*T*=1.035 SECONDS) 73

FIGURE 4.23: HSI *X*-ROTATION JITTER ANALYSIS RESULTS (3.5-SECOND WINDOW) 74

FIGURE 4.24: LEISA *X*-ROTATION JITTER ANALYSIS RESULTS (3.5-SECOND WINDOW) 75

FIGURE 4.25: HSI *Y*-ROTATION JITTER ANALYSIS RESULTS (3.5-SECOND WINDOW) 76

FIGURE 4.26: LEISA *Y*-ROTATION JITTER ANALYSIS RESULTS (3.5-SECOND WINDOW) 77

FIGURE A.1: DETENT AND STATE #1 TORQUES VS. ROTOR ELECTRICAL ANGLE 90

FIGURE A.2: COMPOSITE TORQUE VS. ROTOR ELECTRICAL ANGLE 91

FIGURE A.3: DETENT, STATES #1, #2, AND #3 TORQUES VS. ROTOR ELECTRICAL ANGLE 93

FIGURE C.1: HSI *X*-ROTATION JITTER LEVELS (0.05 SECOND WINDOW) 98

FIGURE C.2: LEISA *X*-ROTATION JITTER LEVELS (0.05 SECOND WINDOW) 99

FIGURE C.3: HSI *X*-ROTATION JITTER LEVELS (0.1 SECOND WINDOW) 100

FIGURE C.4: LEISA *X*-ROTATION JITTER LEVELS (0.1 SECOND WINDOW) 101

FIGURE C.5: HSI *X*-ROTATION JITTER LEVELS (0.2 SECOND WINDOW) 102

FIGURE C.6: LEISA *X*-ROTATION JITTER LEVELS (0.2 SECOND WINDOW) 103

FIGURE C.7: HSI *X*-ROTATION JITTER LEVELS (0.5 SECOND WINDOW) 104

FIGURE C.8: LEISA *X*-ROTATION JITTER LEVELS (0.5 SECOND WINDOW) 105

FIGURE C.9: HSI *X*-ROTATION JITTER LEVELS (1 SECOND WINDOW) 106

FIGURE C.10: LEISA *X*-ROTATION JITTER LEVELS (1 SECOND WINDOW) 107

FIGURE C.11: HSI *X*-ROTATION JITTER LEVELS (3.5 SECOND WINDOW) 108

FIGURE C.12: LEISA *X*-ROTATION JITTER LEVELS (3.5 SECOND WINDOW) 109

FIGURE C.13: HSI *Y*-ROTATION JITTER LEVELS (0.05 SECOND WINDOW) 110

FIGURE C.14: LEISA *Y*-ROTATION JITTER LEVELS (0.05 SECOND WINDOW) 111

FIGURE C.15: HSI *Y*-ROTATION JITTER LEVELS (0.1 SECOND WINDOW) 112

FIGURE C.16: LEISA *Y*-ROTATION JITTER LEVELS (0.1 SECOND WINDOW) 113

FIGURE C.17: HSI *Y*-ROTATION JITTER LEVELS (0.2 SECOND WINDOW) 114

FIGURE C.18: LEISA *Y*-ROTATION JITTER LEVELS (0.2 SECOND WINDOW) 115

FIGURE C.19: HSI *Y*-ROTATION JITTER LEVELS (0.5 SECOND WINDOW) 116

FIGURE C.20: LEISA *Y*-ROTATION JITTER LEVELS (0.5 SECOND WINDOW) 117

FIGURE C.21: HSI *Y*-ROTATION JITTER LEVELS (1 SECOND WINDOW) 118

FIGURE C.22: LEISA *Y*-ROTATION JITTER LEVELS (1 SECOND WINDOW) 119

FIGURE C.23: HSI *Y*-ROTATION JITTER LEVELS (3.5 SECOND WINDOW) 120

FIGURE C.24: LEISA *Y*-ROTATION JITTER LEVELS (3.5 SECOND WINDOW) 121

List of Tables

TABLE 3.1: PAYLOAD INSTRUMENT MISSION REQUIREMENTS 19

TABLE 3.2: LEWIS SPACECRAFT PHYSICAL QUANTITIES 20

TABLE 3.3: TYPE 2 STEPPER MOTOR SPECIFICATIONS 23

TABLE 3.4: STEPPER MOTOR MODEL MECHANICAL SPECIFICATIONS 31

TABLE 3.5: STEPPER MOTOR MODEL ELECTRICAL SPECIFICATIONS 32

TABLE 3.6: RANKED MODES FOR PAYLOAD INSTRUMENT *X*-ROTATIONS 39

TABLE 3.7: RANKED MODES FOR PAYLOAD INSTRUMENT *Y*-ROTATIONS 40

TABLE 4.1: EFFECT OF JITTER WINDOWS ON MODAL CONTRIBUTIONS 45

TABLE 4.2: CSRS JITTER ANALYSIS RESULTS 51

TABLE 4.3: VIBRATION CONTROL SEQUENCE #1 DATA 60

TABLE 4.4: VIBRATION CONTROL SEQUENCE #2 DATA 72

TABLE 4.5: VIBRATION CONTROL SEQUENCE #3 DATA 80

Nomenclature

I_{ii}^{bus}	spacecraft bus moment of inertia about i^{th} Cartesian axis
I_{ii}^{SA}	solar array moment of inertia about i^{th} Cartesian axis
ω_{max}^{motor}	maximum SADA step rate
$\Delta\theta_{step}^{bus}$	spacecraft bus step angle
$\Delta\theta_{step}^{SA}$	solar array step angle
$\Delta\theta_{sim}^{bus}$	spacecraft bus inertial rotation over the course of a simulation
$\Delta\theta_{sim}^{SA}$	solar array inertial rotation over the course of a simulation
$\Delta\theta_{sim}^{s/c}$	combined spacecraft bus and solar array inertial rotation during a simulation
$\omega_{tracking}^{SA}$	solar array inertial angular rate for solar tracking
$\omega_{tracking}^{motor}$	SADA step rate for solar tracking
$\omega_{tracking}^{s/c}$	combined spacecraft bus and solar array inertial angular rate for solar tracking
ω_n	undamped natural frequency
ω_d	damped natural frequency
$\bar{\theta}_e$	SADA rotor electrical angle at equilibrium for an arbitrary electrical state
$E_{rounding}^{sum}$	summation of impulse amplitude to step sequence rounding errors
$E_{rounding}^{max}$	maximum of impulse amplitude to step sequence rounding errors
$E_{variation}^{sum}$	summation of impulse amplitude variation errors
$E_{variation}^{max}$	maximum of impulse amplitude variation errors
ζ	damping ratio
θ	angular displacement
ω	angular velocity
ω	frequency domain variable
$\Delta\theta_r$	SADA rotor step angle
$\Delta\theta_{SA}$	SADA output shaft step angle
$\delta(t)$	Dirac delta function
ω^{bus}	spacecraft bus inertial angular rate
θ_e	SADA rotor electrical angle
ϕ_{ir}	i^{th} FEM node, r^{th} modeshape coefficient
θ_m	SADA rotor mechanical angle
ω_{nr}	natural frequency of rth mode
ζ_r	damping ratio of rth mode
ω^{SA}	solar array inertial angular rate
ACS	Attitude Control System

C	damping coefficient
C_e	SADA motor torque function electrical constant
C_m	SADA motor torque function mechanical constant
CSRS	Constant Step Rate Sequence
FEM	Finite Element Method
FRF	Frequency Response Function
GR	harmonic drive ratio (gear reduction)
$H(s)$	continuous time domain transfer function H
$H(z)$	discrete time domain transfer function H
$H_{ij}(\omega)$	frequency response function
HSI	Hyper Spectral Imager
I_r	SADA rotor moment of inertia
j	imaginary quantity $\sqrt{-1}$
J	moment of inertia coefficient
K	stiffness coefficient
LEISA	Linear Etalon Imaging Spectral Array
MATS	Minimum Actuation Time Sequence
m_r	r^{th} modal mass
n	current motor electrical states
NASA	National Aeronautics and Space Administration
n_{max}	total number of motor electrical states
N_{rev}	steps per SADA output shaft revolution
p_i	i^{th} system pole
PPS	Pulses Per Second
s	Laplace continuous time domain variable
SADA	Solar Array Drive Assembly
SSTI	Small Spacecraft Technology Initiative
T	discrete time sampling period
t	time
T_{detent}	torque developed on the SADA rotor by the motor permanent magnets
TF_{ext}	torque due to external coulomb friction
TF_{ext}	torque due to internal coulomb friction
T_{orbit}	orbital period
$T_{powered}$	torque developed on the SADA rotor by the motor electromagnets
T_{rotor}	total torque developed on the SADA rotor
UCB	Ultraviolet Cosmic Background Spectrometer
VCS	Vibration Controlling Sequence
X	x-direction displacement or rotation
Y	y-direction displacement or rotation
Z	z-direction displacement or rotation
z	discrete time domain variable
z_i	i^{th} system zero

1 Introduction

Structural vibrations must be minimized if continued improvements in the performance of many types of equipment are to be realized. Many different approaches can be utilized in any combination to reduce unacceptable vibrations:

- Additional hardware can be installed to mechanically isolate or dissipate the vibration.
- Sensors and control equipment can be installed to enable a classic feedback control technique to actively respond to and cancel the vibration.
- Operational parameters can be modified to avoid scheduling vibration sensitive tasks while the vibration is present.

All of the above vibration mitigation methods either reduce the possible range of equipment operation or increase the production cost and complexity. When vibrations are induced by actuators within the equipment in the course of performing a desired maneuver, altering or *shaping* the actuator input to avoid initially exciting vibrations would be the simplest solution. The new actuator commands must acceptably perform the desired equipment motion. This *input shaping* technique could potentially solve vibration problems without any additional cost or complexity and allow vibration sensitive tasks to be accomplished at any time. Additional mechanical hardware or feedback control techniques could still be used to augment input shaping.

1.1 Pole-Zero Cancellation Theory

Many different input shaping methods using time domain and frequency domain approaches have been developed. Singer [11] derived an impulse sequence method for vibration control in the continuous time domain, which was later extended to include the suppression of multiple modes of vibration [6, 9]. It has been shown by several researchers [7, 12] that working with input shaping techniques in the Laplace *s*-plane or discrete time *z*-plane rather than in the continuous time domain results in improved mathematical simplicity, especially when a system has multiple undesirable modes of vibration.

Tuttle and Seering [15] have developed a controller design formulation based on the input-shaping technique of Singer, but use pole-zero cancellation in the discrete time domain as suggested by Smith [14]. In this research, the zero-placement technique is used to develop an input shaping algorithm that satisfies structural vibration requirements while operating within actuator capabilities. Controller design incorporating the dynamics of a stepper motor actuator is the primary extension of Tuttle and Seering's work by the current research. Other recent research [2] has examined the use of stepper motor actuators using different vibration control methods.

1.2 Example of Structural Vibration Control: The Lewis Spacecraft

The Lewis spacecraft is a small solar powered Earth-orbiting satellite. Therefore, the satellite must be able to track the sun to maximize the power production from the solar array panels. During normal operation, this tracking is accomplished entirely by rotating the solar arrays relative to the rest of the spacecraft body. This is accomplished by a pair

of stepper motor actuators, one for each of two solar array wings extending from the main body.

Several instruments are onboard the Lewis spacecraft that have strict pointing requirements to satisfy the designed data gathering capability. Any proposed control algorithm for the solar array drive assembly (SADA) actuators must satisfy both of these basic mission requirements as a minimum capability. This problem in structural vibration control is used as an example of the pole-zero cancellation technique.

1.3 Overview of Results

Two different solar tracking methods for the Lewis SADA were initially investigated as baseline cases. The first method was the Constant Step Rate Sequence (CSRS) which tracks the sun most accurately by maintaining a constant step rate that corresponds to one full rotation of the solar array per orbit. This repetitive input results in an average of approximately 19 and 54 μradians of rotational jitter about the *Y*-axis (or *Y*-rotation jitter) for the HSI and LEISA instruments respectively during a 3.5 second period of time, known as a jitter window. These instruments have maximum allowable jitter limits of 10 and 30 μradians respectively, and so the CSRS as simulated was unacceptable. The 3.5 second jitter window allows all identified structural modes (listed in Appendix B) to complete at least one cycle within the window and therefore fully contribute to the measured jitter of the linear simulation. The jitter analysis results using the 3.5 second window only are presented in this section as a summary of the effects of the various SADA control methods investigated.

A second baseline tracking method was the Minimum Actuation Time Sequence (MATS) which makes use of the ±5° maximum "tracking error" allowed and achieves a new solar array orientation in one large rotational slew. From an initial orientation of -5°, the solar arrays would be rotated through the ideal sun orientation of 0° to the opposite maximum of +5° at one time. Approximately 160 seconds later another 10° rotation of the solar arrays would be required. The rotations are done at the maximum angular rate of the actuator to minimize the disturbance time. Structural damping does reduce the vibrational motion during the quiescent period, but the simulated jitter about the Y-axis during a 3.5 second window was an average of approximately 297 μradians for both instruments and never reduced to an acceptable level during the 160 second simulation.

The first Vibration Control Sequence (VCS #1) uses the *z*-plane pole-zero cancellation method of Tuttle and Seering [15] to "shape" the SADA output and cancel the dynamics of eight target structural modes. This sequence achieves acceptable levels of jitter about the *Y*-axis for the HSI instrument for approximately 65% of the 160 second simulation time. The corresponding LEISA jitter results are within the instrument requirements for approximately 84% of the simulation time. The use of VCS #1 to command the SADA actuator would therefore allow the full capability of the HSI and LEISA instruments to be realized for the majority of the time. This would require coordination between the SADA and payload instrument operations, but conservation of angular momentum calculations indicate that even a single step of the SADA actuator would cause unacceptable rigid body motion of the spacecraft bus and therefore this coordination is unavoidable.

VCS #2 introduces the issue of controller robustness by incorporating a 10% error in the target natural frequencies, and is presented as a typical system identification error. This SADA command sequence has *Y*-rotation jitter levels that are about midway between both the VCS #1 and MATS jitter levels and actually has better performance than VCS #1 for jitter about the *X*-axis. However, the VCS #2 jitter about the *Y*-axis is above the jitter limits during the entire simulation for the HSI instrument and approximately 90% of the simulation for the LEISA.

A final vibration controlling sequence, VCS #3, illustrates the proposed method of increasing the input shaping robustness to system identification errors. The same errors in the target frequencies used for VCS #2 are used for this sequence, but now the number of shaper zeros is tripled. Increasing the number of zeros increases the bandwidth of the vibration reduction of the input shaper. The results from this final simulation closely match the performance of VCS #1, and actually allow greater than 67% and 87% of the simulation time to be available for the HSI and LEISA operations respectively. The large improvement in shaper performance in the presence of system identification errors is achieved at no additional actuator or computational requirements.

2 Pole-Zero Cancellation Vibration Control Theory

The residual vibration control design method of Tuttle and Seering [15] is presented. This formulation is based on pole-zero cancellation and the design is accomplished in the discrete time domain. The resulting input shaping function consists of impulse sequences occurring at discrete time intervals. Robustness and multiple mode vibration issues can be handled in a direct geometric manner using *z*-plane shaper design as discussed in Section 2.1. The input shaping impulse sequence is in general convolved with arbitrary actuator commands and the subsequent continuous time input then used to drive the actuator.

2.1 Discrete Time System Description

Denoting the discrete time domain system input as *U(z)*, the shaper transfer function as *H(z)*, and the plant transfer function as *G(z)*, the open loop transfer function description of the system shown in Figure 2.1 is

$$\frac{Y(z)}{U(z)} = G(z) \cdot H(z) \qquad \textbf{(2.1}$$

where *Y(z)* is the system output.

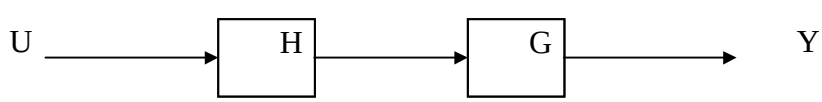

FIGURE 2.1: SYSTEM BLOCK DIAGRAM

The general form of *G(z)* with *k* zeros and *l* poles is

$$G(z) = \frac{(z - z_1)(z - z_1^*)(z - z_2)(z - z_2^*)\ldots(z - z_k)(z - z_k^*)}{(z - p_1)(z - p_1^*)(z - p_2)(z - p_2^*)\ldots(z - p_l)(z - p_l^*)} \quad \textbf{(2.2}$$

where z_i, z_i*, p_i and p_i* are the ith complex conjugate pairs of the plant zeros and poles respectively. The resonant modes are indicated by the poles in *G(z)*. The input to *G(z)* that will not excite particular modes will have matching zeros to cancel the corresponding resonant poles. Following the development of Tuttle and Seering [15], for *m* undesirable modes of vibration in *G(z)*, there are 2*m* complex poles which must be canceled, e.g. p_1 , p_1* , ... , p_m , p_m* . The shaper *H(z)* must take the initial form

$$H(z) = (z - p_1)(z - p_1^*)(z - p_2)(z - p_2^*)\ldots(z - p_m)(z - p_m^*) \quad \textbf{(2.3}$$

The ith damped mode of the system is defined by the complex conjugate pair of poles

$$\begin{Bmatrix} p_i \\ p_i^* \end{Bmatrix} = \begin{Bmatrix} e^{-\zeta_i \omega_{ni} T} e^{j\omega_{di} T} \\ e^{-\zeta_i \omega_{ni} T} e^{-j\omega_{di} T} \end{Bmatrix} \quad \textbf{(2.4}$$

where *T* is the discrete time sampling period, ω_{ni} and ω_{di} are the undamped and damped natural frequencies of the ith mode, and ζ_i is the damping ratio of the ith mode with the standard relationship

$$\omega_{di} = \omega_{ni}\sqrt{1 - \zeta_i^2} \quad \textbf{(2.5}$$

The sampling period *T* is the time intervals at which the discrete time transfer function is defined. It is separate from the sampling period of a digital controller or other hardware in the system and represents the zero-order hold in the transformation of the continuous time physical system into the discrete time representation.

H(z) must be *causal* or *nonanticipatory*, i.e., the output at time *t* does not depend on the input applied after time *t*, but only on the input applied before and at time *t*. Therefore the past affects the future but not conversely and this condition applies to all real systems. The causality condition translates to the *z*-plane as a requirement that the order of the numerator of *H(z)* is less than or equal to the order of the denominator.

The numerator contains all the desired input shaping dynamics. Therefore, placing all the denominator poles at *z*=0 eliminates any denominator dynamics that might unduly affect the input *U(z)*. With these additional requirements, *H(z)* now has the more general form

$$H(z) = C\frac{(z-p_1)(z-p_1^*)(z-p_2)(z-p_2^*)\ldots(z-p_m)(z-p_m^*)}{z^m} \qquad \textbf{(2.6}$$

where C is a constant gain used to change the overall amplitude of the shaper transfer function output.

2.2 Robustness and Multiple-Mode Considerations

Equation 2.6 is a minimally robust version of *U(z)*, i.e. only one shaper zero per system pole. Increasing the number of zeros placed at a particular pole has been shown to improve shaper robustness [12, 15] to variations or inaccuracies in the system parameters defining that mode. The most general form of *H(z)* therefore is

$$H(z) = C\frac{(z-p_1)^{n_1}(z-p_1^*)^{n_1}(z-p_2)^{n_2}(z-p_2^*)^{n_2}\ldots(z-p_m)^{n_m}(z-p_m^*)^{n_m}}{z^{2(n_1+n_2+\ldots+n_m)}} \qquad \textbf{(2.7}$$

where each zero p_i is repeated n_i times, resulting in n_i^{th} order robustness.

In addition, a *z*-plane plot of the shaper zeros and system poles can show in a simple geometric way the relative effectiveness of each shaper zero on multiple system poles. Consider the pole -zero plot of Figure 2.2, which shows the location on the *z*-plane of four poles by their complex conjugate roots.

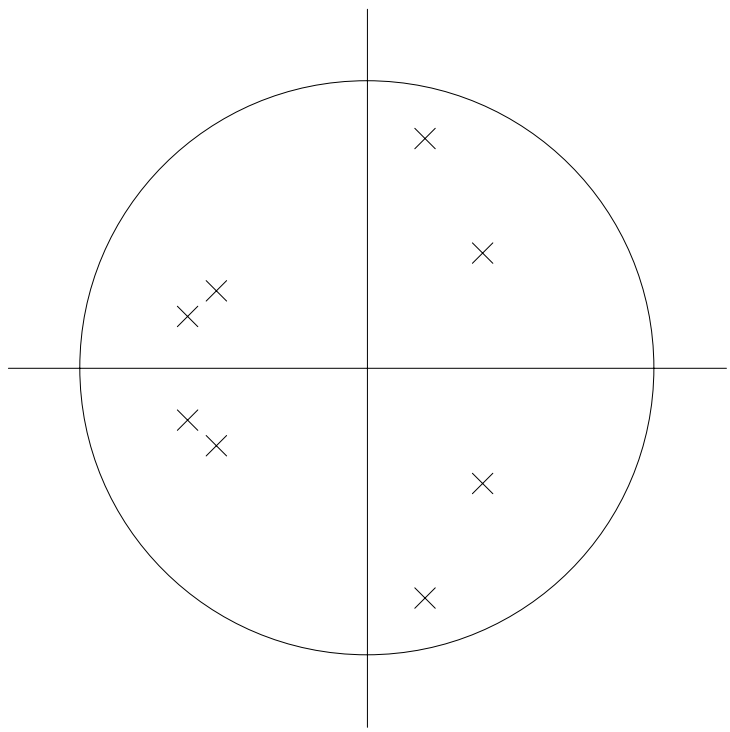

FIGURE 2.2: EXAMPLE SYSTEM POLES IN THE *Z*-PLANE

Undesirable system poles that are near one another in the *z*-plane could be targeted by a lesser number of well-placed shaper zeros [15]. In this manner, an initial shaper transfer function can be very quickly designed and respond to robustness concerns while incorporating a minimum number of shaper zeros. Reducing the number of shaper zeros reduces the time lag produced by convolving the input with the shaper transfer function.

To cancel the four poles in Figure 2.2, four shaper zeros with the same complex roots would be required. Alternatively, three zeros could be employed with one zero being midway between the two closely located poles in the second and third quadrant of the unit circle as shown in Figure 2.3. The plant dynamics represented by those two poles would not be completely canceled but may be reduced to acceptable levels while the additional dynamics and time delay introduced by the shaper are decreased.

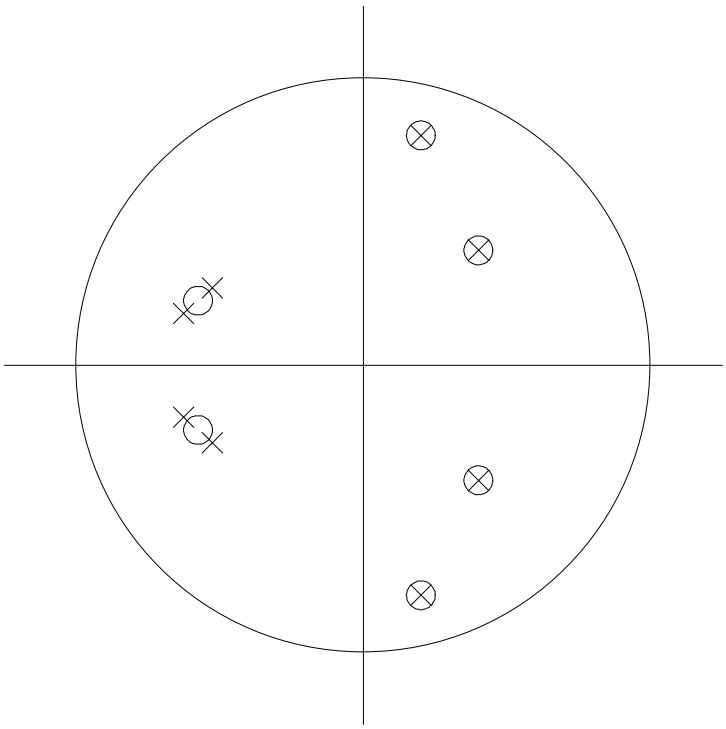

FIGURE 2.3: EXAMPLE SYSTEM POLES AND SHAPER ZEROS IN THE *Z*-PLANE

2.3 Time Domain Implementation

Expanding the terms of Equation 2.7 yields

$$H(z) = C\frac{z^{2(n_1+n_2+\ldots+n_m)} + a_1 z^{2(n_1+n_2+\ldots+n_m)-1} \ldots a_{2(n_1+n_2+\ldots+n_m)-1} z + a_{2(n_1+n_2+\ldots+n_m)}}{z^{2(n_1+n_2+\ldots+n_m)}} \quad \textbf{(2.8}$$

and mapping the *z*-plane poles and zeros to the *s*-plane by the relation

$$z = e^{sT} \quad \textbf{(2.9}$$

yields the equivalent continuous time transfer function

$$H(s) = C\frac{e^{2(n_1+n_2+\ldots+n_m)sT} + a_1 e^{(2(n_1+n_2+\ldots+n_m)-1)sT} \ldots a_{2(n_1+n_2+\ldots+n_m)-1} e^{sT} + a_{2(n_1+n_2+\ldots+n_m)}}{e^{2(n_1+n_2+\ldots+n_m)sT}} \quad \textbf{(2.10}$$

Transforming Equation 2.10 to the time domain can be accomplished by dividing the numerator by the denominator and taking the inverse Laplace transform, which results in

$$H(t) = C\left[\delta(t) + a_1\delta(t-T) + a_2\delta(t-2T) + \ldots + a_{2(n_1+n_2+\ldots+n_m)}\delta(t-2(n_1+n_2+\ldots+n_m)T)\right] \quad \textbf{(2.11}$$

Equation 2.11 represents a series of impulses of varying magnitudes that are evenly spaced in time by *T*, the discrete time sampling period. The constant *C* can be used to scale the amplitudes *a* such that the sum of all the impulse amplitudes is unity or any arbitrary value.

As *T* is varied for any given set of shaper zeros, the dimensionless impulse amplitudes will change according to the relations above. In this manner, an infinite set of impulse amplitudes and corresponding time spacing between them can be found with the same theoretical vibration canceling effect. In practice, the minimum time spacing and maximum impulse magnitude are limited by the actuator capability. The maximum time spacing is generally limited by the desired system performance since increasing *T* causes an increased

time delay when convolving the input shaping impulse sequence with an arbitrary input [15].

2.4 Extension of Pole-Zero Cancellation for Stepper Motors

The input shaping transfer function as developed by Singer, et al [9, 10] is intended for convolution with an arbitrary input. For simplicity, assume the arbitrary input is a constant torque. The convolution of the impulse sequences with a constant torque results in a series of impulsive torques that are related to the constant torque value by the impulse amplitudes a. Figure 2.4 shows a representative set of impulse amplitudes with T=3 seconds.

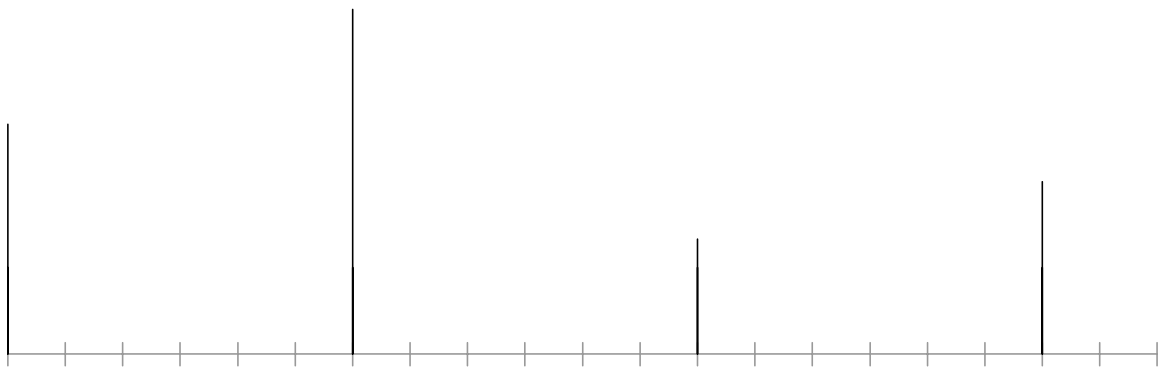

FIGURE 2.4: EXAMPLE IMPULSE AMPLITUDES

A stepper motor actuator cannot produce a specified torque, it can only increment the output shaft forward or reverse at a specified step rate. Since a true impulse is impossible to produce, it is proposed that a variable number of actuator steps at a high step rate could have a similar effect on the structure as a variable magnitude “impulse” torque. Each impulse torque is transformed into a sequence of actuator steps and assuming a maximum

step rate is used for all sequences, larger impulse amplitudes result in longer step sequences, as shown in Figure 2.5.

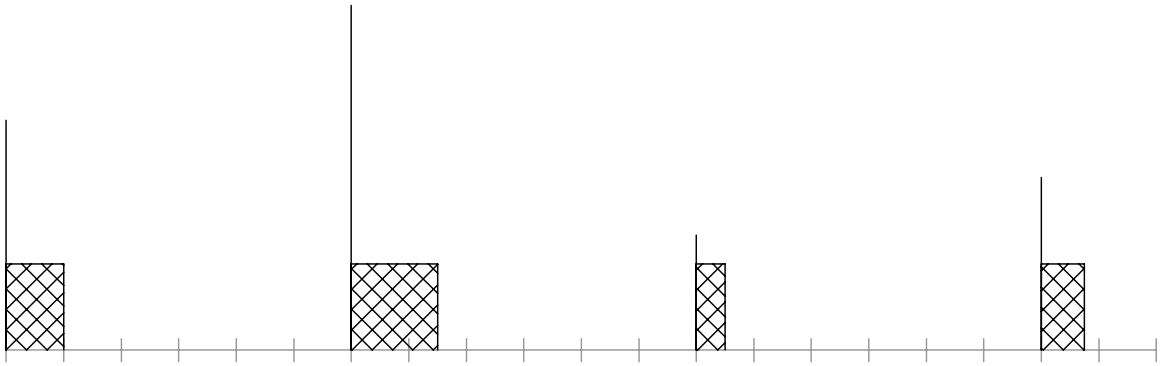

FIGURE 2.5: EXAMPLE IMPULSE AMPLITUDES AND STEP SEQUENCE APPROXIMATIONS

Finally, the step sequences are shifted in time so that each sequence is centered about the original impulse time as shown in Figure 2.6.

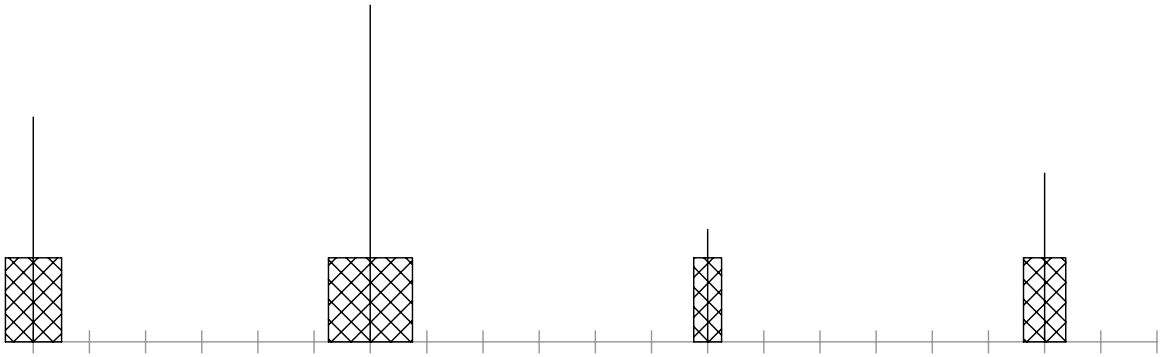

FIGURE 2.6: EXAMPLE TIME –ADJUSTED STEP SEQUENCE APPROXIMATIONS

2.5 Selection and Implementation of Vibration Control Sequences

There are an infinite number of input shaping transfer functions that can be developed. However, actuator and application-specific constraints will most likely not allow most of these possible transfer functions and favor some of the remaining over others. To aid in

the selection of transfer functions, several guidelines in the form of error calculations are presented.

2.5.1 Error Calculations

The step sequences produced by the procedure of Section 2.4 do not in general consist of integer numbers of steps and must be rounded to integer values for implementation by a stepper motor. The total error produced by rounding the amplitudes is defined as

$$E_{rounding}^{sum} = \sum_{i=1}^{2N+1} E_{rounding}^{i} = \sum_{i=1}^{2N+1} \left| a_i - round\left(a_i\right) \right| \qquad \textbf{(2.12}$$

and was one criteria used in the ranking of the many possible input shaper solutions. The maximum rounding error

$$E_{rounding}^{max} = \max\left(E_{rounding}^{i}\right) \qquad \textbf{(2.13}$$

within each solution was also calculated. Ranking the solutions in order of increasing error was developed as an aid in selecting a solution for a simulation run. Concern about the disparity between the mathematically ideal impulse amplitude and the resulting rounded number of stepper motor steps assumes the structure is sensitive to the exact number of steps.

Conversely, if the structure is insensitive to the exact number of steps, then the step sequences will all have a similar effect on the structure. It would therefore be desirable that the vibration control solution require the same force or torque on the structure at each sampling time *T*. This translates to having all the impulse amplitudes as close in value as possible. The variation between the normalized impulse amplitudes and an ideal amplitude

(which is constant for all 2*N*+1 impulses) was a second criteria used to rank the solutions and is defined as

$$E_{variation}^{sum} = \sum_{i=1}^{2N+1} E_{variation}^{i} = \sum_{i=1}^{2N+1} \left| a_i - \frac{1}{2N+1} \right| \qquad \textbf{(2.14}$$

The maximum variation error

$$E_{variation}^{max} = \max\left(E_{variation}^{i}\right) \qquad \textbf{(2.15}$$

can also be calculated for each solution.

2.5.2 Other Considerations

The values for *T* must be compatible with the actuator and problem specifications to generate useful sets of impulse sequences. The actuator is capable of a maximum stepping rate and therefore a minimum time between steps can be calculated. Therefore, *T* should be incremented by this minimum interval throughout a specified range. The range for *T* was chosen based on the number of zeros (and therefore the number of step sequences) that were to be implemented by the input shaper transfer function.

In general, smaller values of *T* and larger values for *N* were desirable for several reasons. Placing *N* zeros in the shaper transfer function results in 2*N*+1 impulses in the time domain. As the number of impulses in the solution increases, the number of steps contained within each step sequence generally decreases, and therefore less time is required for that sequence. Smaller step sequences should have more of an impulsive nature in their effect on the structure and can be placed closer together, i.e., the sampling period *T* can be smaller. As *T* decreases, all 2*N*+1 step sequences can be completed in less

time and there is more time in the simulation for structural damping to quiet residual vibrations that could have a significant effect.

3 Example Of Structural Vibration Control

3.1 Overview Of Lewis Spacecraft

The National Aeronautics and Space Agency (NASA) Small Spacecraft Technology Initiative (SSTI) is intended to demonstrate the viability of new technologies for use in space. The first pair of these next generation satellites are appropriately named Lewis and Clark. These satellites feature modular construction and make extensive use of off-the-shelf hardware. The current SSTI program has formed partnerships between NASA and two aerospace corporations: TRW is the corporate partner for the Lewis (shown in Figure 3.1) and CTA is the partner for the Clark spacecraft.

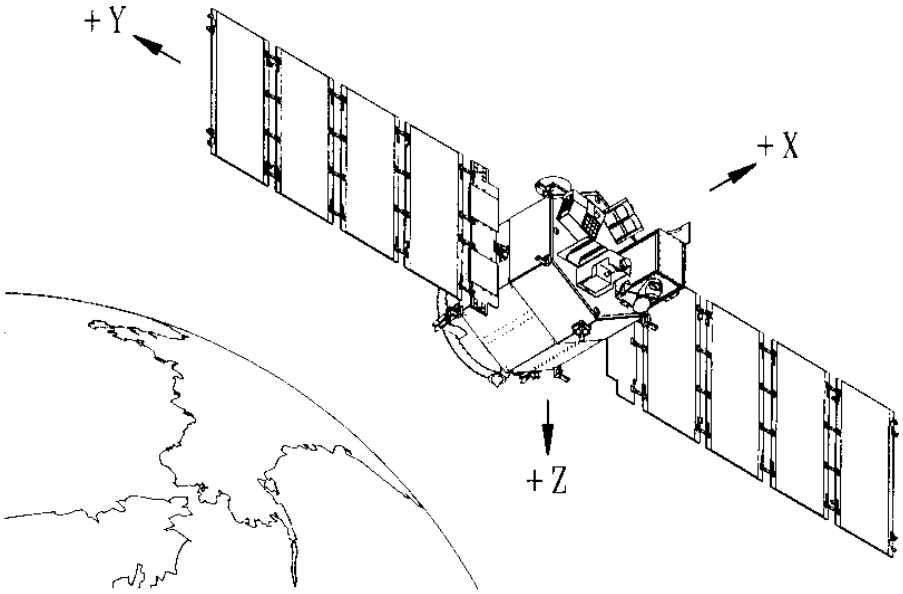

FIGURE 3.1: LEWIS SPACECRAFT

3.1.1 Lewis Orbital Operations

The Lewis spacecraft [13] will be inserted into a sun-synchronous orbit with a mean altitude of 283 nautical miles and 97.1° inclination. The orbital period will be approximately 95 minutes and for approximately 63% of the orbit, Lewis will be in sunlight. Some of the major operations over the course of a single orbit are illustrated in Figure 3.2.

While the satellite is in sunlight, there are two primary instruments which will observe Earth: the Hyper Spectral Imager (HSI) and Linear Etalon Imaging Spectral Array (LEISA). During the orbital eclipse, the Ultraviolet Cosmic Background Spectrometer (UCB) will operate to avoid interference from the sun.

The two solar array wings are required to track the sun and maximize power generation during the sunlit period. The Solar Array Drive Assembly (SADA) of the

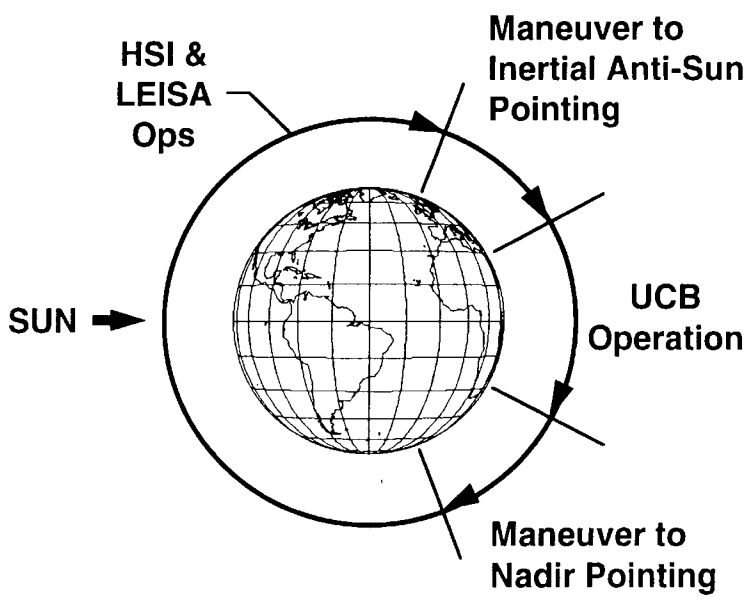

FIGURE 3.2: LEWIS SPACECRAFT ORBITAL OPERATIONS

Lewis spacecraft can rotate the solar array wings 360° continuously about the *Y*-axis and is required to track the sun to within ±5°. For a given orientation of the other two spacecraft axes with respect to the sun, this specification will assure at least 99.6% of the maximum solar radiation is available for electrical power generation. The SADA utilizes a rotary stepper motor which is capable of up to 200 steps or pulses per second (PPS). The stepper motor actuator imparts impulsive-like torques into the Lewis structure.

The HSI and LEISA instruments have relatively high resolution capabilities and consequently are sensitive to small amplitude vibrations. The requirements for the UCB instrument are not critical and it is not necessary for the solar arrays to track the sun during the 35 minute eclipse. Consequently, this research is limited to the operations and requirements during the approximately 60 minutes per orbit when the SADA could potentially incur structural vibrations that reduce the HSI or LEISA data quality. The range of time these two instruments may require to complete gathering data for an image and the maximum allowable vibratory motion or *jitter* of the instrument boresight is given in Table 3.1.

TABLE 3.1: PAYLOAD INSTRUMENT MISSION REQUIREMENTS

	HSI	*LEISA*
Minimum Data Acquisition Period	3 sec	20 sec
Maximum Data Acquisition Period	30 sec	50 sec
Maximum Allowable Boresight Jitter	10 μradians, < 250Hz 2 μradians, > 1500Hz	30 μ radians

3.1.2 Physical Description

Table 3.2 summarizes the dimensions, masses, idealized geometry, and the corresponding moments of inertia of the spacecraft bus and the solar array wings.

TABLE 3.2: LEWIS SPACECRAFT PHYSICAL QUANTITIES

	Basic Shape & Dimensions (in)	*Weight* (lbf)	I_{xx} (lbf-in-s^2)	I_{yy} (lbf-in-s^2)	I_{zz} (lbf-in-s^2)
Spacecraft Bus	Cylinder: 70 x 28 (radius)	797.2	25.16	38.78	38.78
Solar Array	Flat Plate: 59 x 138 x 1	26.4	3.989	0.6167	3.373

3.1.3 Description Of Payload Instruments Module And Mission Requirements

The payload instruments are attached to the upper payload platform as shown in Figures 3.4. These items consist of the Hyper Spectral Imager (HSI), Linear Etalon Imaging Spectral Array (LEISA), Ultraviolet Cosmic Background Spectrograph (UCB), and both the Wide and Narrow Field of View Star Tracker Assemblies. For each instrument, there are six possible jitter quantities: a displacement and a rotation corresponding to each of the three orthogonal Cartesian coordinates. Displacements have a negligible effect on the pointing accuracy of instruments in orbit due to the large distances between the instrument and subject. Therefore, only the three rotations are of possible concern.

The HSI has a line-of-sight that is fixed relative to the spacecraft and parallel to the *Z* axis. The line-of-sight of the LEISA can change within the instrument field-of-regard, but the field-of-regard is centered about a vector that is parallel to the HSI line-of-sight. Rotation about the line-of-sight is a secondary concern and so the two important motions

for the rotational jitter are along the spacecraft *X*- and *Y*-axes. The maximum allowable jitter for these instruments is listed in Table 3.1.

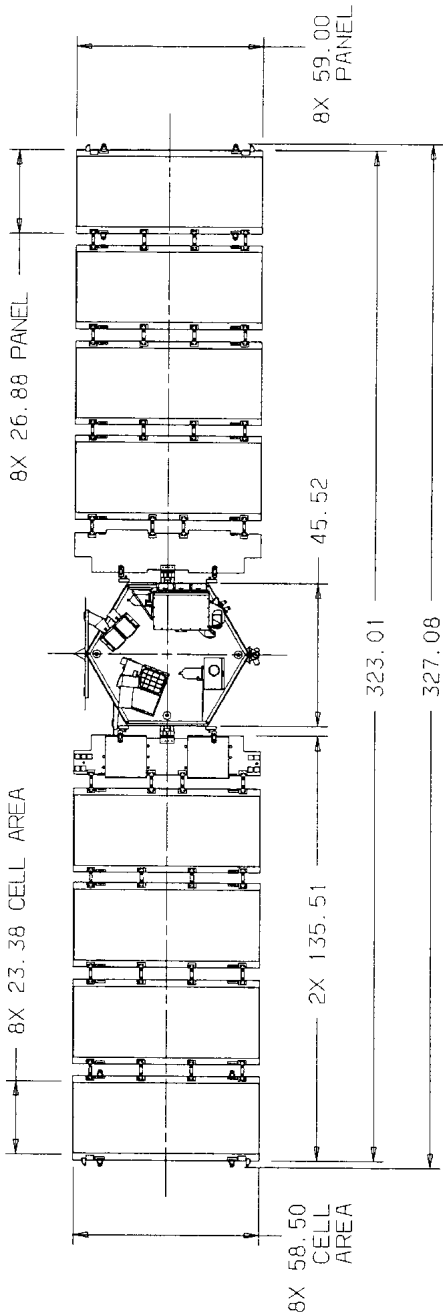

FIGURE 3.3: SPACECRAFT DIMENSIONS (INCHES)

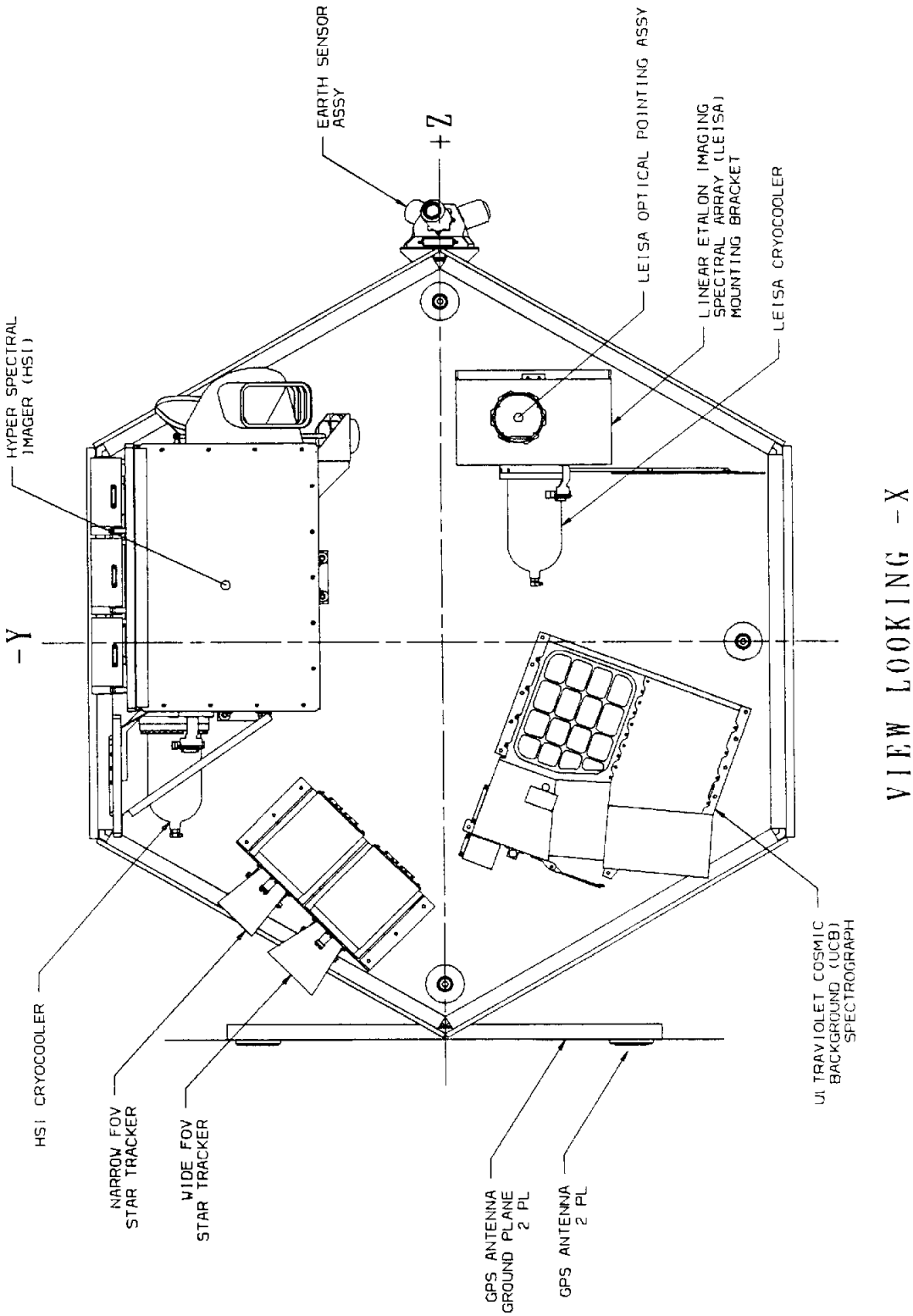

FIGURE 3.4: PAYLOAD INSTRUMENT MODULE PLAN VIEW

3.1.4 Description Of Solar Array Drive Assembly And Mission Requirements

Each of the two Solar Array Drive Assemblies (SADA) for Lewis use a single Schaeffer Magnetics Type 2 Rotary Incremental Actuator and associated drive electronics. The SADA's have the functional requirement of pointing the solar arrays at the sun within ±5° about the *Y* axis. Each solar array wing interfaces with the main spacecraft bus via 52 sliprings and the actuator output shaft. This arrangement provides continuous 360° rotational freedom of motion. The actuator output shaft is aligned with the spacecraft *Y*-axis. A more detailed view of the solar array wings is shown in Figure 3.5. The specifications for the Schaeffer Magnetics stepper motor are shown in Table 3.3.

TABLE 3.3: TYPE 2 STEPPER MOTOR SPECIFICATIONS

Output shaft step angle, $\Delta\theta_{SA}$	0.02°
Steps per revolution, N_{rev}	18,000
Harmonic drive ratio, GR	100
Rotor step angle, $\Delta\theta_r$	2.0°
Output step rate, ω_{max}^{motor}	450 steps/sec; 9.0°/sec
Holding torques	Powered: 150 in-lbf Detent: 50 in-lbf
Torsional stiffness	6,000 in-lbf/rad
Total assembly weight	2.0 lbf
Rotor moment of inertia, I_r	8.3×10^{-5} lbf-in-s^2

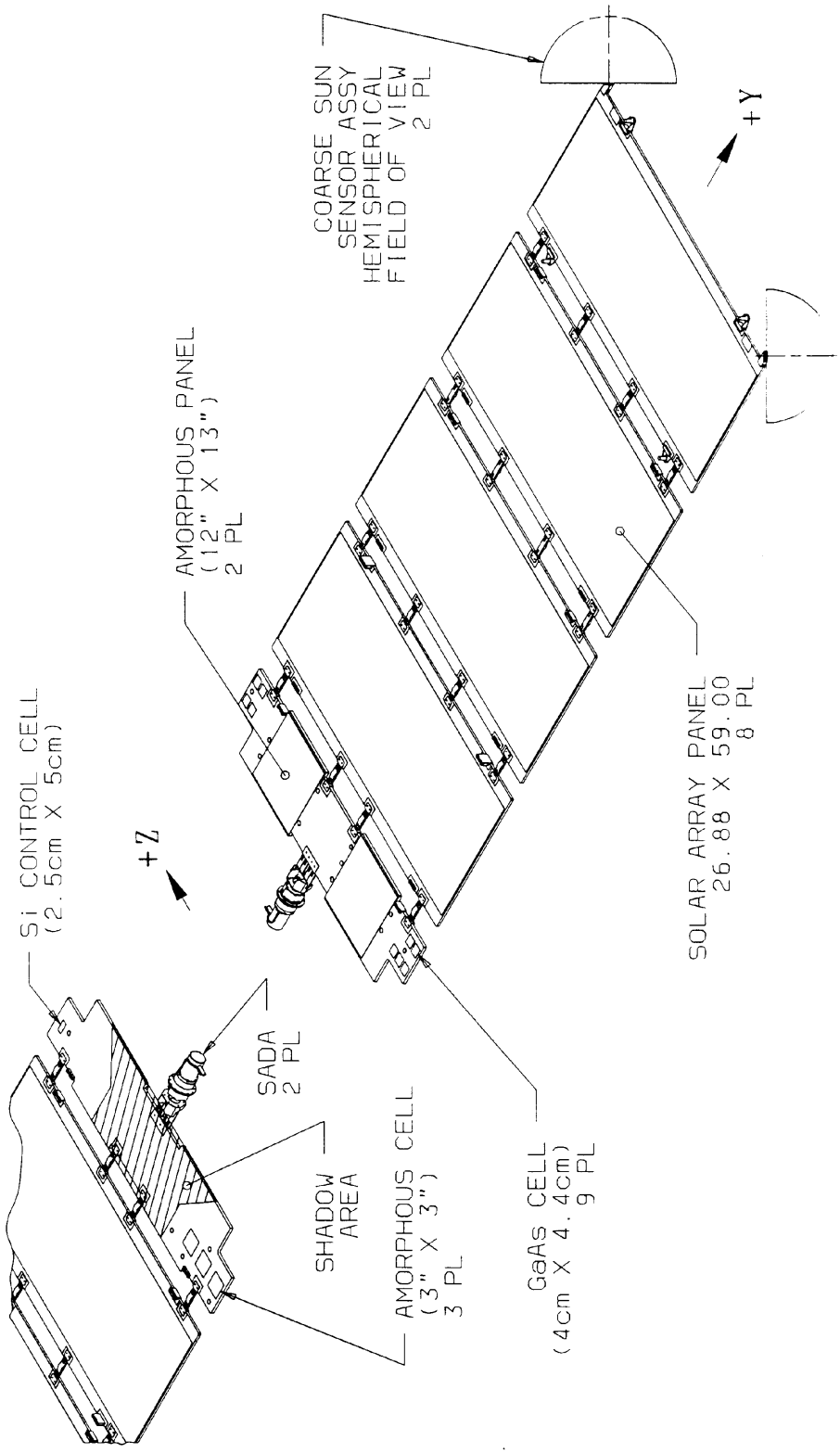

FIGURE 3.5: SOLAR ARRAY WING ISOMETRIC VIEW

Figures 3.6 and 3.7 illustrate the basic physical dimensions and the main internal components of the Type 2 actuator. During SADA operation, the stator electromagnets develop torque on the rotor. The rotor then transfers this torque and resulting angular motion through the harmonic drive, a gear reduction device. The harmonic drive transfers the amplified SADA torque to the motor output flange and end load. The end loads for the Lewis spacecraft SADA's are the solar array panels.

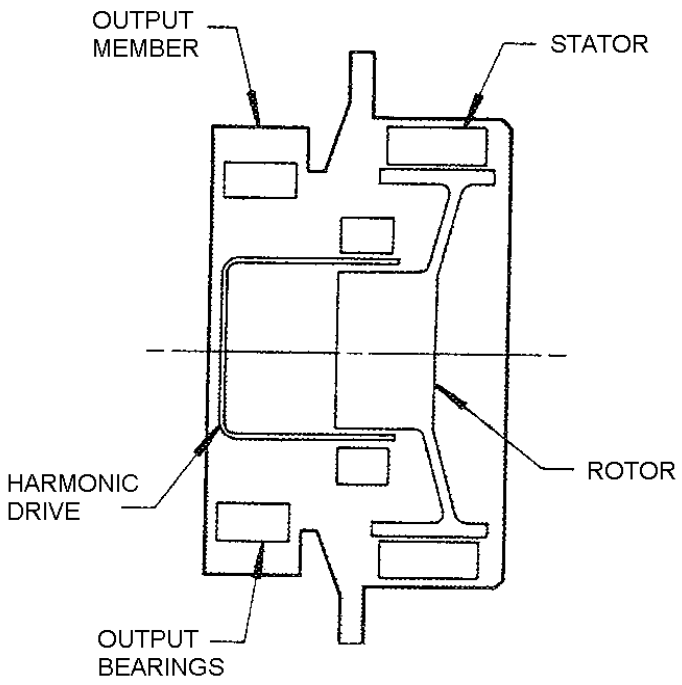

FIGURE 3.6: TYPE 2 STEPPER MOTOR CUT-AWAY VIEW

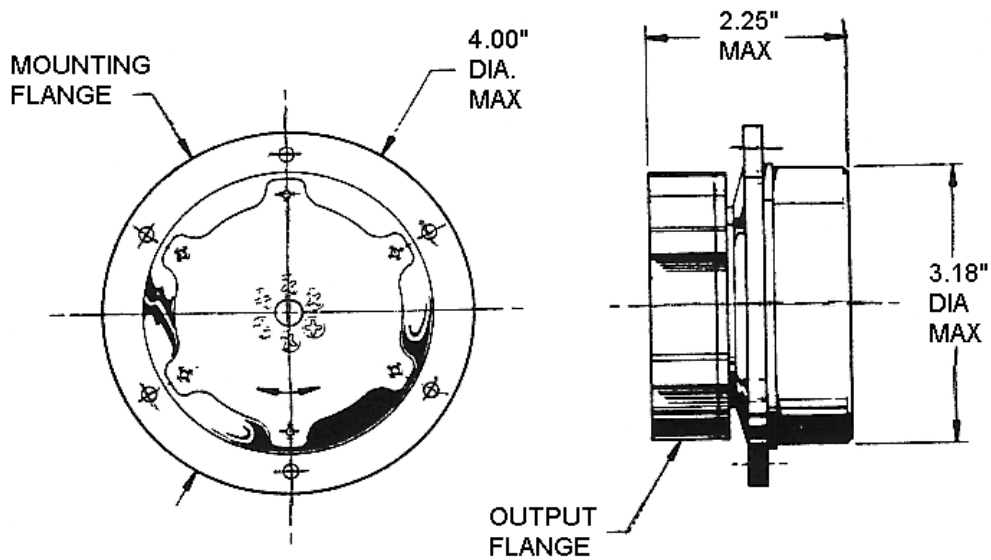

FIGURE 3.7: TYPE 2 STEPPER MOTOR EXTERNAL VIEW

The Lewis SADA uses a rotational stepper motor as an actuator and any desired solar array orientation corrections must be discretized for implementation by the stepper motor. During sunlit periods, the power optimal SADA operation would be to continuously move the solar array at a constant velocity of

$$\omega_{tracking}^{SA} = \frac{360°}{T_{orbit}} \approx 0.0632°/\text{sec} \qquad \textbf{(3.1}$$

where T_{orbit} is the orbital period, approximately 5700 seconds. Discretizing this quantity according to the stepper motor specifications results in the tracking step rate of

$$\omega_{tracking}^{motor} = \frac{\omega_{tracking}^{SA}}{\Delta\theta_{step}^{SA}} \approx 3.16 \frac{\text{step}}{\text{sec}} \qquad \textbf{(3.2}$$

This quantity is about 0.7% of ω_{max}^{motor}, the maximum step rate of the actuator listed in Table 3.3. Experimental investigations by Miller [LaRC, private communication] have shown step rates up to 100 Hz to be dynamically discrete operations for unloaded Schaeffer Magnetics Type 1 actuators in the laboratory. However, the Type 2 actuator employed on Lewis is a larger stepper motor and will have a significantly different environment and an end load. The motor dynamics are further discussed in Section 3.2.

All simulations for this research were conducted for 10° of SADA rotation over a total time of 160 seconds. These parameters were chosen based on two requirements. First, the normal to the solar array panels is allowed to vary up to 5° about the *Y* axes from the sun vector, resulting in at most a 0.4% decrease from the maximum possible incident solar radiation. This allows a maximum rotational motion at one time of 10°, if the solar arrays begin with a 5° bias. Second, this amount of rotation for the solar arrays is required over an interval of time dictated by the orbital period and is

$$\frac{10°}{\omega_{tracking}^{SA}} \approx 158.3 \text{seconds} \qquad \textbf{(3.3}$$

which was then rounded up to 160 seconds.

3.1.5 Angular Momentum Calculations

A single finite element model (FEM) was used to simulate the spacecraft structure. This model had a fixed orientation of the solar arrays relative to the spacecraft bus and did not allow the rotation of the solar array panels to be simulated. Therefore, the simulated

SADA torque acts as an external torque on the FEM at the nodes corresponding to the SADA's and is not represented by equal and opposite internal torques. The angular momentum of the system is *not* conserved since the SADA output acts as an external torque. To provide a basic check on the simulation results the following calculations are performed.

By rotating both solar arrays at the solar tracking velocity, the simulated SADA torque should increase the angular momentum of the system by the quantity

$$2 I_{yy}^{SA} \omega_{tracking}^{SA} = 1.36 \times 10^{-3} \text{ lbf} \cdot \text{in} \cdot \text{sec} \qquad \textbf{(3.4}$$

Dividing this angular momentum increase by the combined inertia of the spacecraft bus and the solar arrays yields the average angular velocity of the spacecraft expected from the CSRS simulation as

$$\omega_{tracking}^{s/c} = 3.4 \times 10^{-5} \frac{\text{radians}}{\text{sec}} \qquad \textbf{(3.5}$$

A simulated 10° rotation of the solar array panels will maintain this average velocity for 158.3 seconds and cause a total spacecraft rotation of

$$\Delta\theta_{simulation}^{s/c} = 5.4 \times 10^{-3} \text{ radians} \qquad \textbf{(3.6}$$

This quantity is then used as a basic check on the various stepper motor command sequences. Since each sequence should simulate a 10° solar array rotation, the total spacecraft rotation should approximately equal $\Delta\theta_{simulation}^{s/c}$.

3.2 Lewis Spacecraft Dynamic Model

Several different analytical tools were used to complete this research. A model of the Lewis spacecraft structural dynamics was a core element, and it was fundamental to producing the final results simulating the jitter experienced by the payload instruments. A separate dynamic model of the Schaeffer Magnetics Type 2 actuator employed within the Solar Array Drive Assembly (SADA) was used to develop the torque time profiles of the SADA operations. These two components were then incorporated into one computer based simulation through the use of the PLATSIM [4] analysis package.

3.2.1 Structural Model

A NASTRAN finite element model was used to develop a modal model of the spacecraft structural dynamics. The finite element model (FEM) eigensolution identified the flexible body modes and the corresponding lowest 163 natural frequencies are listed in Appendix B. The modal damping ratio was modeled as 0.2% for all modes. The mass-normalized modeshapes at the nodes corresponding to the HSI and LEISA instruments and the two SADA's were available to the author. The modeshape information was not included for space considerations.

3.2.2 PLATSIM Linear Analysis Software

PLATSIM [4] is a NASA Langley Research Center developed software package that incorporates the spacecraft modal model, ACS description, and the disturbance models into one dynamic simulation. Various disturbance scenarios can be constructed and used as input to the modal model. During a time domain simulation, these scenarios are input to the modal model at the specific node(s) associated with the disturbance source. The

response of specific nodes can be selected and their response tracked during the simulation. Displacement, rate, or acceleration data can be chosen as the output for each node and jitter analysis can be conducted.

3.2.3 Stepper Motor Model

Farley modified a dynamic model of a Schaeffer Magnetics Type 1 actuator [3] to represent a Type 2 actuator for the author [private communication]. Additional data for the Lewis spacecraft application was determined [13] and used to create various torque time profiles of the motor output flange.

The four degree of freedom (DOF) electromechanical dynamic model developed by Farley is shown in Figure 3.8. The inertia, damping, and stiffness characteristics of the spacecraft, motor rotor, harmonic drive gear reduction, end load and their connecting elements are included. The coulomb friction acting on the harmonic drive gear reduction inside the stepper motor (*TFint*) and acting on the output flange (*TFext*) are also included. The data used in the motor simulation to describe the model is listed in Tables 3.4 and 3.5

The static, back EMF, and transient currents in the stepper motor electrical system can be calculated from the motor model. These currents superpose within the electromagnets to develop torque on the rotor. The model requires the permanent magnet or detent torque maximum amplitude, motor electrical constant, resistance of each phase separately, series resistance of all 3 phases, inductance of each phase, and applied voltage. The motor was treated as having a constant voltage source and the limiting current (the largest current that can be drawn by the motor) was therefore defined.

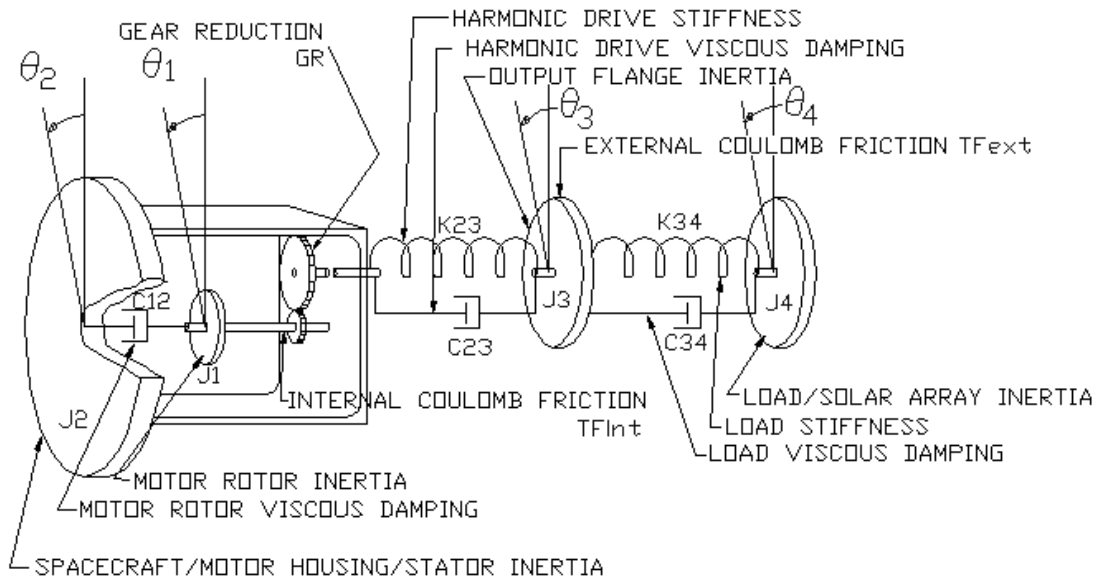

FIGURE 3.8: FOUR-DOF STEPPER MOTOR MODEL DIAGRAM

TABLE 3.4: STEPPER MOTOR MODEL MECHANICAL SPECIFICATIONS

Motor Rotor Inertia, *J1*	9.38×10^{-6} Kg-m^2
Spacecraft Inertia, *J2*	4.38 Kg-m^2
Output Flange Inertia, *J3*	0.03 Kg-m^2
Load / Solar Array Inertia, *J4*	0.0697 Kg-m^2
Harmonic Drive Torsional Stiffness, *K23*	677.9 N-M/rad
Load Torsional Stiffness, *K34*	50 N-M/rad
Rotor Viscous Damping, *C12*	0.0 N-m/rad-sec
Harmonic Drive Damping Ratio, *C23*	0.1
Flexible Load Damping Ratio, *C34*	0.02
External Coulomb Friction, *TFext*	0.268 N-m
Internal Coulomb Friction, *TFint*	0.117 N-m (Rotor Break-away Friction)
	0.003 radians (Dahl Friction Factor)
Gear Reduction Ratio, *GR*	100:1
Output Step Size	2 degrees

TABLE 3.5: STEPPER MOTOR MODEL ELECTRICAL SPECIFICATIONS

Applied Voltage	12 volts
Current Limit	0.5 amps
Phase Inductance	0.003 Henrys
Series Resistance (all phases)	0.35 Ohms
Phase Resistance	12 Ohms
Motor Constant	0.169477 N-m/Amp
Detent Torque	0.056492 N-m
Maximum Pulse Width	0.035 seconds
Minimum Dead Time Between Pulses	0.0005 seconds

Different types of stepping sequences can be simulated within the model: a constant step rate, or a linear ramping or staircase ramping of the step rate. Only a constant 200 steps or *pulses* per second (PPS) step rate was used for this research, but it is common practice to ramp up the motor step rate in various ways to more smoothly accelerate the load. These other methods would be of possible interest in further studies of vibration control using stepper motors. For all step rate options, the motor model requires information about the maximum pulse width and minimum dead time or spacing between pulses, as illustrated in Figure 3.9 and listed in Table 3.5.

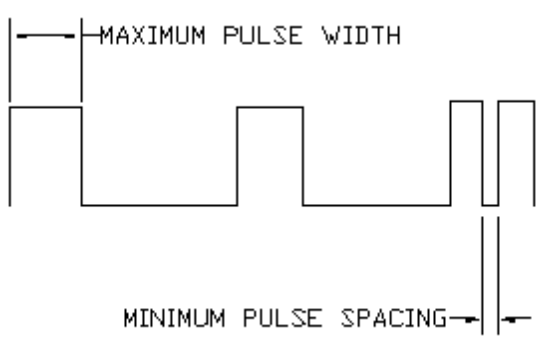

FIGURE 3.9: MOTOR STEPPING OPERATION PARAMETERS

3.3 Determination of Target Modes

The NASTRAN analysis of the finite element model of Lewis returned a mass-normalized eigenvalue solution and the 163 lowest frequency flexible-body modes were then identified. A frequency response function analysis was used to determine the modes that had the strongest coupling between the two SADA input nodes and the two payload instrument output nodes.

3.3.1 Finite Element Analysis Results

Modeshapes are ratios of motions between all of the nodes within a finite element model and only the relative magnitude of a particular value is important. Most of the low frequency modes involve relatively large motions of the solar arrays compared to the deflection of the rest of the structure, and this is not surprising due to their large size and flexibility. The modeshape values, however, do not directly indicate the quantitative relationship between SADA input and the resulting payload instrument motion.

The natural frequencies identified range from 0.3 Hz to 149.5 Hz with 13 modes having a resonant frequency below 10 Hz. The damping ratio for all modes was modeled as 0.2% and lower frequency modes would dissipate energy more slowly than high frequency modes. Therefore, the low frequency modes would affect the jitter at the payload instruments more than higher frequency modes during a quiescent period without SADA input.

The stepper motor input is simulated at 200 PPS and would be expected to excite high frequency modes. High frequency modes would therefore possibly affect the jitter at the payload instruments more than lower frequency modes during active periods with

SADA input. Selecting the target modes for pole-zero cancellation will require a more objective FRF analysis.

3.3.2 Frequency Response Function

The frequency response function (FRF) quantitatively defines the relationship between a pair of input and output locations within a structure over a range of frequencies. The coordinate direction of each location must be defined as well. For example, an input could be at one of the SADA nodes with a torque in the *Y* direction, and an output could be the rotation about the *X*-axis of the HSI node.

For a modal, two degree of freedom system, the FRF reduces to

$$H_{ij}(\omega) = \sum_{r=1}^{N} \frac{\phi_{ir}\phi_{jr} / m_r}{\left(\omega_{nr}^2 - \omega^2\right) + j2\zeta_r\omega_{nr}\omega} \qquad \textbf{(3.7}$$

where there are N modes to be included. The rth mode has a natural frequency ω_{nr}, damping ratio ζ_r, modal mass m_r, and corresponding modeshape coefficients ϕ_{ir} and ϕ_{jr} (for input node i and output node j). $H_{ij}(\omega)$ is a complex number and typically is shown on a magnitude and phase plot. To evaluate the importance of each mode to the input-output relationship, only the magnitude information is of concern.

Normally, the response for all the N modes is summed as shown in Equation 3.7. The modes can be ranked in contribution to the magnitude of the input-output relationship by calculating the frequency response function for each mode at its natural frequency. This results in the purely imaginary quantity

$$H_{ij}(\omega_n) = \frac{\phi_{ir}\phi_{jr} / m_r}{j2\zeta_r\omega_{nr}^2} \quad \textbf{(3.8}$$

Each mode therefore contributes a specific magnitude response at the output location to a unit input. These 163 different values are then sorted and used to identify the most important modes in causing the output response. Both Equations 3.7 and 3.8 were used for a total of eight different input output pairs: both SADA's as inputs and the HSI *X*-rotation, LEISA *X*-rotation, HSI *Y*-rotation, and LEISA *Y*-rotation as outputs.

3.3.3 Modal Input-Output Analysis

The two different SADA nodes were denoted as SADA #1 and SADA #2 for clarity. All simulations operated both solar array drives in tandem, using the same vibration control solution to determine the step sequences. Therefore the SADA's are handled separately only during the FRF analysis. The FRF analysis was performed for all eight input-output pairs: two SADA's with torque about the *Y*-axis as inputs and the HSI and LEISA rotations about the *X*- and *Y*-axes as outputs.

Figure 3.10 shows the FRF for the input-output pair SADA #1 (*Y*-rotation) - HSI (*X*-rotation). The lower frequencies have the largest magnitude response, but there is a broad band of increased coupling from about 65 to 130 Hz. Specifically, the two highest peaks occur under 5 Hz and there are other sizable responses at about 65 Hz, 85 Hz, and 115 Hz.

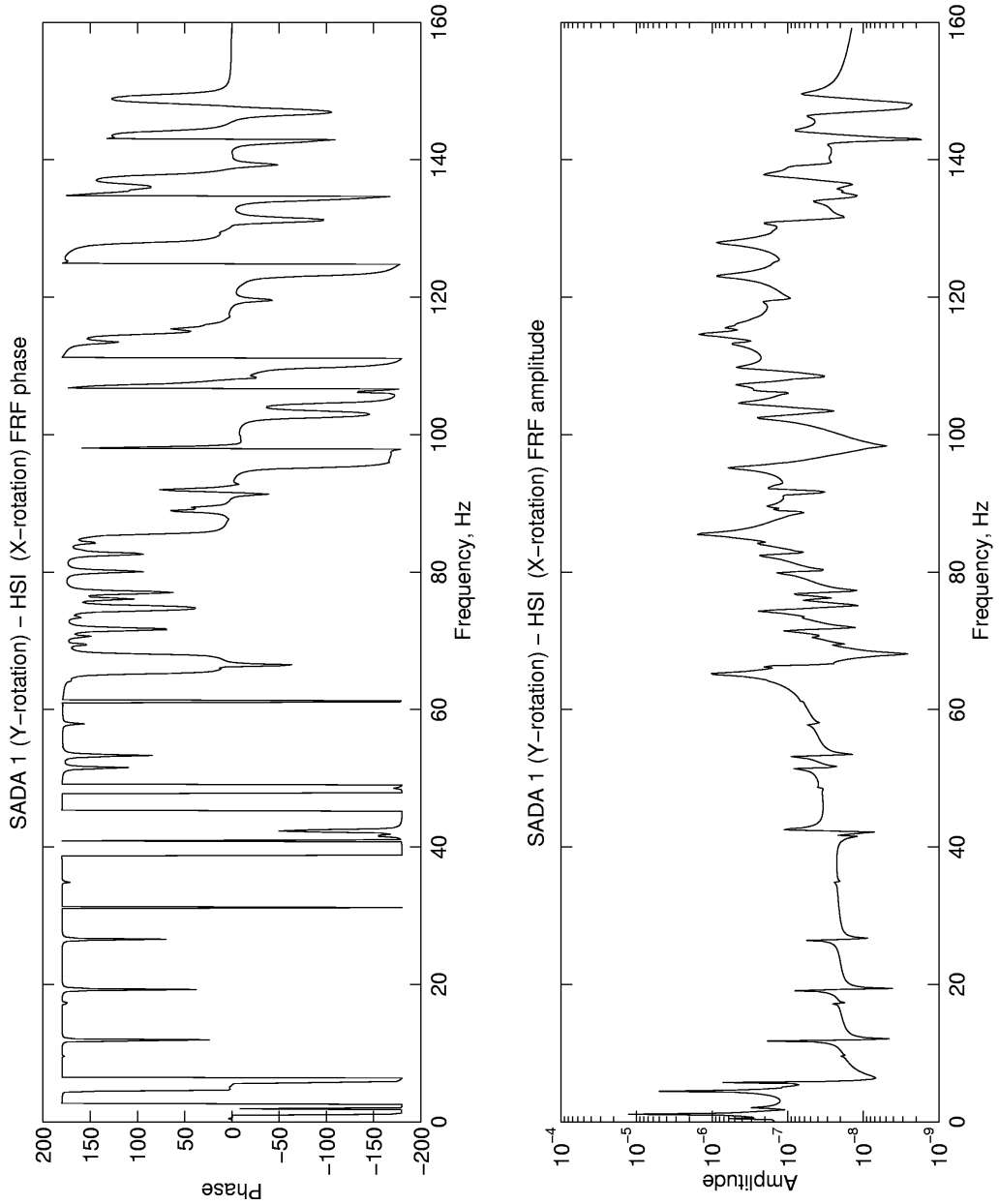

FIGURE 3.10: SADA #1 *Y*-ROTATION (INPUT) – HSI *X*-ROTATION (OUTPUT) FRF

Use of Equation 3.8 ranked each mode in its importance with respect to this input-output pair. A semilog plot of the ranked modes is shown in Figure 3.11. The two highest decades of the plot contain 10 modes, with the other 153 modes decreasing to eight orders of magnitude less.

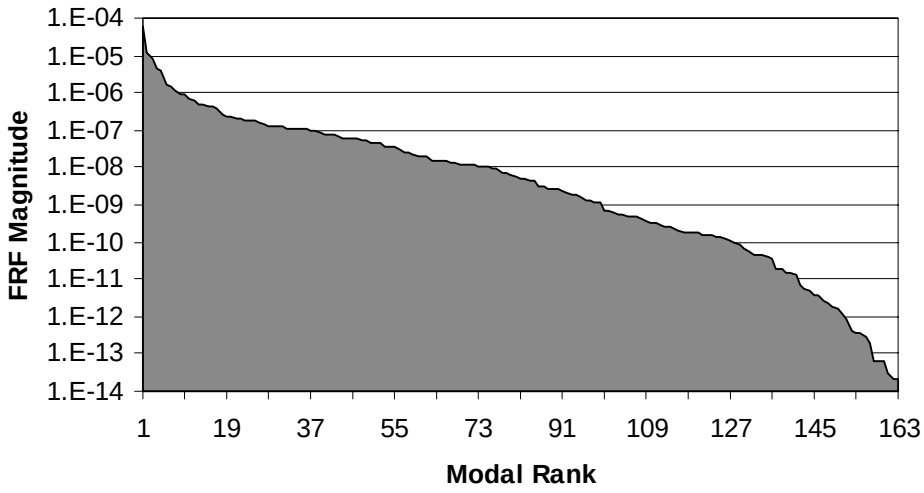

FIGURE 3.11: SADA #1 *Y*-ROTATION – HSI *X*-ROTATION RANKED MODES (1)

The ten highest magnitude modes are plotted linearly in Figure 3.12. This plot clearly shows the importance of each mode in the magnitude of the output response to a unit input. The contribution from mode #4 is approximately six times that of the next two, modes #3 and #8. Appendix C contains the FRF analysis plots for the remaining seven input-output pairs.

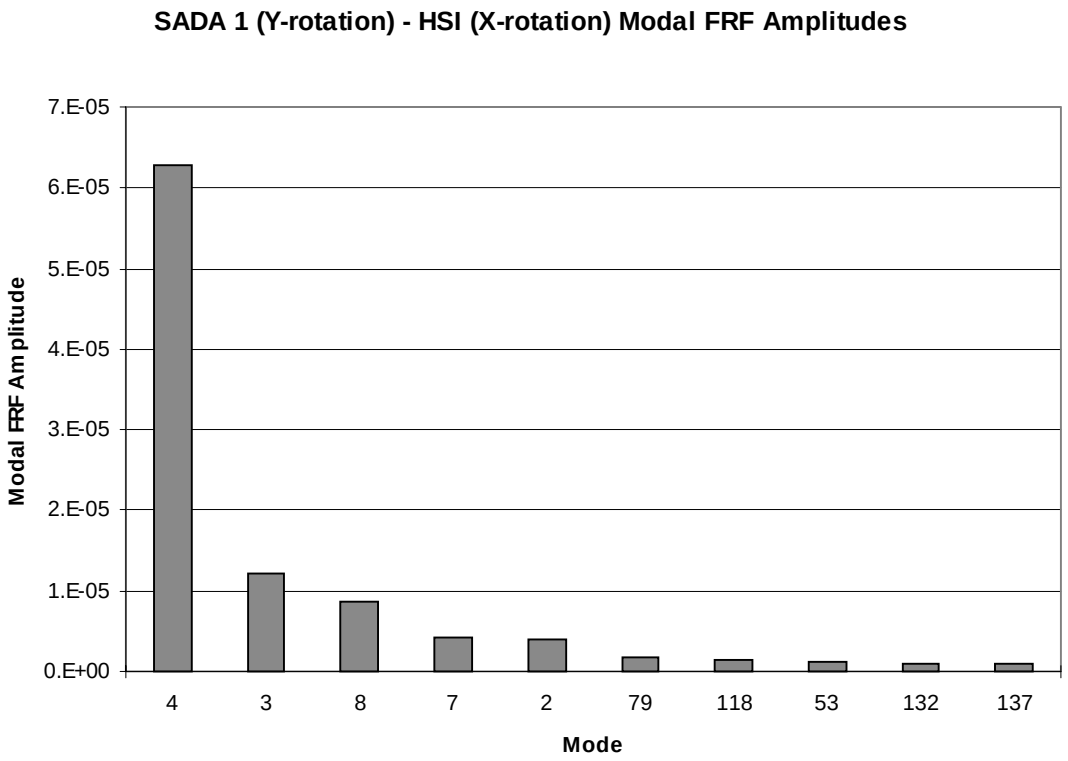

FIGURE 3.12: SADA #1 *Y*-ROTATION – HSI *X*-ROTATION RANKED MODES (2)

3.3.4 Selection of Target Modes

Table 3.6 and Figure 3.13 summarize the results of half of the FRF analysis by presenting the ten modes that provide the strongest input-output correlation in order of payload instrument *X*-rotation magnitude. The three largest contributors to both the HSI and LEISA *X*-rotations for both SADA inputs are modes #3, #4, and #8 although the modes are varied in ranking between the two SADA's. The other modes common to the four input-output pairs are #2 and #7. Of the remaining modes, #11 is ranked fourth for SADA #2 and the other modes are of decreasing importance. Therefore modes #2, #3, #4, #7, and #8 and possibly #11 would be recommended as target modes for input shaping to reduce payload instrument *X*-rotation.

TABLE 3.6: RANKED MODES FOR PAYLOAD INSTRUMENT *X*-ROTATIONS

SADA #1 Input	**Mode Number**									
HSI Output	4	3	8	7	2	79	118	53	132	137
LEISA Output	4	3	8	7	2	118	53	137	117	109
SADA #2 Input										
HSI Output	3	8	4	11	7	2	68	69	53	118
LEISA Output	3	8	4	11	7	2	118	119	53	82

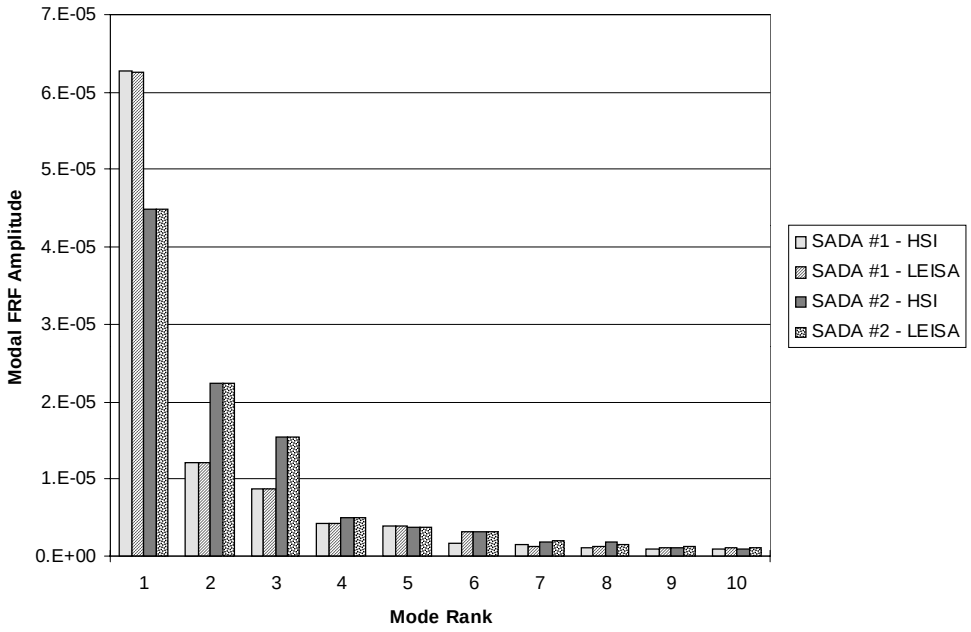

FIGURE 3.13: PAYLOAD INSTRUMENT *X*-ROTATION FRF MAGNITUDES

Table 3.7 summarizes the results of the second half of the FRF analysis by listing the 10 modes that provide the strongest input-output correlation in order of payload instrument *Y*-rotation magnitude. The two largest contributors to both the HSI and LEISA *X*-rotations for both SADA inputs are modes #3 and #4. The magnitude of the input-output correlation for both of these modes is much greater than for any of the other

modes, as shown by Figure 3.14. The only other modes common to the four input-output pairs are #40, #1, and #7. Of the remaining modes, #12 and #11 are ranked fourth for SADA #1 and SADA #2 respectively, and the remainder are of decreasing importance. Modes #3 and #4 are the most important and modes #1, #7, #11, #12, and #40 are of secondary importance as target modes for input shaping to reduce payload instrument *Y*-rotation.

TABLE 3.7: RANKED MODES FOR PAYLOAD INSTRUMENT *Y*-ROTATIONS

SADA #1 Input	**Mode Number**									
HSI Output	4	3	12	40	1	7	117	97	109	79
LEISA Output	4	3	12	40	1	7	117	97	79	109
SADA #2 Input										
HSI Output	3	4	11	40	68	69	1	7	43	8
LEISA Output	3	4	11	40	68	69	1	7	43	8

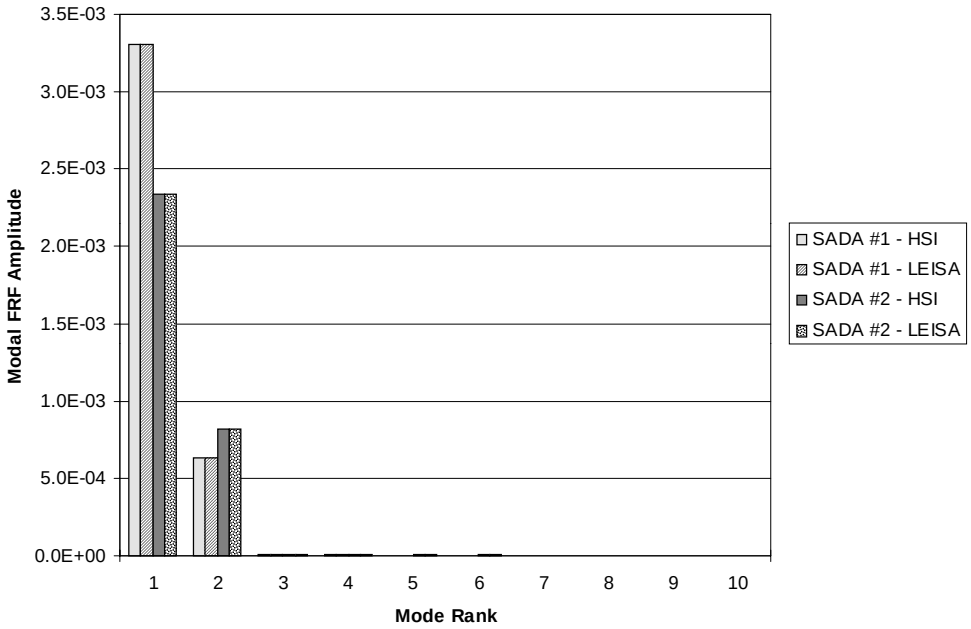

FIGURE 3.14: PAYLOAD INSTRUMENT *Y*-ROTATION FRF MAGNITUDES

4 Simulations And Results

The analysis technique used to evaluate the structural vibrations due to the SADA torque inputs is presented and then the structural responses and calculated vibration levels for the two baseline simulations are discussed. The application to the Lewis spacecraft of the pole-zero cancellation technique is introduced and the results from three vibration control simulations are included. These examples illustrate the vibration control effects of pole-zero cancellation and a method for increasing shaper robustness to errors in system identification.

4.1 Jitter Analysis Method

Motion of the solar array panels must be accomplished without exciting structural modes beyond acceptable jitter for the various payloads onboard. *Jitter* is usually defined as the absolute value of the peak-to-peak change in the displacement or rotation of a particular point on the spacecraft during a period of time called a *jitter window*. As an example, a jitter requirement might be "10 μradians / 1 sec" which means a maximum of 10 μradians of rotation is allowable over any one second period of time.

When the period of a sinusoidal or other periodic vibration is less than the jitter window, the vibration will complete at least one full cycle during the jitter window. The resulting jitter would then equal the peak-to-peak amplitude of the vibration. When the jitter window is less time than the vibration period, the jitter also depends on the phase of the vibration in the jitter window as well as the vibration amplitude. Therefore, careful

selection of jitter windows can restrict the contributions of vibrations below the *jitter cutoff frequency*, which is defined here as the reciprocal of the jitter window.

The total time the jitter is of concern can be much longer than the jitter window. The largest jitter value that occurs during the total time of interest is known as the *maximum jitter*. Continuing the previous example, let the 10 μradians / 1 sec jitter requirement be prescribed for total time of interest of 3 seconds. In Figure 4.1, two different sinusoidal vibrations are shown and a one second long jitter window is specified. Since the 3 Hz vibration completes several cycles during the jitter window, it has a jitter that is equal to the peak-to-peak amplitude (2.5 μradians in this example) and is constant for the total time of interest. The displacement due to the 0.5 Hz vibration during the jitter window indicated is 2 μradians. However, the lower frequency vibration has a longer period than the jitter window (i.e., the vibration frequency is below the jitter cutoff frequency), and therefore the maximum displacement within the jitter window also depends on the phase of the vibration.

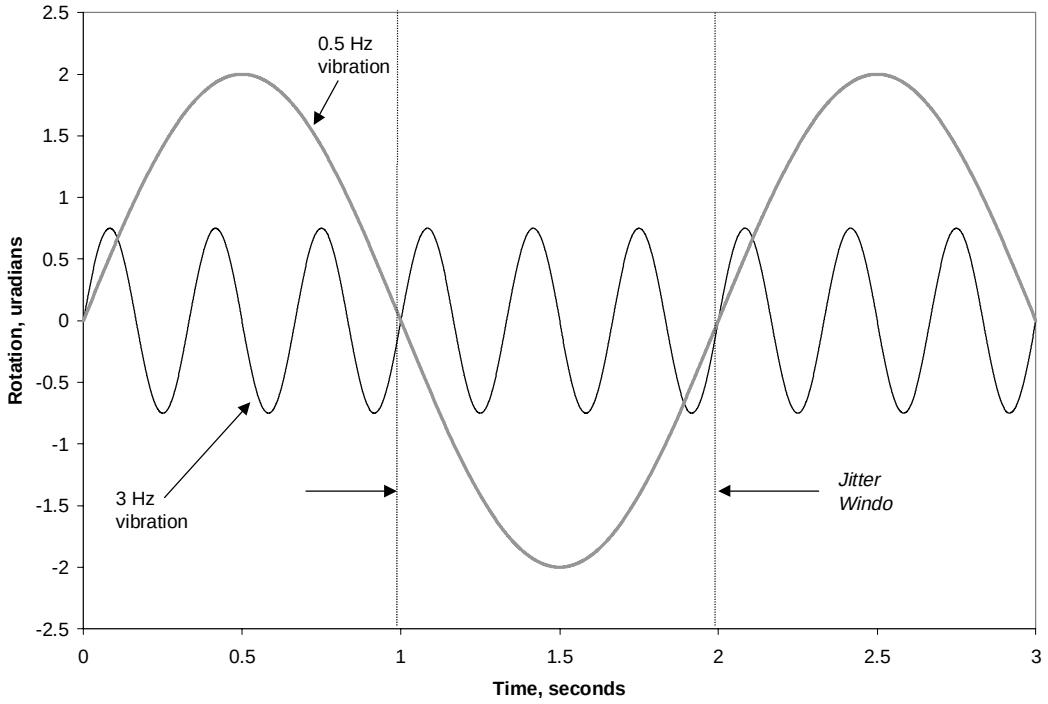

FIGURE 4.1: JITTER ANALYSIS EXAMPLE (1)

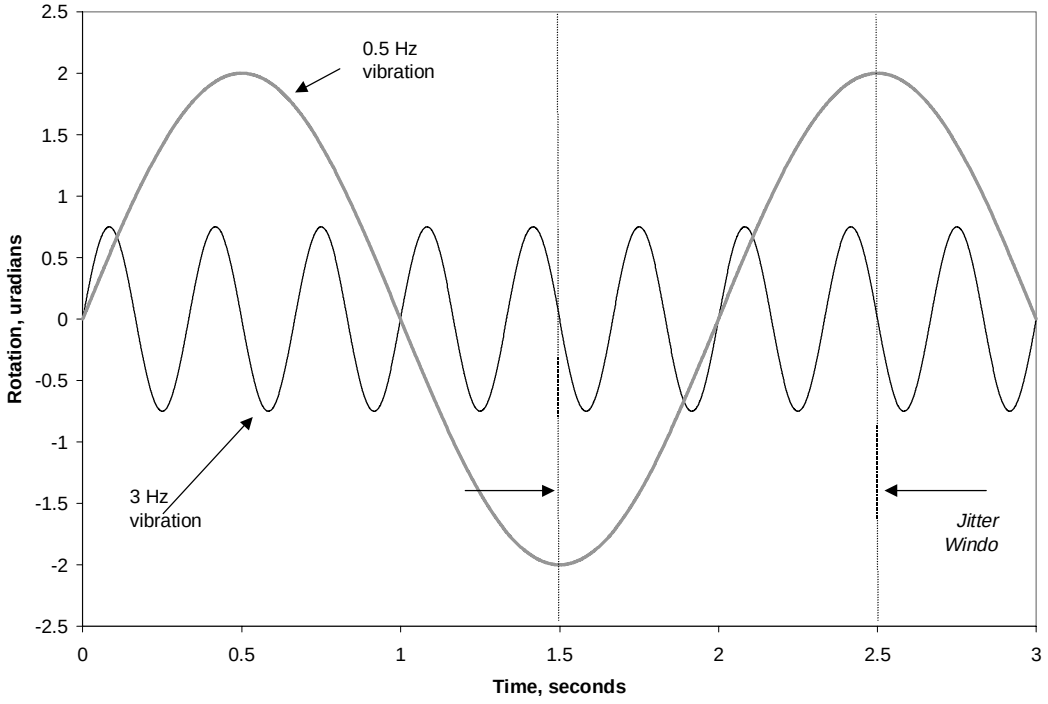

FIGURE 4.2: JITTER ANALYSIS EXAMPLE (2)

For a one second jitter window from 1.5 to 2.5 seconds the displacement for the 0.5 Hz vibration would double to 4 μradians as shown in Figure 4.2. If the jitter window is "slid" in this manner along the total time of interest the maximum jitter for all possible jitter windows can be found. More computationally efficient means of calculating jitter [5] were used for this research but the result is the same. Since 4 μradians is the maximum jitter value, these example vibrations would satisfy the 10 μradians / 1 second jitter requirement for the entire time shown. Only the maximum rotation over all possible jitter windows is of interest, and so the term *jitter* alone will be used to refer to the maximum jitter. Jitter analysis of this nature will be used to determine the effectiveness of the vibration reduction.

4.1.1 Selection of Jitter Windows and Analysis Start Time

Use of different length jitter windows can better reveal the vibration due to a particular frequency range of modes. The shorter length windows will not allow lower frequency vibrations to complete a full cycle within the window and therefore the measured jitter due to lower frequency modes will be diminished. Table 4.1 details the jitter windows used and the corresponding cutoff frequency, and lists the modes that are above the cutoff frequency and therefore able to contribute fully within that jitter window. The modal frequencies as determined by the FEM eigensolution are listed in Appendix B.

TABLE 4.1: EFFECT OF JITTER WINDOWS ON MODAL CONTRIBUTIONS

Jitter Window, seconds	0.05	0.1	0.2	0.5	1.0	3.5
Cutoff Frequency, Hz	20	10	5	2	1	0.286
Fully Included Modes	23-163	15-163	10-163	8-163	3-163	1-163

The cutoff frequency is not an absolute demarcation, however. By strict calculation, the 0.2 second window does not allow the full contribution of mode #9, which has a natural frequency of 4.97 Hz. However, 99.4% of one cycle at that frequency will fit in the 0.2 second jitter window and so mode #9 cannot be considered excluded from contributing significantly to jitter in that window. The longest jitter window (3.5 seconds), allows all the structural modes contained within the finite element model of Lewis to fully contribute. Jitter windows longer than this period of time will only show the additional effects of rigid body motions, which will not be reduced by this vibration control technique.

Jitter analysis was conducted initially to find the maximum jitter over the entire 160 second simulation. The "start time" of the analysis would therefore be t=0. This starting time was increased by 0.5 seconds for each subsequent analysis, up to t=156.5 seconds. Increasing the jitter analysis start times allowed transient responses from earlier SADA disturbances to dissipate and not be included in the later analyses. Since the jitter tended to decrease over the simulation time, this allowed a determination of when the jitter levels were acceptable for the remainder of the simulation.

4.2 Baseline Simulations And Jitter Analysis Results

Torque time profiles were used to simulate the SADA outputs resulting from the five stepper command sequences presented in this research. Jitter analysis using six different jitter windows was conducted on the resulting X- and Y-rotations of the two FEM nodes corresponding to the HSI and LEISA payload instruments. These 24 different analyses

were conducted over the course of the simulation and used to determine the relative effectiveness of the vibration control method in comparison to baseline results.

4.2.1 Constant Step Rate Simulation

The torque variation of a single step of the SADA rotary actuator is shown in Figure 4.3. The duration of a single step is about 1/40th of a second from beginning to end and therefore up to about a 40 Hz step rate would be expected to consist of entirely discrete operations. This is a reasonable result given that a smaller rotary stepper motor with lighter end-loading conditions was found by Jim Miller of NASA Langley Research Center [private communication] to have discrete steps up to 100 Hz. Cascading these steps at the prescribed step rate of approximately 3.16 steps or pulses per second (PPS) results in the Constant Step Rate Sequence (CSRS) torque input, a portion of which is shown in Figure 4.4. This plot illustrates the short time length and impulsive nature of the individual steps.

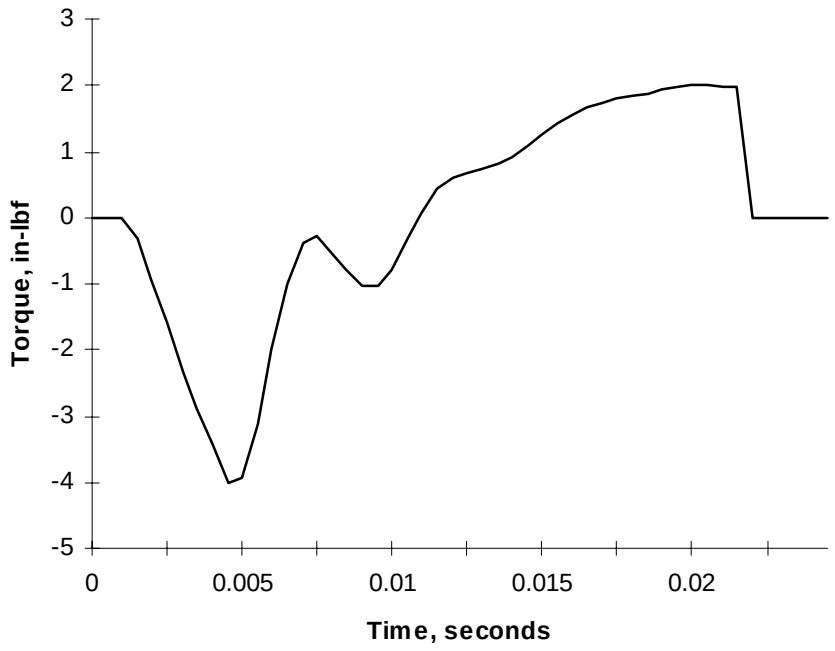

FIGURE 4.3: SINGLE STEP TORQUE TIME PROFILE

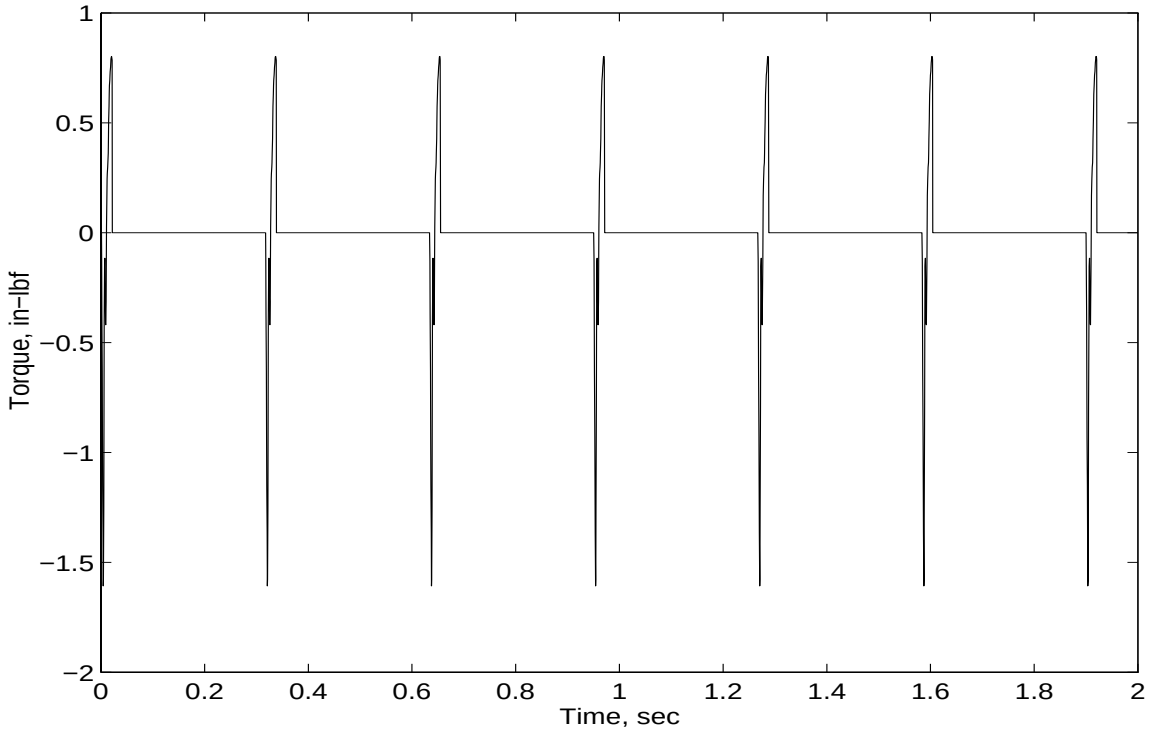

FIGURE 4.4: CSRS TORQUE TIME PROFILE, 3.16 PPS

The *X*- and *Y*-rotations of the HSI instrument are shown in Figures 4.5 and 4.6. These figures show the total response (combined rigid and flexible body terms) and the flexible body response alone. The rigid body *Y*-rotation of the HSI instrument was approximately 5,350 μradians, close to the quantity predicted by Equation 3.6. The rigid body *X*- and *Z*-rotations are approximately -102 and –13.5 μradians respectively, and this indicates that the simulated spacecraft structure transfers some energy between the coordinate directions via non-zero off-diagonal terms in the inertia matrix.

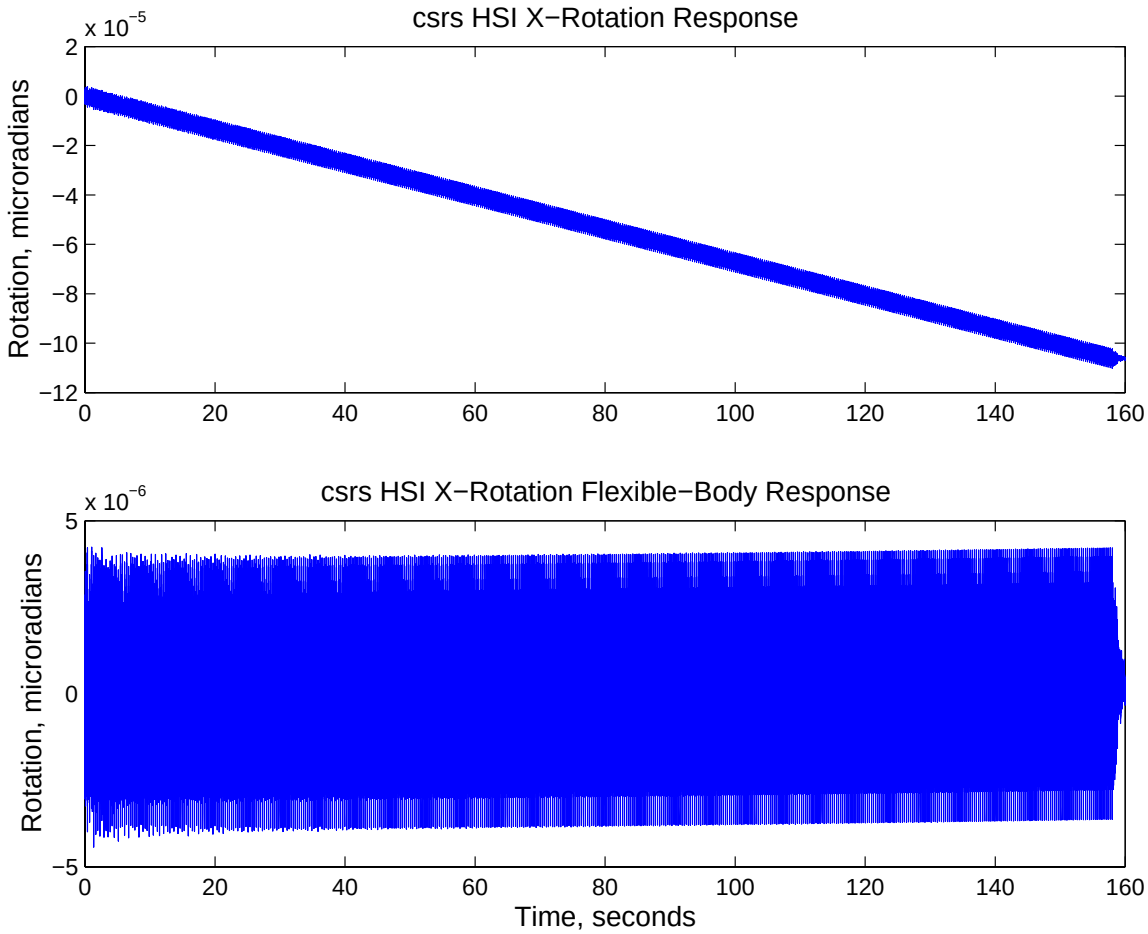

FIGURE 4.5: HSI *X*-ROTATION RESPONSE TO CSRS TORQUE INPUT

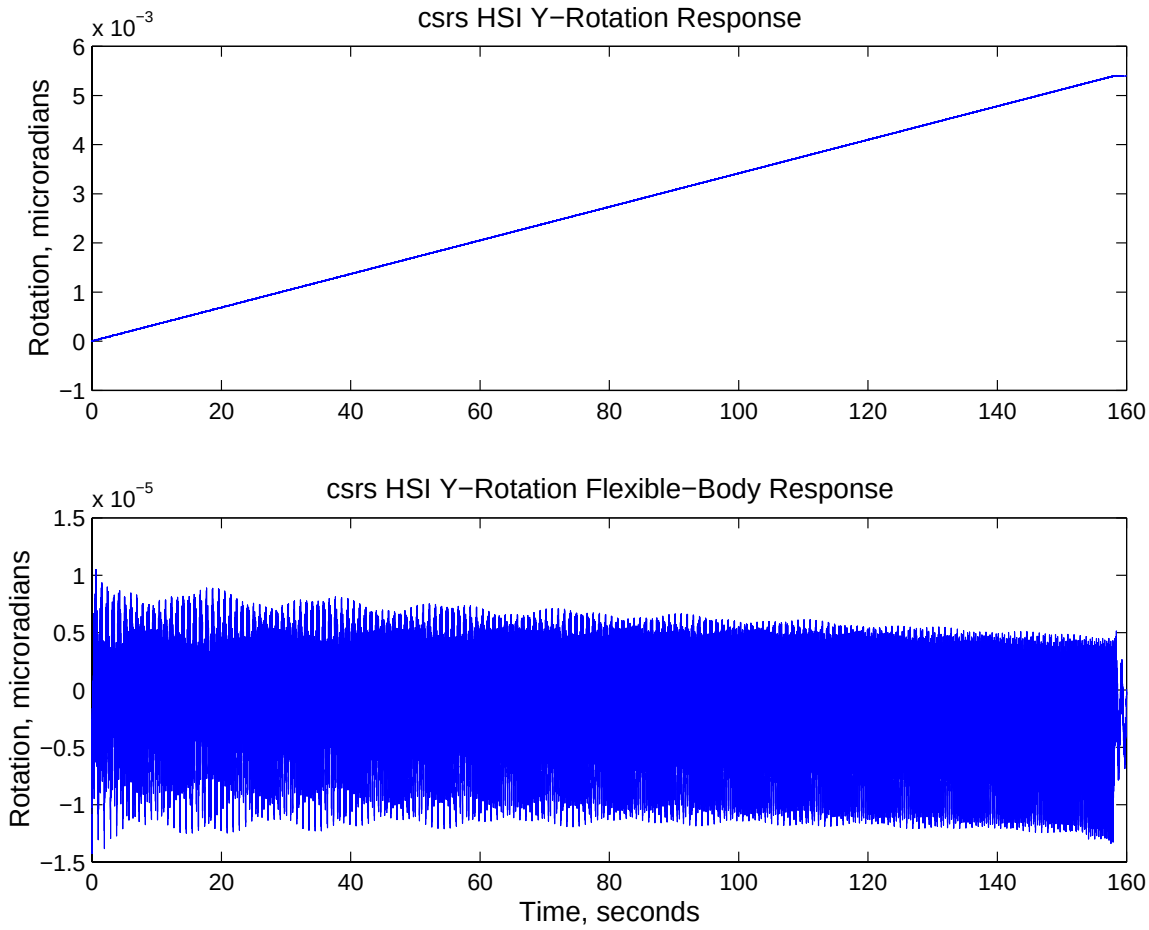

FIGURE 4.6: HSI *Y*-ROTATION RESPONSE TO CSRS TORQUE INPUT

For both instruments, the jitter response to the CSRS torque input are nearly constant values for all analysis start times. Within the simulation, the HSI and LEISA nodes achieve a steady state response almost immediately to the repetitive CSRS torque input. Table 4.2 summarizes the average jitter levels for the six jitter windows used.

The *Y*-rotation jitter levels are clearly not acceptable and have significant input from the higher frequency modes (i.e., the jitter levels only increase slightly as the jitter window is lengthened from 0.05 seconds to 3.5 seconds). The *X*-rotation is much less, and is due

to the structural transfer of rotational energy since the input torque is acting about the *Y*-axis only.

TABLE 4.2: CSRS JITTER ANALYSIS RESULTS

Jitter Windows in seconds		**HSI X-rotation**	**LEISA X-rotation**	**HSI Y-rotation**	**LEISA Y-rotation**
0.05	*Jitter, μradians*	7.20	5.91	16.96	51.95
	% of Jitter Limit	72.0%	19.7%	169.6%	173.2%
0.1	*Jitter, μradians*	7.20	5.91	16.99	51.95
	% of Jitter Limit	72.0%	19.7%	169.9%	173.2%
0.2	*Jitter, μradians*	7.20	5.91	17.56	51.95
	% of Jitter Limit	72.0%	19.7%	175.6%	173.2%
0.5	*Jitter, μradians*	7.79	5.97	18.87	54.31
	% of Jitter Limit	77.9%	19.9%	188.7%	181.0%
1	*Jitter, μradians*	7.79	5.99	19.01	54.32
	% of Jitter Limit	77.9%	20.0%	190.1%	181.1%
3.5	*Jitter, μradians*	7.80	6.00	19.07	54.43
	% of Jitter Limit	78.0%	20.0%	190.7%	181.4%

4.2.2 Minimum Actuation Time Simulation

A single actuator sequence consisting of 500 consecutive steps at the maximum rate of 200 pulses per second (PPS) was simulated. The first 0.5 seconds of the 200 PPS torque output is shown in Figure 4.7. This achieves the required 10° of rotation in a minimum time of 2.5 seconds and would allow a maximum amount of time for structural damping to dissipate the vibrational energy. The stepper motor torque output at high step rates loses its distinct step characteristics. The response of the HSI to the MATS torque input is shown in Figures 4.8 and 4.9.

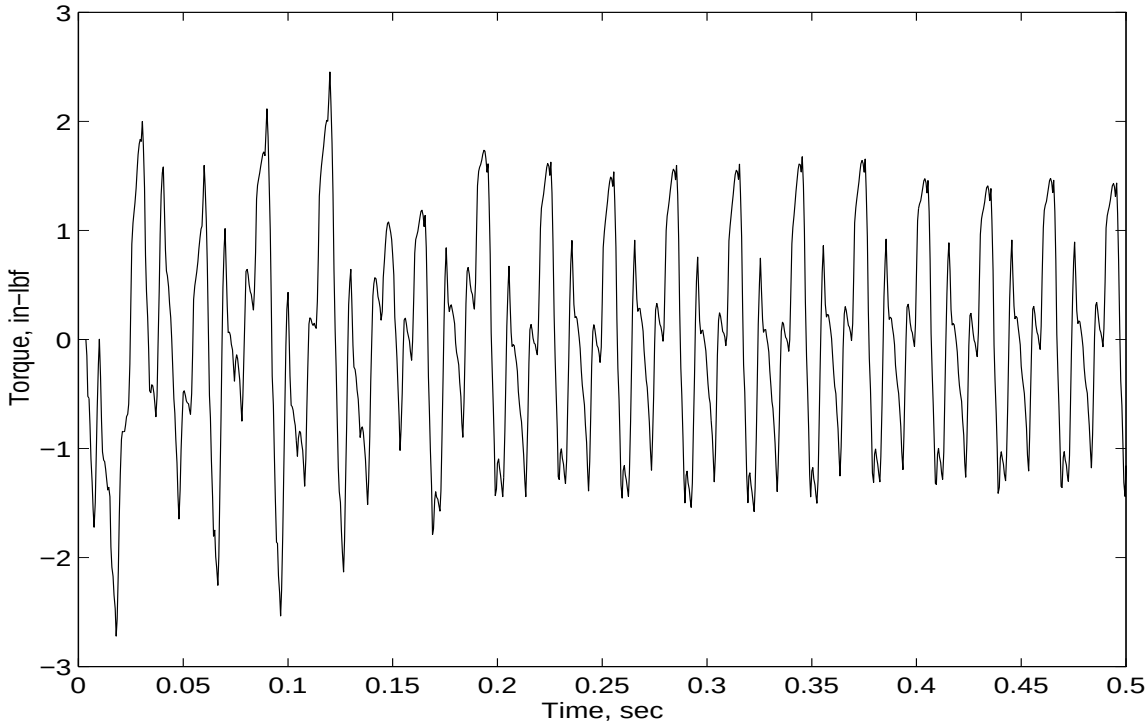

FIGURE 4.7: MATS TORQUE TIME PROFILE, 200 PPS

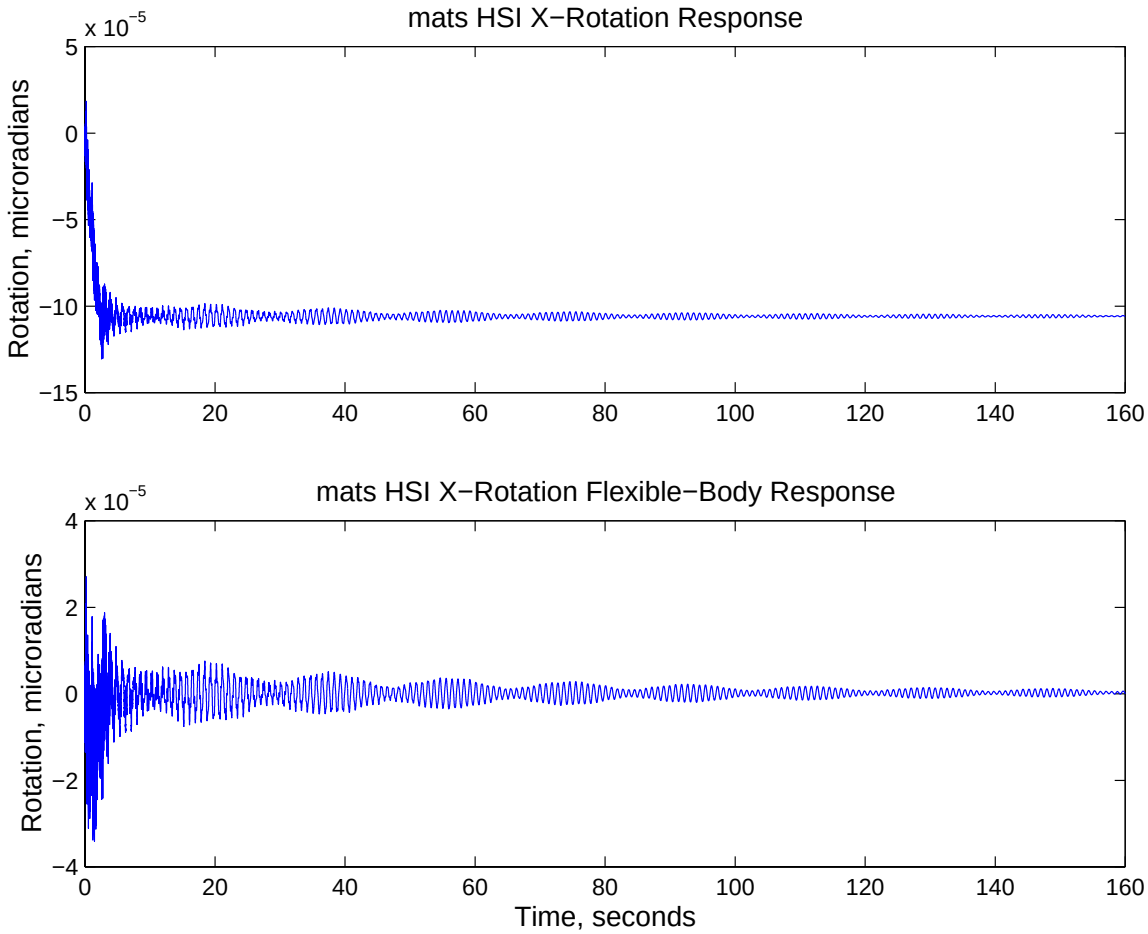

FIGURE 4.8: HSI *X*-ROTATION RESPONSE TO MATS TORQUE INPUT

The rigid body *Y*-rotation for the spacecraft is approximately 5,350 μradians, agreeing with the response from the CSRS input. After the SADA input is complete at t=2.5 seconds, the spacecraft structure was allowed to settle until t=160 seconds. The HSI *Y*-rotation response during the settling period consists of a superposition of decaying sinusoids from the simulated structural modes. Jitter analysis was conducted as stated previously over the entire simulation time.

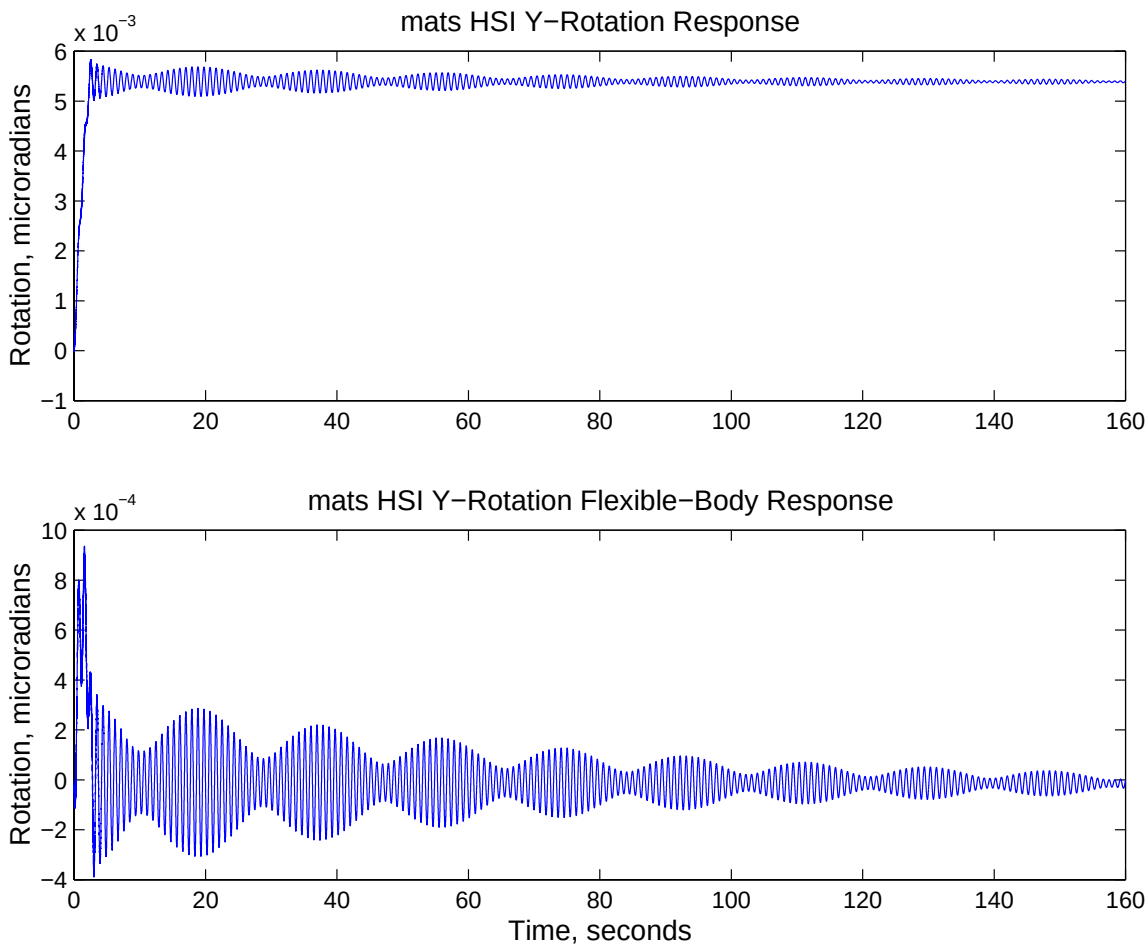

FIGURE 4.9: HSI *Y*-ROTATION RESPONSE TO MATS TORQUE INPUT

The jitter analysis results for both the CSRS and MATS simulations are summarized in Figures 4.10 through 4.13, and show the jitter values as percentages of the instrument jitter limits. Jitter analyses of the MATS simulation response with a start time of t=0 had the largest values. The jitter levels steadily decreased as the analysis start time progressed and the last jitter analyses, with a start time of t=156.5 seconds, had the minimum value.

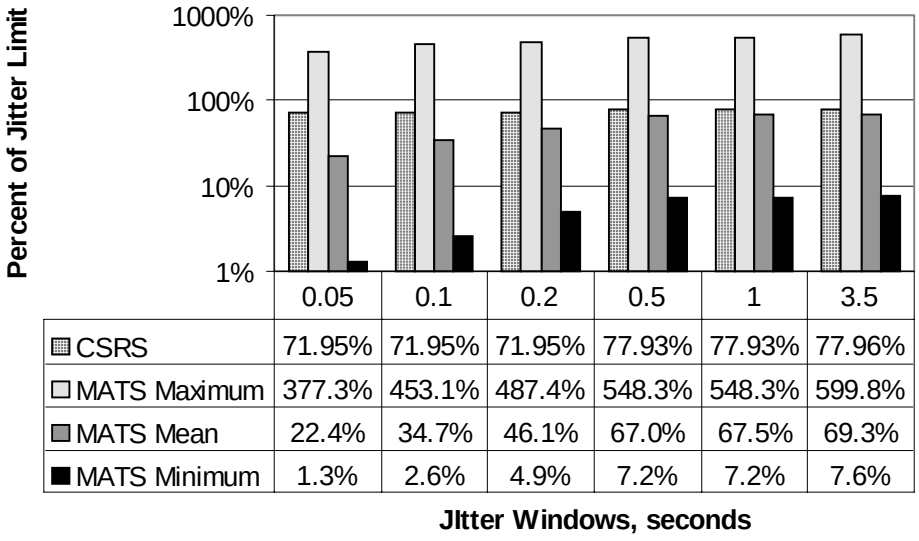

	0.05	0.1	0.2	0.5	1	3.5
CSRS	71.95%	71.95%	71.95%	77.93%	77.93%	77.96%
MATS Maximum	377.3%	453.1%	487.4%	548.3%	548.3%	599.8%
MATS Mean	22.4%	34.7%	46.1%	67.0%	67.5%	69.3%
MATS Minimum	1.3%	2.6%	4.9%	7.2%	7.2%	7.6%

FIGURE 4.10: HSI *X*-ROTATION BASELINE JITTER LEVELS

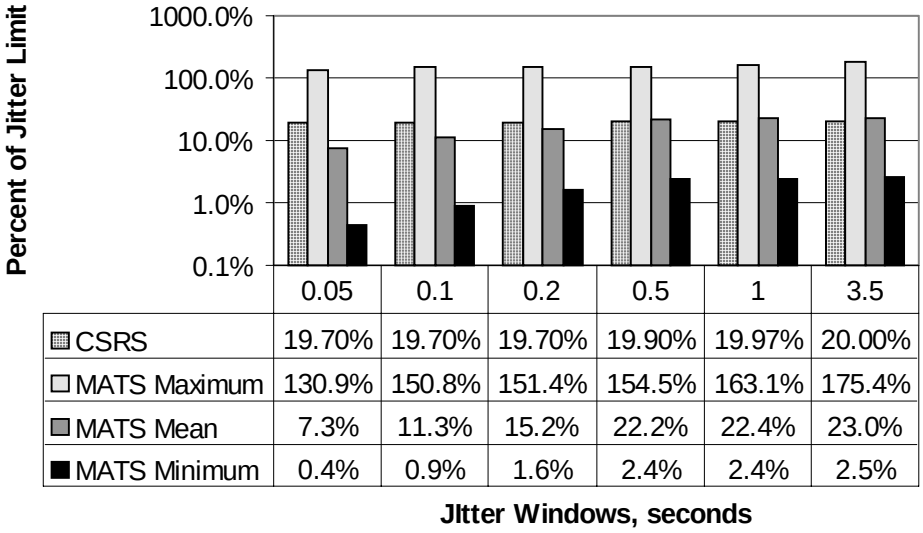

	0.05	0.1	0.2	0.5	1	3.5
CSRS	19.70%	19.70%	19.70%	19.90%	19.97%	20.00%
MATS Maximum	130.9%	150.8%	151.4%	154.5%	163.1%	175.4%
MATS Mean	7.3%	11.3%	15.2%	22.2%	22.4%	23.0%
MATS Minimum	0.4%	0.9%	1.6%	2.4%	2.4%	2.5%

FIGURE 4.11: LEISA *X*-ROTATION BASELINE JITTER LEVELS

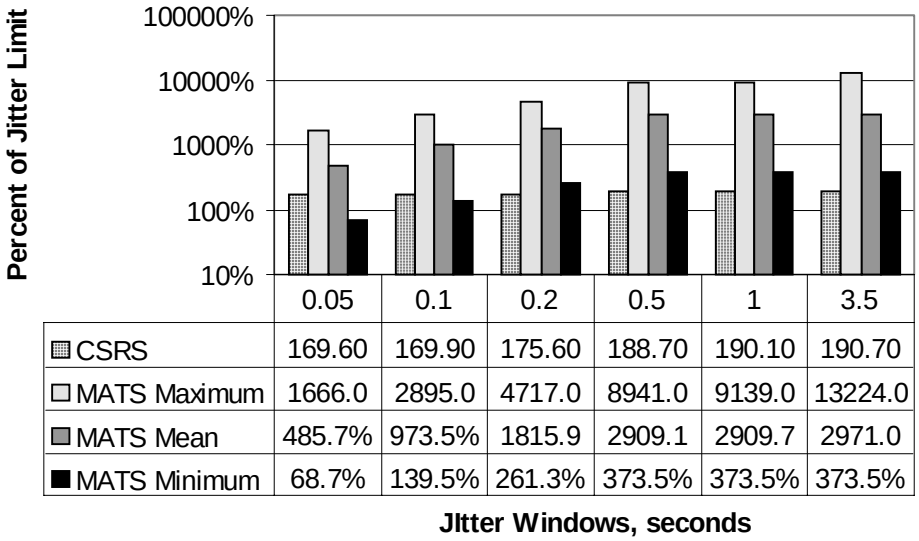

	0.05	0.1	0.2	0.5	1	3.5
CSRS	169.60	169.90	175.60	188.70	190.10	190.70
MATS Maximum	1666.0	2895.0	4717.0	8941.0	9139.0	13224.0
MATS Mean	485.7%	973.5%	1815.9	2909.1	2909.7	2971.0
MATS Minimum	68.7%	139.5%	261.3%	373.5%	373.5%	373.5%

FIGURE 4.12: HSI *Y*-ROTATION BASELINE JITTER LEVELS

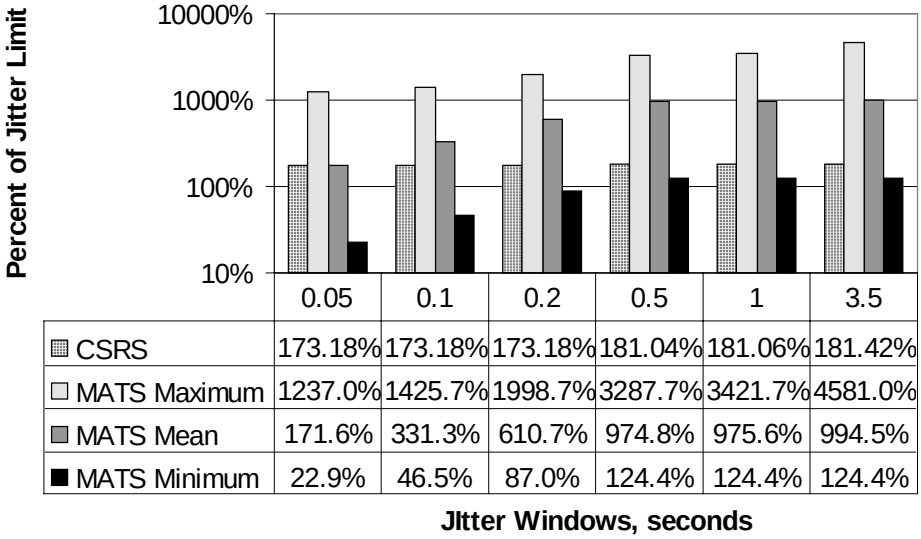

	0.05	0.1	0.2	0.5	1	3.5
CSRS	173.18%	173.18%	173.18%	181.04%	181.06%	181.42%
MATS Maximum	1237.0%	1425.7%	1998.7%	3287.7%	3421.7%	4581.0%
MATS Mean	171.6%	331.3%	610.7%	974.8%	975.6%	994.5%
MATS Minimum	22.9%	46.5%	87.0%	124.4%	124.4%	124.4%

FIGURE 4.13: LEISA *Y*-ROTATION BASELINE JITTER LEVELS

Examination of the MATS simulation response reveals that the average and minimum *X*-rotations are below the desired jitter limits, but the corresponding *Y*-rotations generally exceed the limits. The HSI minimum *Y*-rotation jitter values are above the instrument jitter

limit for the 5 longer jitter windows, with only the 0.05 second window having an acceptable minimum jitter value (68.7% of the jitter limit, see Figure 4.12). Structural damping (modeled as 0.2% for all modes) decreased the minimum LEISA *Y*-rotation jitter for the 0.5, 1.0 and 3.5 second windows to 124.4% of the instrument jitter limit (see Figure 4.13). These results illustrate that with a lightly damped system the structural modes can cause sustained vibratory motion that could reduce the data quality from the payload instruments and a more advanced command sequence could be employed to directly address this concern.

4.3 Shaped Input Simulations and Results

The implementation of the *z*-plane pole-zero cancellation theory for the Lewis spacecraft SADA is presented. To aid in the selection of input shaper solutions, additional calculations using four different criteria are performed. These calculations rank the many possible sets of stepper motor sequences produced by the vibration control theory. The proposed solutions were then transformed into equivalent SADA torque time profiles and the Lewis spacecraft response was simulated using the model introduced in Section 3. Jitter analysis was then performed to evaluate the performance of each sequence in reducing vibration. The results from three of these simulations are presented in Sections 4.3.

The target modes were selected as discussed in Section 3.3. The corresponding target poles were calculated from the modal information according to Equation 2.4 and the discrete time transfer function was constructed. This transfer function was transformed to the Laplace *s*-domain and the numerator coefficients were extracted. These coefficients

are the impulse amplitudes of Equation 2.11, and solutions with any negative impulses were removed. This is not essential, but removing solutions with negative impulses ensured that the SADA would always move the solar arrays in the desired direction. Other researchers have investigated the use of negative impulses to shorten the time interval T between impulses [8] but this was not investigated for the Lewis spacecraft. The impulse amplitudes of the remaining solutions were normalized to sum to one. The four ranking criteria of Equations 2.12 through 2.15 were calculated and based on these rankings, one or more solutions were selected and used with the PLATSIM Lewis simulation.

The stepper sequence(s) defined by a given input shaper solution was then used to construct an SADA torque time profile. This torque profile contained the desired number of steps in each sequence and had each sequence spaced in time at a center-to-center distance equal to T as shown in Figure 2.6. The simulated SADA torque was applied to the SADA nodes within an open-loop simulation (to remove any effects from the Lewis spacecraft ACS) and the resulting jitter levels of the HSI and LEISA payload instruments examined to evaluate the vibration reduction.

The results for all eight input-output pairs must be considered in the selection of target modes for the input shaper, since the one shaper is to attempt to reduce the four output vibrations. The X-rotations from the constant step rate and single sequence simulations were below the jitter limits for all jitter windows, and so it was desired to maintain that performance. At the same time, the simulated Y-rotations were up to 1.5 times the jitter limits and so that performance had to be improved. Comparison of the FRF analysis plots show that a torque input about the Y-axis by either of the SADA's has a

much greater impact on the *Y*-rotation of the payload instruments than on the *X*-rotation of that node. Therefore, the controllability of the *Y*-rotations by the SADA torque is greater.

4.3.1 Vibration Control Sequence #1

Table 4.3 shows the information that fully describes Vibration Control Sequence #1 (VCS #1) as implemented for the Lewis spacecraft. The *Target Modes* are the modes selected using the FRF analysis of Section 3.3. The *Target Robustness* is the total number of zeros that are placed over the corresponding system poles by the shaper transfer function. The *Impulse Amplitudes* listed are the normalized values, and the *Step Time* is the time at which each step sequence begins, adjusted as explained in Section 2.4. The system poles corresponding to the eight target modes are plotted in the *z*-plane in Figure 4.14, and the shaper zeros are placed exactly over the system poles in this command sequence. The first 30 seconds of the SADA torque for VCS #1 is shown in Figure 4.15, with the torque being zero from t=30 to t=160 seconds.

TABLE 4.3: VIBRATION CONTROL SEQUENCE #1 DATA

Target Modes	#2	#3	#4	#7	#8	#11	#12	#40
Target Robustness	1	2	2	1	2	1	1	1
Total # Impulses	23							
Sampling Time, T	1.14 seconds							
Step Rate	200 PPS							

Impulse #	*Impulse Amplitudes*	*# Steps*	*Impulse Time, seconds*	*Step Time, seconds*
1	0.023073	12	0	0
2	0.03148	16	1.14	1.125
3	0.036154	18	2.28	2.255
4	0.08806	44	3.42	3.325
5	0.051758	26	4.56	4.505
6	0.040324	20	5.7	5.655
7	0.094088	47	6.84	6.7225
8	0.012803	6	7.98	7.96
9	0.047849	24	9.12	9.05
10	0.113721	57	10.26	10.1025
11	0.037566	19	11.4	11.3325
12	0.09349	47	12.54	12.3975
13	0.100759	50	13.68	13.525
14	0.022169	11	14.82	14.7575
15	0.050666	25	15.96	15.8575
16	0.036388	18	17.1	17.01
17	0.008973	4	18.24	18.18
18	0.032492	16	19.38	19.285
19	0.029042	15	20.52	20.4225
20	0.019262	10	21.66	21.57
21	0.017665	9	22.8	22.7075
22	0.009763	5	23.94	23.8525
23	0.002455	1	25.08	24.9975
Totals	1.00	500		

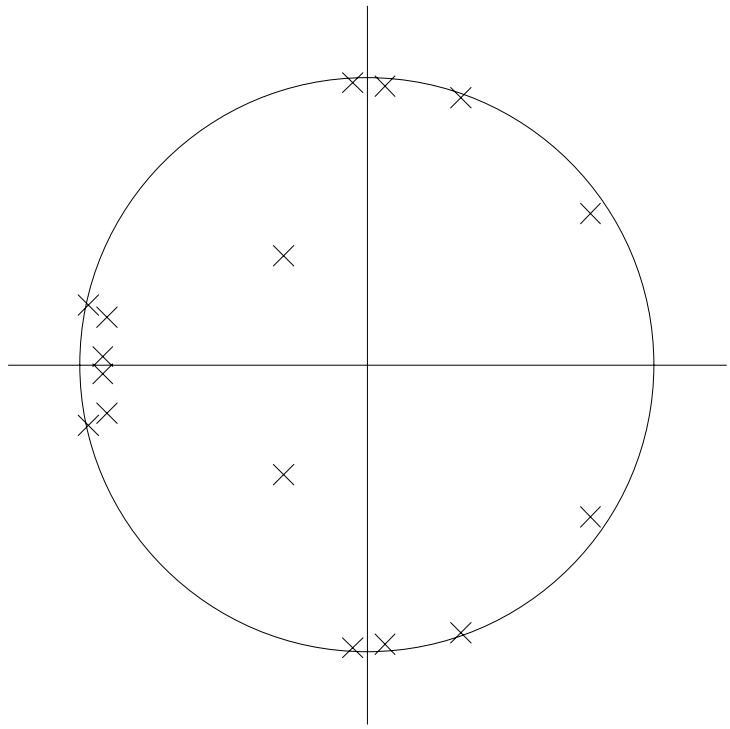

FIGURE 4.14: SYSTEM POLES IN THE *Z*-PLANE (*T*=1.14 SECONDS)

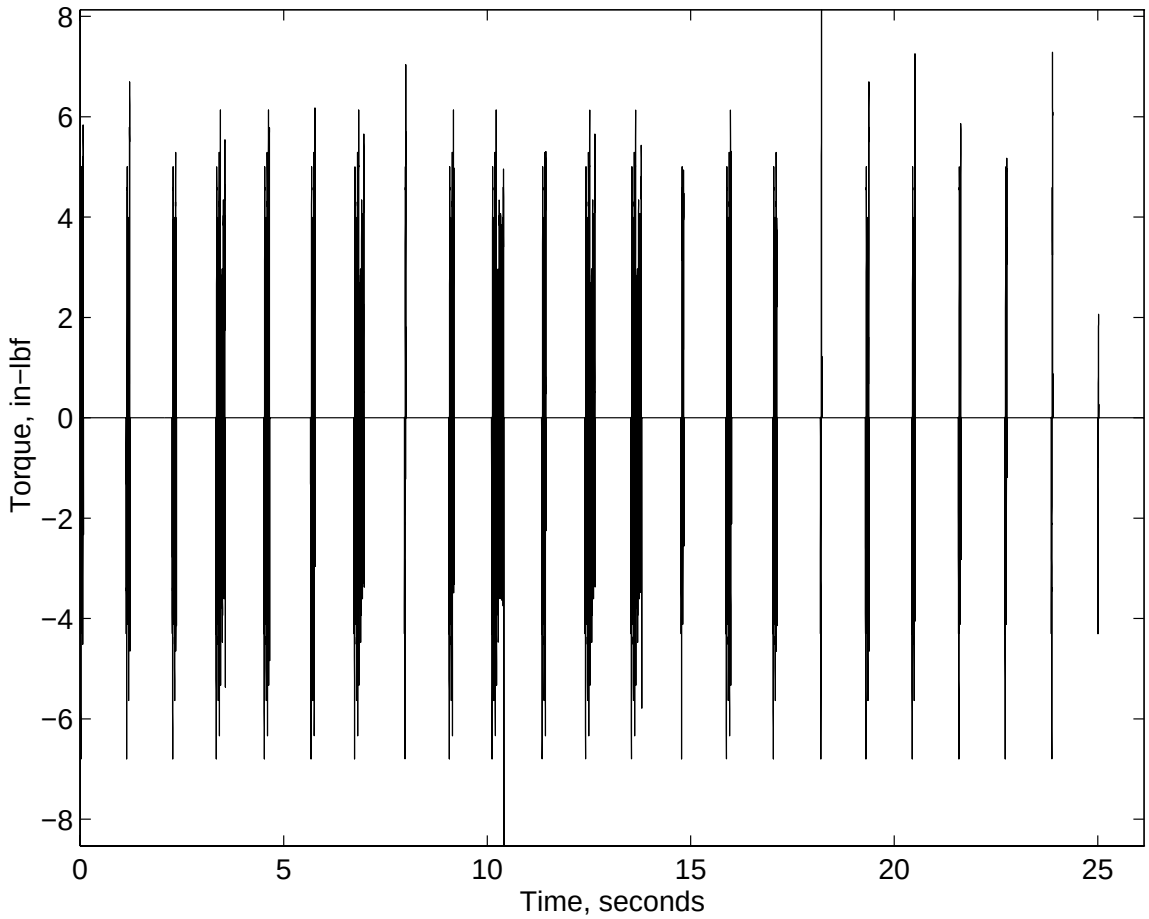

FIGURE 4.15: SADA TORQUE TIME PROFILE FOR VCS #1

The HSI *X*- and *Y*-rotations resulting from the VCS #1 input torque are depicted in Figures 4.16 and 4.17. The LEISA response was nearly identical within the scale of the graph. The total rigid body *Y*-rotation of the spacecraft agrees quite closely with the prediction of Equation 3.6 and is approximately 5,350 μradians.

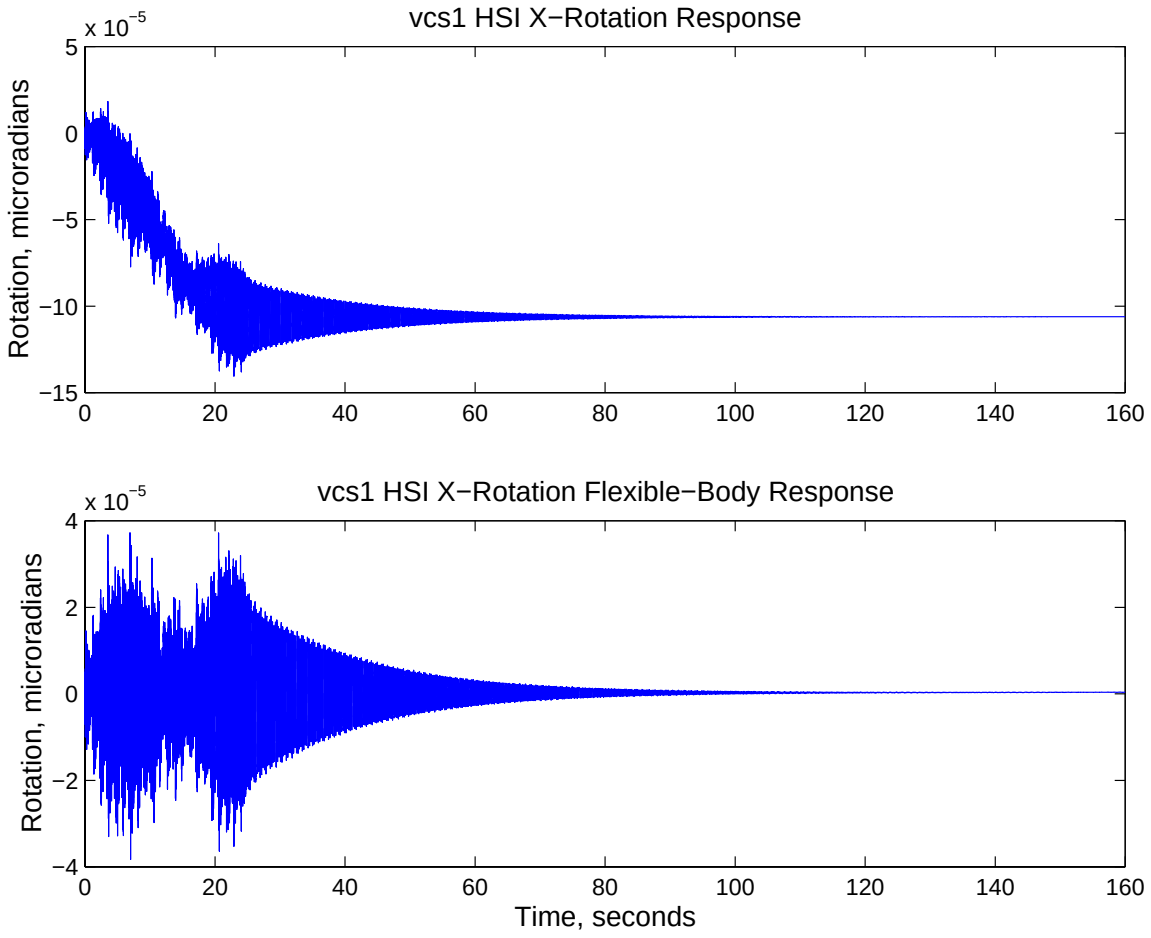

FIGURE 4.16: HSI *X*-ROTATION RESPONSE TO VCS #1

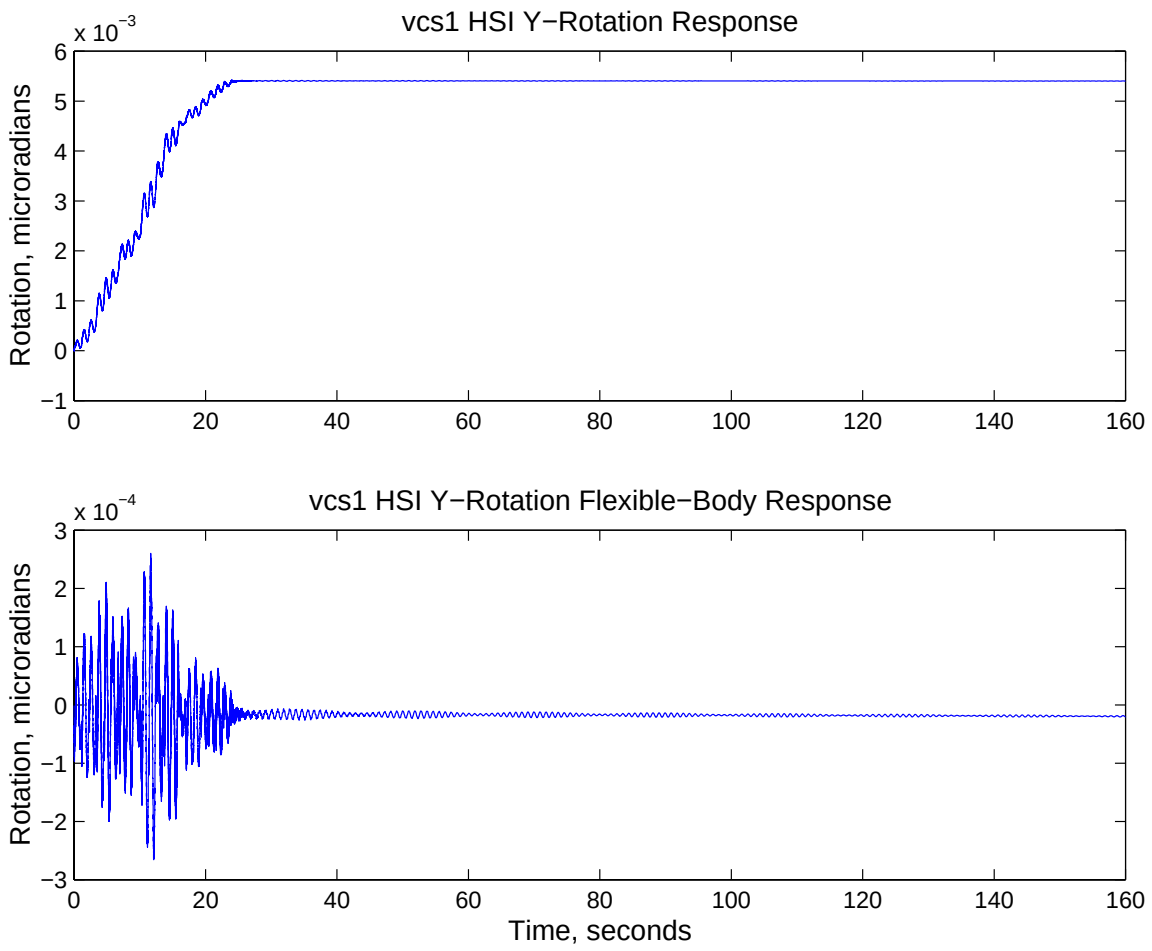

FIGURE 4.17: HSI *Y*-ROTATION RESPONSE TO VCS #1

Jitter analysis of the HSI and LEISA responses was then performed. The jitter values for a 3.5-second window are shown in Figures 4.18 through 4.21. These plots are representative of the performance of the VCS #1 step commands in comparison to the CSRS and MATS step commands introduced in Section 3. The *X*-rotation jitter is plotted on a linear scale, while the *Y*-rotation jitter is plotted on a semi-log scale to display the larger variation in the jitter results. The staircase nature of the plots is an effect of the jitter analysis method since the maximum jitter quantity from the given analysis start time until

the end of the simulation is displayed. A solid gray line at the 100% level on all four plots marks the jitter limit.

For all three simulations, the jitter levels are fairly constant while the SADA torque is non-zero. Referring to the 3.5-second jitter window results shown in Figures 4.18 and 4.19, the VCS #1 simulation *X*-rotation jitter begins (at *t*=0 seconds) with values that are greater than the MATS simulation values. For both the MATS and VCS #1 simulations, the jitter levels drop very quickly once the SADA input torque ceases. For the MATS simulation, this event occurs at *t*=2.5 seconds, but doesn't occur for the VCS #1 simulation until approximately *t*=25 seconds. The payload instrument jitter requirements are therefore not satisfied in *X*-rotation by the VCS #1 simulation until *t*=50 seconds for the HSI and *t*=33 seconds for the LEISA.

However, the input shaper was primarily designed to reduce the problematic *Y*-rotation jitter levels (and the *X*-rotations of the payload instruments are not very controllable by the torque about the *Y*-axis produced by the SADA, as revealed by the FRF analysis of Section 3). The *Y*-rotation jitter analysis results are shown for the 3.5-second window in Figures 4.20 and 4.21. For the VCS #1 simulation, the *Y*-rotation jitter levels are approximately constant when the SADA torque is non-zero and then drop off very sharply. The large decrease in *Y*-rotation jitter levels immediately following the end of the SADA input during the VCS #1 simulation is due to the shaping of the SADA input. The HSI and LEISA instruments have acceptable *Y*-rotation jitter levels by *t*=56 and 26 seconds, respectively. In contrast, the MATS simulation jitter levels decrease at a much smaller rate due to structural damping only and never achieve acceptable jitter levels. The

CSRS simulation jitter levels are approximately constant at 190.7% and 181.4% of the jitter requirements for the HSI and LEISA respectively. In general, the VCS #1 step sequence causes both the *X*-rotation and *Y*-rotation jitter levels to be within the payload instrument requirements shortly after the SADA step commands are completed.

Since angular momentum is conserved in the physical system, the rigid body rotation about the Y-axis of the spacecraft bus from even a single step of the SADA is of a significant quantity (10.3 μradians, which corresponds to approximately 103% and 33% of the HSI and LEISA jitter requirements respectively). Therefore, any action by the SADA would preclude the optimal operation of the payload instruments. The VCS #1 step commands cause a minority of the simulation time to be spent at the higher jitter levels and allow more time for a vibration sensitive operation to be performed.

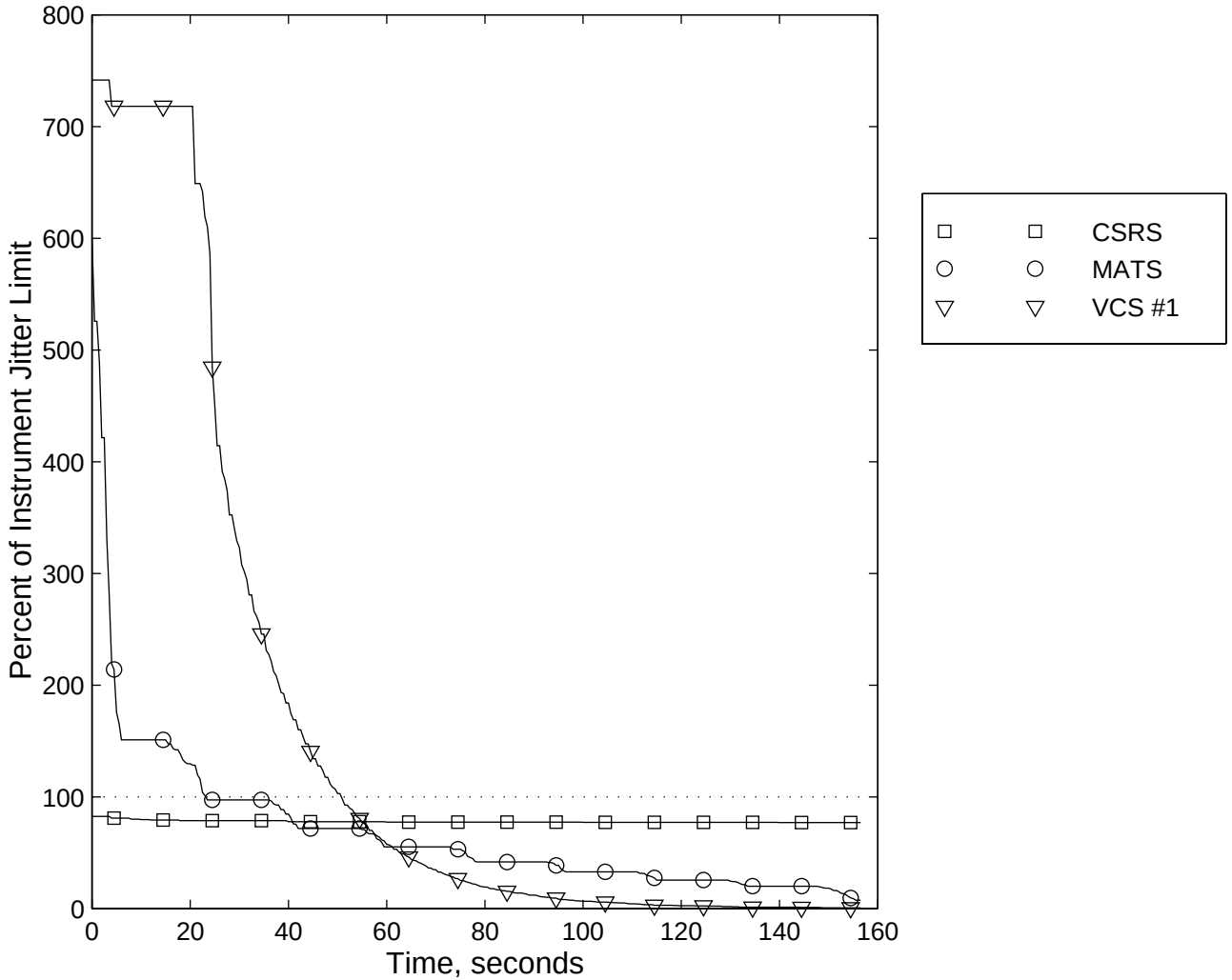

FIGURE 4.18: HSI *X*-ROTATION JITTER ANALYSIS RESULTS (3.5-SECOND WINDOW)

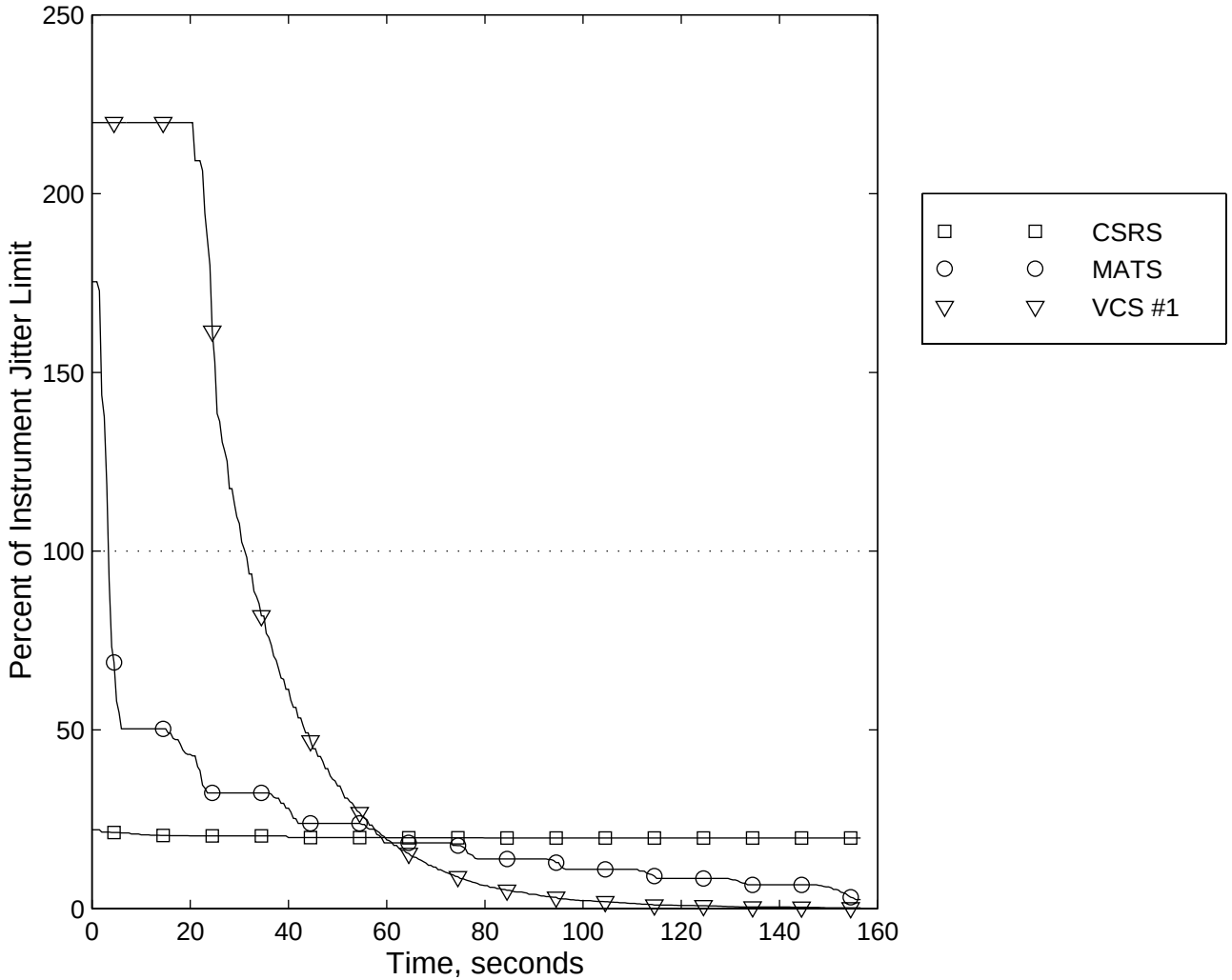

FIGURE 4.19: LEISA *X*-ROTATION JITTER ANALYSIS RESULTS (3.5-SECOND WINDOW)

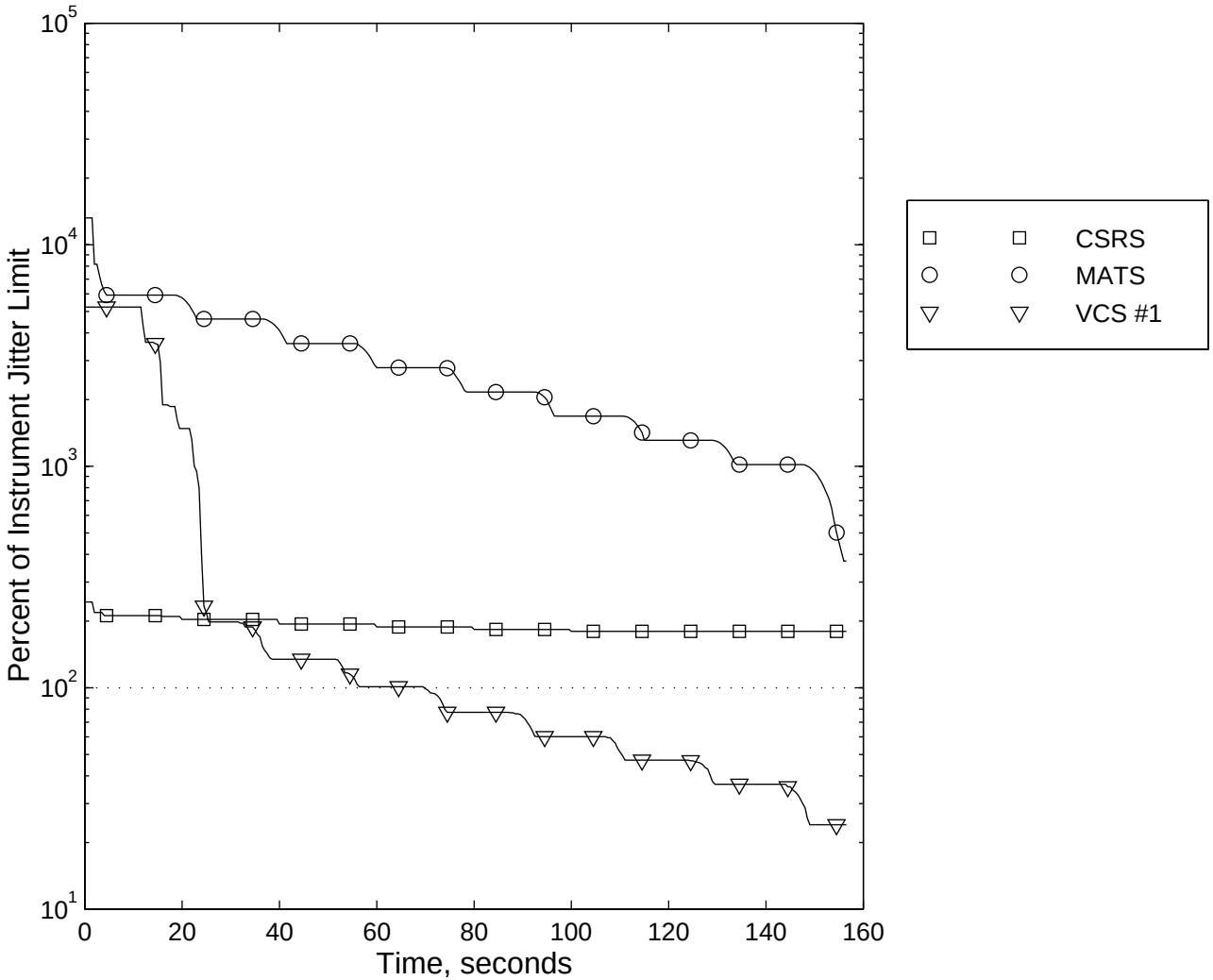

FIGURE 4.20: HSI *Y*-ROTATION JITTER ANALYSIS RESULTS (3.5-SECOND WINDOW)

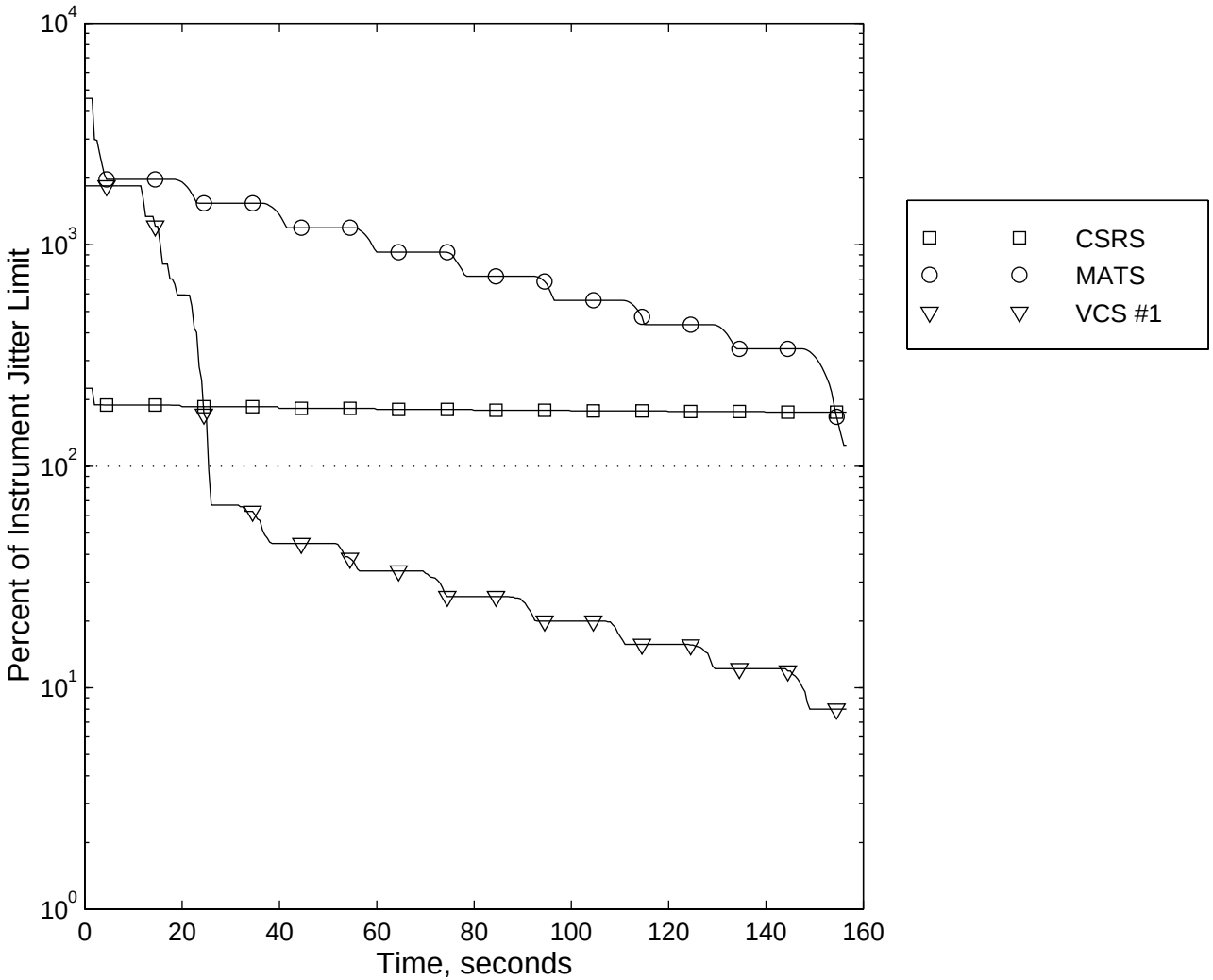

FIGURE 4.21: LEISA *Y*-ROTATION JITTER ANALYSIS RESULTS (3.5-SECOND WINDOW)

4.3.2 Vibration Control Sequence #2

The VCS #1 simulation had perfect identification of the system poles, allowing the shaper zeros to be collocated with the target poles for maximum effectiveness in vibration reduction. However, significant errors in the identification of even moderately complex structures are possible and a robust control system must be able to operate well despite these inaccuracies. The technique of using additional shaper zeros to compensate for errors in the identification of the system poles is presented in this section.

Table 4.4 shows the data for a second vibration reducing solution as implemented for the Lewis spacecraft. The final step sequence of VCS #2 rounded down to zero when discretized for the SADA actuator and was removed from the command sequence. This discretization caused the impulse amplitudes to sum to slightly less than one. VCS #2 has the same target modes as VCS #1, but the natural frequencies of the target modes have been intentionally made erroneous for this case. Specifically, the frequencies of the zeros placed by the pole-zero cancellation algorithm have been made 10% higher than the poles of the modeled system. Having an inconsistent value for the modal natural frequencies between the input shaping algorithm and the physical system (represented by a finite element model in this research) explores the robustness of the pole-zero cancellation method. The system poles and VCS #2 shaper zeros are plotted in the *z*-plane in Figure 4.22 and this graph illustrates the large inaccuracies introduced by the 10% error in natural frequency.

TABLE 4.4: VIBRATION CONTROL SEQUENCE #2 DATA

Target Modes	#2	#3	#4	#7	#8	#11	#12	#40
Target Robustness	1	2	2	1	2	1	1	1
Total # Impulses	22							
Sampling Time, T	1.035 seconds							
Step Rate	200 PPS							

Impulse #	*Impulse Amplitudes*	*# Steps*	*Impulse Time, seconds*	*Step Time, seconds*
1	0.008644	4	0	0
2	0.016913	8	1.035	1.025
3	0.024012	12	2.07	2.05
4	0.048988	24	3.105	3.055
5	0.051361	26	4.14	4.085
6	0.052878	26	5.175	5.12
7	0.077811	39	6.21	6.1225
8	0.061522	31	7.245	7.1775
9	0.068918	34	8.28	8.205
10	0.094138	47	9.315	9.2075
11	0.071606	36	10.35	10.27
12	0.081233	41	11.385	11.2925
13	0.083637	42	12.42	12.325
14	0.052490	26	13.455	13.4
15	0.052883	26	14.49	14.435
16	0.044653	22	15.525	15.48
17	0.027901	14	16.56	16.535
18	0.028963	14	17.595	17.57
19	0.022739	11	18.63	18.6125
20	0.013575	7	19.665	19.6575
21	0.009587	5	20.7	20.6975
22	0.004635	2	21.735	21.74
Totals	0.999	500		

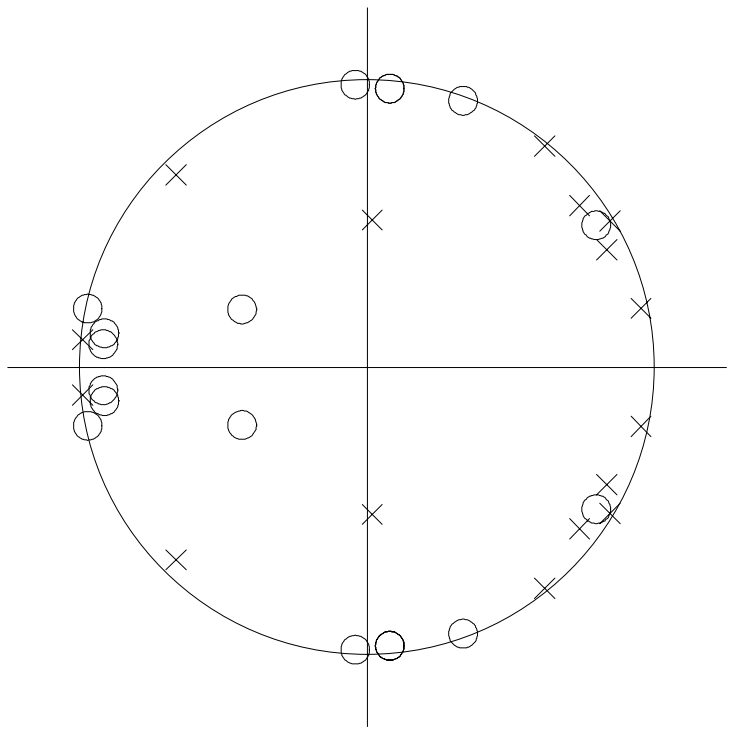

FIGURE 4.22: SYSTEM POLES AND VCS #2 ZEROS IN THE *Z*-PLANE (*T*=1.035 SECONDS)

The jitter analysis results of all four simulations for a 3.5-second jitter window are compared in Figures 2.23 through 4.26. Again, the *X*-rotation jitter results are plotted on a linear scale while the *Y*-rotation results are plotted on a semi-log scale, and a dashed line at the 100% level on all four plots indicates the jitter limit.

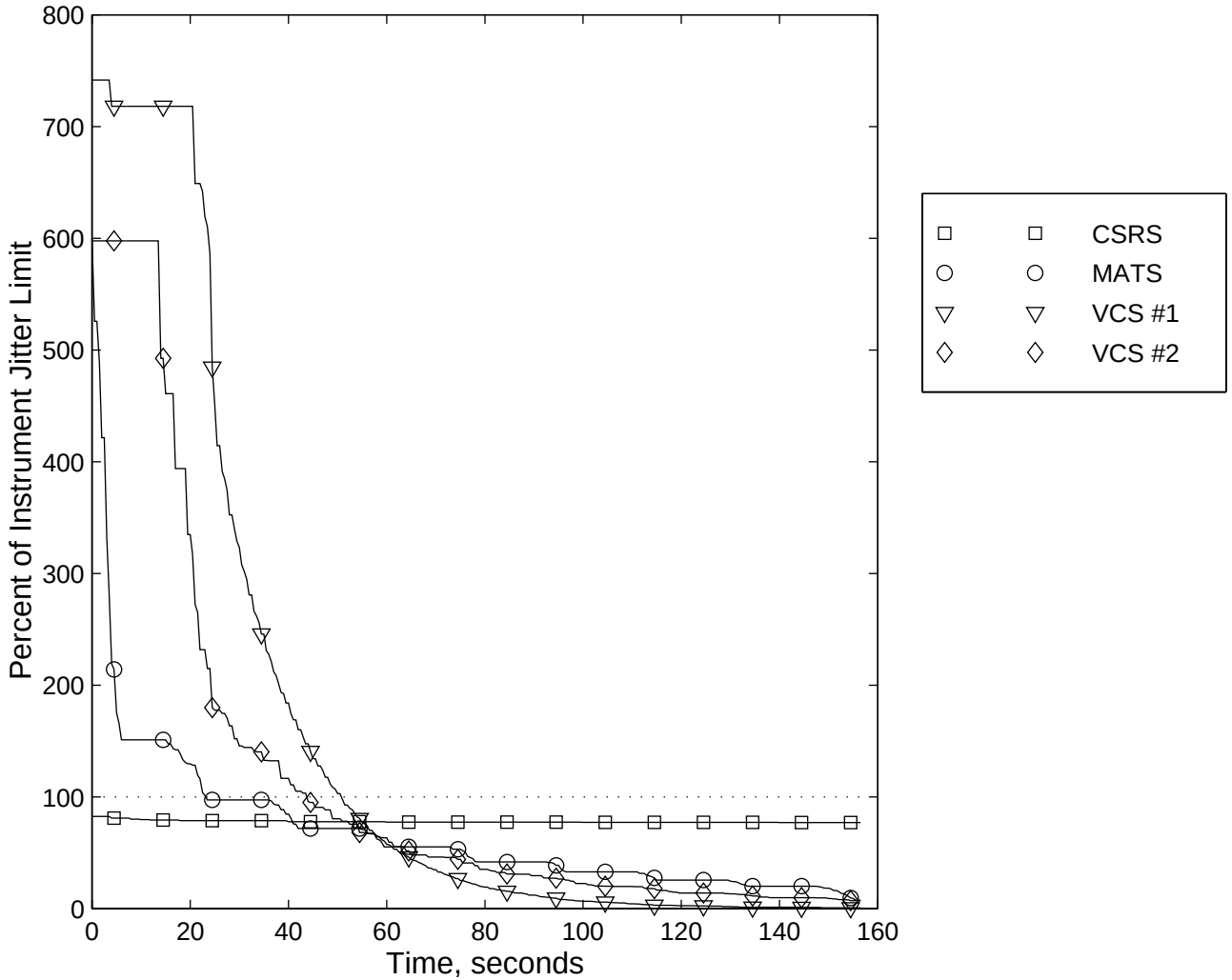

FIGURE 4.23: HSI *X*-ROTATION JITTER ANALYSIS RESULTS (3.5-SECOND WINDOW)

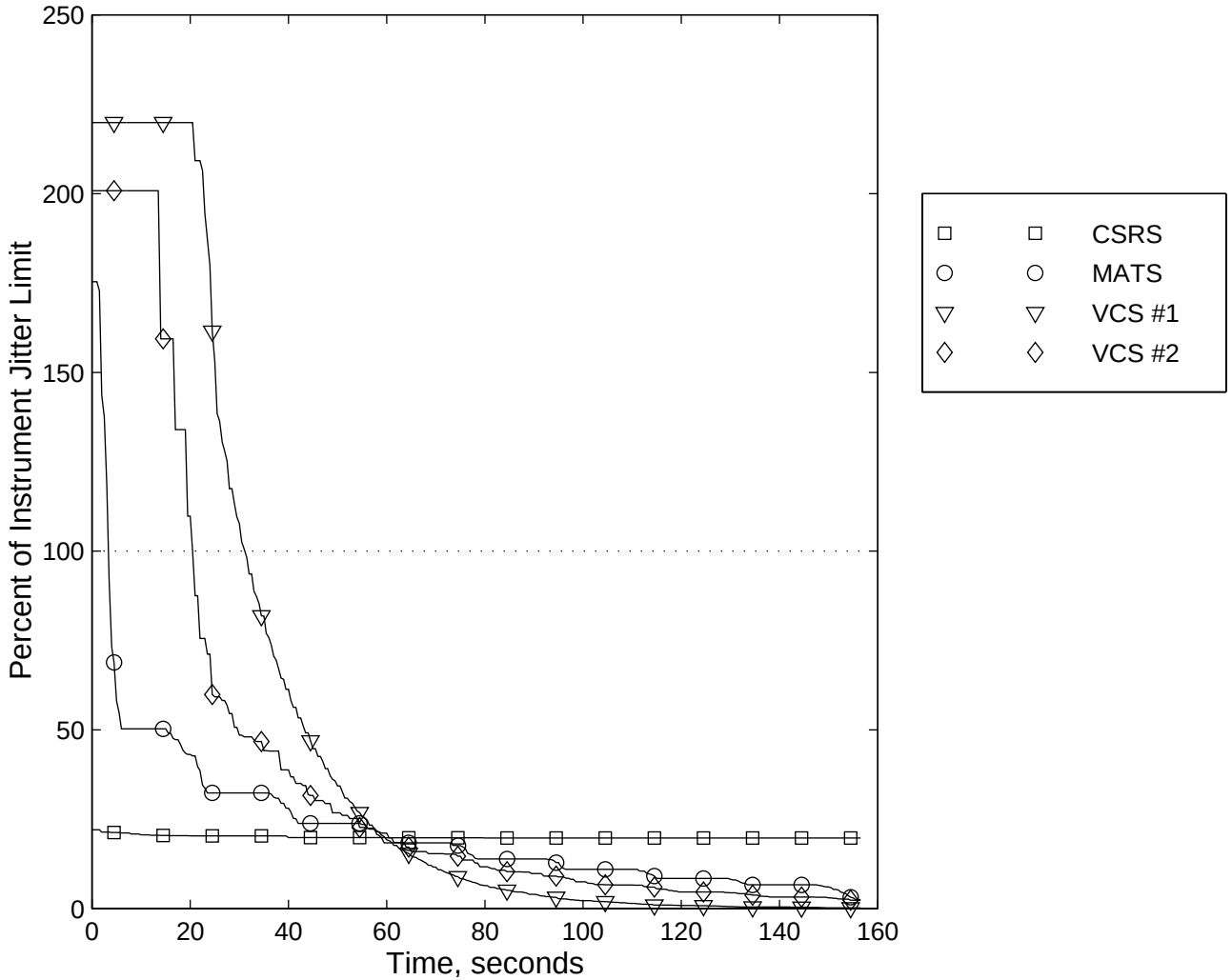

FIGURE 4.24: LEISA *X*-ROTATION JITTER ANALYSIS RESULTS (3.5-SECOND WINDOW)

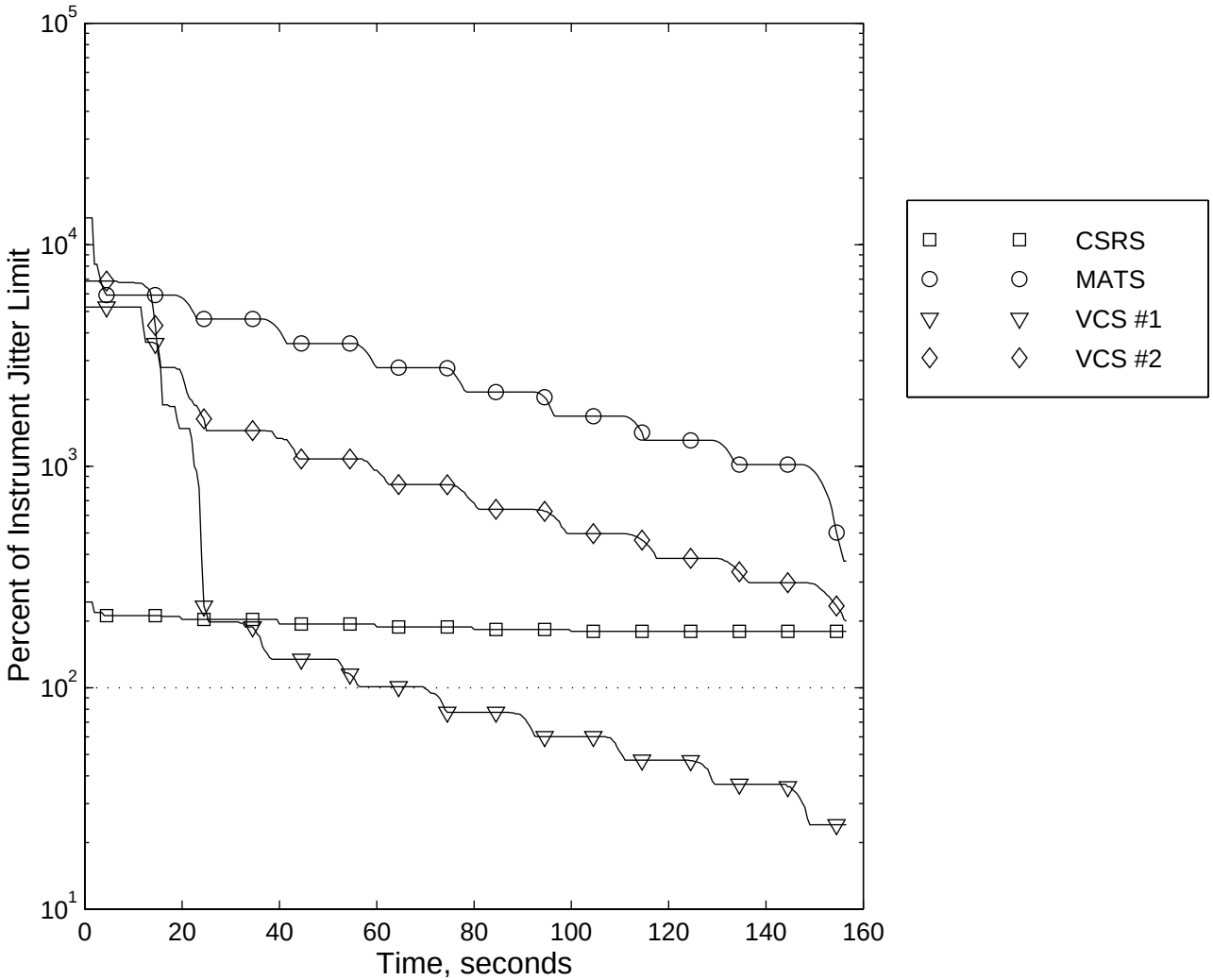

FIGURE 4.25: HSI *Y*-ROTATION JITTER ANALYSIS RESULTS (3.5-SECOND WINDOW)

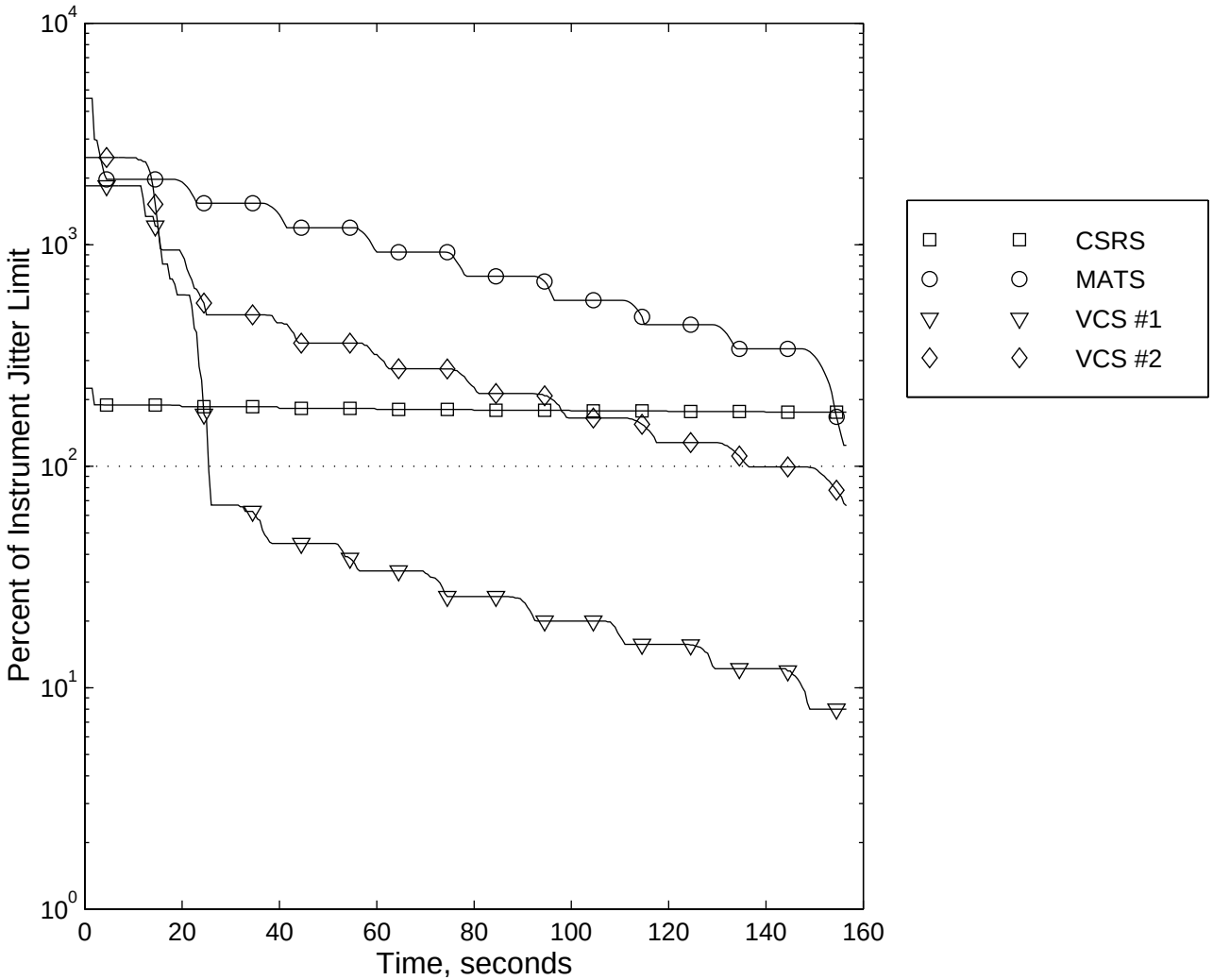

FIGURE 4.26: LEISA *Y*-ROTATION JITTER ANALYSIS RESULTS (3.5-SECOND WINDOW)

As might be expected, the vibration control performance for the *Y*-rotation of VCS #2 is less satisfactory than that of VCS #1. The 10% error in natural frequency for the target modes caused the 3.5-second window *Y*-Rotation jitter levels for VCS #2 (see Figures 4.25 and 4.26) to never achieve acceptable levels. Conversely, the *X*-rotation jitter results for VCS #2 are actually improved over the VCS #1 results. This is primarily due to the shorter time interval between the step sequences (T=1.14 seconds for VCS #1 and T=1.035 seconds for VCS #2) since the reduction in *X*-rotation jitter levels is caused by structural damping. In general, errors in identification of the natural frequencies or damping ratios of the target modes will cause less than ideal input shaper performance. To incorporate insensitivity to these possible errors, additional zeros can be placed on some or all of the target modes [15]. This technique is explored in the following section.

4.3.3 Vibration Control Sequence #3

It has been shown that the deleterious effects on vibration reduction caused by errors in either damping ratio or natural frequency can be mitigated by the placement of additional shaper zeros [15]. To illustrate this technique, the same target modes and erroneous natural frequencies used for VCS #2 were used for the final case, VCS #3, but three times as many zeros were placed. The 22 additional zeros for VCS #3 were located on the same points on the *z*-plane as the original 11 zeros for VCS #2, resulting in third order pole-zero cancellation.

Placing 33 input shaper zeros results in 67 impulse amplitudes but many impulse amplitudes rounded down to zero steps when discretized for the SADA actuator. Since these 21 null sequences occurred either before and after but not during the set of 46 non-

zero sequences, all the null sequences were ignored. The data describing this third vibration control sequence is given in Table 4.5. The total number of actuator steps was 500 but the sum of the impulse amplitudes is slightly less than one. If the discretization caused the total number of steps to be some value other than 500, the next SADA command sequence should then be performed at the appropriate time according to the solar tracking requirement, i.e., some time other than t=160 seconds.

4.4 Summary Of Results

The value of T and the total number of non-zero "impulses" are substantially different between the VCS #1 and VCS #3 command sequences, but these parameters combine to cause both to complete the solar array 10° rotation at similar times in the simulation (approximately T=25 seconds for VCS #1 and T=19.35 seconds for VCS #3). The command sequences consist of sets of actuator steps that vary from 1 to 57 steps for VCS #1 and from 1 to 23 steps for VCS #3. Therefore, these two command sequences are very comparable in the length of the actuation time and the SADA performance required which implies that in this application the "cost" of the additional robustness is negligible.

The complete set of graphs comparing the jitter analysis results for the CSRS, MATS, VCS #1, VCS #2, and VCS #3 simulations are given in Appendix C. Increasing the input shaper robustness allowed very similar vibration reduction performance to be achieved by VCS #3 in comparison to VCS #1, even though the VCS #3 target natural

TABLE 4.5: VIBRATION CONTROL SEQUENCE #3 DATA

Target Modes	#2	#3	#4	#7	#8	#11	#12	#40
Target Robustness	3	6	6	3	6	3	3	3
Total # Impulses	46							
Sampling Time, T	0.43 seconds							
Step Rate	200 PPS							

Impulse #	*Impulse Amplitudes*	*# Steps*	*Impulse Time, seconds*	*Step Time, seconds*
1	0.001188	1	0.00	0.0000
2	0.001784	1	0.43	0.4300
3	0.002598	1	0.86	0.8600
4	0.003612	2	1.29	1.2875
5	0.004805	2	1.72	1.7175
6	0.006211	3	2.15	2.1450
7	0.007927	4	2.58	2.5725
8	0.010022	5	3.01	3.0000
9	0.012460	6	3.44	3.4275
10	0.015108	8	3.87	3.8525
11	0.017854	9	4.30	4.2800
12	0.020717	10	4.73	4.7075
13	0.023798	12	5.16	5.1325
14	0.027116	14	5.59	5.5575
15	0.030493	15	6.02	5.9850
16	0.033650	17	6.45	6.4100
17	0.036421	18	6.88	6.8375
18	0.038864	19	7.31	7.2650
19	0.041113	21	7.74	7.6900
20	0.043152	22	8.17	8.1175
21	0.044744	22	8.60	8.5475
22	0.045628	23	9.03	8.9750
23	0.045750	23	9.46	9.4050
24	0.045296	23	9.89	9.8350
25	0.044482	22	10.32	10.2675
26	0.043333	22	10.75	10.6975
27	0.041693	21	11.18	11.1300
28	0.039446	20	11.61	11.5625
29	0.036697	18	12.04	11.9975
30	0.033718	17	12.47	12.4300
31	0.030727	15	12.90	12.8650
32	0.027753	14	13.33	13.2975
33	0.024711	12	13.76	13.7325
34	0.021586	11	14.19	14.1650
35	0.018504	9	14.62	14.6000
36	0.015648	8	15.05	15.0325
37	0.013114	7	15.48	15.4650
38	0.010871	5	15.91	15.9000
39	0.008847	4	16.34	16.3325
40	0.007019	4	16.77	16.7625
41	0.005432	3	17.20	17.1950
42	0.004132	2	17.63	17.6275
43	0.003108	2	18.06	18.0575
44	0.002302	1	18.49	18.4900
45	0.001655	1	18.92	18.9200
46	0.001139	1	19.35	19.3500
Totals	0.996228	500		

frequencies were 10% higher than the modeled system. For several windows the jitter decreased below the jitter limit at an earlier time for VCS #3 than for VCS #1, primarily due to the earlier completion of the solar array rotation by VCS #3. These results indicate that in this application, an increase in the number of shaper zeros can improve the feedforward robustness of the system with very little or no decrease in other aspects of system performance.

For rotation about the *X*-axis, the VCS simulations in general have less time with acceptable jitter levels than either the CSRS or MATS simulations. These results are presented in Figures C.1 through C.12. One notable exception is the 3.5 second window analysis of the CSRS simulation for the HSI instrument shown in Figure C.11.

Figures C.13 through C.24 show the marked improvement for rotation about the *Y*-axis in the VCS #1 and #3 simulations in comparison to the CSRS and MATS baseline cases. The CSRS and MATS simulations have limited to zero time during the simulation when acceptable jitter levels were achieved. The system identification error explored in the VCS #2 simulation shows up as significantly worse mission performance but the use of additional shaper zeros counteracts this deficiency very well. These results show that the VCS step commands are an effective means to control structural vibrations and therefore improve mission performance when the system identification is reasonably accurate and robustness techniques are employed.

5 Conclusions

The structural vibration response of a well-understood system can be reduced considerably through the use of input shaping techniques. Reduction of structural vibration can often allow the system to perform required tasks more quickly, using less actuator power, reducing system wear, and possibly allowing the addition of new tasks that were not possible before.

5.1 Current Results

As is the case for many techniques in structural dynamics, the vibration reduction performance of pole-zero cancellation methods is dependent on the accuracy of the system identification. In the Lewis spacecraft vibration problem, the system identification for VCS #1 was perfect insofar as the results presented were generated through the use of a simulation that used the same system description as that used to generate the input shaper. Therefore the results could be viewed as exceptional in comparison to the results that would be obtained in practice with a poorly understood physical system. This is a known limitation of the pole-zero cancellation approach.

However, identifying a physical system through empirical techniques is becoming common and can yield accurate descriptions of complex systems relatively quickly. The results presented here and through experimentation [15] have shown that the robustness of an input shaper transfer function can be increased through the placement of additional zeros as discussed in this paper. In the current research, it was found that this increase in

controller robustness could be accomplished without any increase in computational complexity or actuator requirements.

5.2 Recommendations for Future Research

Several areas were recognized as topics that warrant additional investigation and are presented briefly below. The use of alternative actuators is a basic consideration, as is a deeper understanding of the effects of changing system parameters to multiple mode robustness. Beyond those topics, adaptation of the input shaper (perhaps automatically) to changes in the system should be considered. This is particularly appropriate as digital computing power increases in capability and much more involved control schemes can be implemented.

5.2.1 Further Study of Actuator Dynamics

A stepper motor actuator was simulated as the system input device for the shaped commands. This is not the most desirable actuator for the pole-zero cancellation technique implemented, but it was shown that the technique is still very effective with this actuator. Use of alternative stepping methods to a constant step rate and other actuator techniques specific to stepper motors might allow further improvement on the results obtained.

5.2.2 Further Study of Multiple-Mode Robustness

A more extensive study of the relationship between the structural modes, system identification accuracy, controller robustness, and input shaper performance could be useful since the effective use of the robustness afforded by additional shaper zeros depends upon the application. In the case of a rotating solar array presented here, the system modal

parameters would change as the orientation of the solar arrays relative to the spacecraft bus progressed.

Extending the input shaper algorithm to account for the current relative orientation (and therefore the *expected* change in system parameters) before calculating the command sequence would be one method of handling this variation in system parameters. A simpler method might be to “frame” the range of possible values of natural frequency and damping ratio for the target modes with multiple zeros. This second technique could produce acceptable system performance with a single command sequence for all relative orientations, or both techniques could be combined to produce a limited number of command sequences to cover the range of possible system parameters.

5.2.3 Automatic Selection of Target Modes

Study of the effectiveness of the frequency response function or other methods in identifying the modes of concern in the presence of the many variables could also be topics for further research. There are, in general, many feasible input shaper transfer functions for a particular application and a study of a method to automate the selection of the most desirable input shaping solution would be a first step to an adaptive extension of pole-zero cancellation.

5.2.4 Extension to Adaptive Feedforward Vibration Control

The pole-zero cancellation method presented in this paper is computationally simple to implement and could be incorporated into an on-board computing system or embedded controller. With the addition of feedback, the on-board computer could be programmed to automatically adapt the input shaper to any variations in the system parameters or

environment, or changes to the mission requirements, whether these variations were expected or not. This would be an extension of existing research into input shaping for varying system parameters [1]. Better performance of mechanical systems can be obtained with fewer feedback components through the use of a feedforward input shaping algorithm [12]. The entirely software-based simulation and jitter analysis tools presented in this research would facilitate rapid experimentation with proposed adaptive feedforward algorithms and allow researchers to pursue the most promising methods.

References

[1] Book, W.J. and Magee, D.P., “Application of Input Shaping to a System with Varying Parameters”, *Proceedings of the 1992 Japan-USA Symposium on Flexible Automation*, San Francisco, CA, July 1992, pp. 519-526

[2] Bouton, C.E. and McConnell, K.G., “Noise and Vibration Control with Robust Vibration Suppression”, *Sound and Vibration*, June 1997, pp. 24-26

[3] Farley, R., "Modeling of a Rotational Stepper Motor with a Flexible Load", *Proceedings of the 29th Aerospace Mechanisms Symposium*, NASA Conference Publication #3293, League City, TX, May 1995, pp. 280-282

[4] Giesy, D.P., Kenny, S. and Maghami, P., "PLATSIM: A Simulation and Analysis Package for Large-Order Flexible Systems (Version 2.0)," NASA TM-4790, 1997

[5] Giesy, D.P., "Efficient Calculation of Jitter/Stability Metric," *Journal of Spacecraft and Rockets*, Vol. 34, No. 4, July-August 1997, pp. 549-557

[6] Hyde, J.M. and Seering, W.P., “Using Input Command Pre-Shaping to Suppress Multiple Mode Vibration”, *Proceedings of the 1991 IEEE International Conference on Robotics and Automation*, Sacramento, CA, April 1991, pp. 2604-2609

[7] Murphy, B.R. and Watanabe, I., “Digital Shaping Filters for Reducing Machine Vibration”, *IEEE Transactions on Robotics and Automation*, April 1992, Vol. 8, No. 2, pp. 285-289

[8] Rappole, B.W., Singer, N.C., and Seering, W.P., “Input Shaping with Negative Sequences for Reducing Vibrations in Flexible Structures”, *Proceedings of the 1993 American Control Conference*, San Francisco, CA, June 1993, Vol. 3, pp. 2695-2699

[9] Rappole, B.W., Singer, N.C., and Seering, W.P., "Multiple-Mode Input Shaping Sequences for Reducing Residual Vibrations", *Machine Elements and Machine Dynamics (ASME)*, 1994, Vol. 71, pp. 11-16

[10] Singer, N.C. and Seering, W.P., "Preshaping Command Inputs to Reduce System Vibration", *ASME Journal of Dynamic Systems, Measurements, and Control*, March 1990, Vol. 112, pp. 76-81

[11] Singer, N.C., "Residual Vibration Reduction in Computer Controlled Machines", Ph.D. Dissertation, Massachusetts Institute of Technology, February 1989

[12] Singh, T. and Vadali, S.R., "Robust Time-Delay Control", *ASME Journal of Dynamic Systems, Measurement, and Control*, 1993, Vol. 115, pp. 303-306

[13] *Small Satellite Technology Initiative: Lewis Spacecraft Program, System Critical Design Audit*, NASA and TRW, January 1995

[14] Smith, O.J.M., Feedback Control Systems, 1958, New York, McGraw-Hill Book Company, Inc., pp. 331-345

[15] Tuttle, T.D. and Seering, W.P., "A Zero-Placement Technique for Designing Shaped Inputs to Suppress Multiple-Mode Vibration", *Proceedings of the 1994 American Control Conference*, Baltimore, MD, June 1994, Vol. 3, pp. 2533-2537

Appendix A: Stepper Motor Description

The basic operation of a three-phase stepper motor is presented in this section. The relationship between the rotor position and the motor output torque is shown, and the specific motor parameters for the SADA actuator on Lewis are calculated.

A.1 Torque Function

Referring to the stepper motor parameters of Table 2.2, the stepper motor torque function is

$$T_{motor} = T_{powered} \cos\left[C_e\left(\theta_e + n\frac{\pi}{3}\right)\right] + T_{detent} \sin\left[C_m \theta_e\right] \qquad \textbf{(A.1}$$

where $T_{powered}$ and T_{detent} are the maximum torques the electromagnets and permanent magnets of the motor can respectively develop on the rotor, θ_e is the current rotor electrical angle (from 0 to 2π radians), C_m and C_e are constant motor parameters, and n is the state count. The three-phase stepper motors manufactured by Schaeffer Magnetics have a total of 6 different electrical states. Therefore n is an integer value that repeats from 1 to 6, forming one *electrical cycle* of the motor. One electrical cycle can be thought of as a rotation through 360 *electrical degrees* denoted as 360_e° from here on. C_m is a motor constant equal to the number of mechanical steps per revolution of the motor rotor

$$C_m = \frac{N_{rev}}{R} = \frac{18{,}000}{100} = 180 \qquad \textbf{(A.2}$$

where N_{rev} is the total number of steps per revolution of the output shaft and R is the gear reduction of the motor harmonic drive. C_e is a second motor constant that defines the number of electrical cycles per revolution of the motor rotor

$$C_e = \frac{C_m}{n_{\max}} = \frac{180}{6} = 30 \qquad \textbf{(A.3}$$

where n_{max} equals 6 and is the total number of different states in one electrical cycle. The rotor electrical angle, θ_e , is related to the rotor mechanical angle, θ_m ,by

$$\frac{\theta_m}{\Delta\theta_m} = \frac{\theta_e}{360_e^{\circ} / n_{\max}} \qquad \textbf{(A.4}$$

where $\Delta\theta_m$ equals 2° and is the incremental change in the rotor mechanical angle caused by progression through one electrical state. Substituting in specific motor values results in

$$\theta_e = 30\,\theta_m \qquad \textbf{(A.5}$$

In summary, one complete electrical cycle of the stepper motor consists of progressive motion through 6 electrical states (i.e., rotation through 360_e°) that results in a 12° rotation of the motor rotor. With a 100:1 gear reduction through the harmonic drive, a corresponding 0.12° rotation of the output shaft will occur.

A.2 Detent and Powered Motor Torques

The torque developed on the rotor at any time depends on which, if any, motor electrical state is powered, the position or phase of the rotor relative to the motor windings, and the maximum amplitude of the powered and detent holding torques. Figure A.1 shows the torques on the rotor for a complete electrical cycle, if only state #1 is

powered. The two torques are the detent or unpowered torque, produced by permanent magnets and the state 1 torque, produced by the state 1 electromagnets.

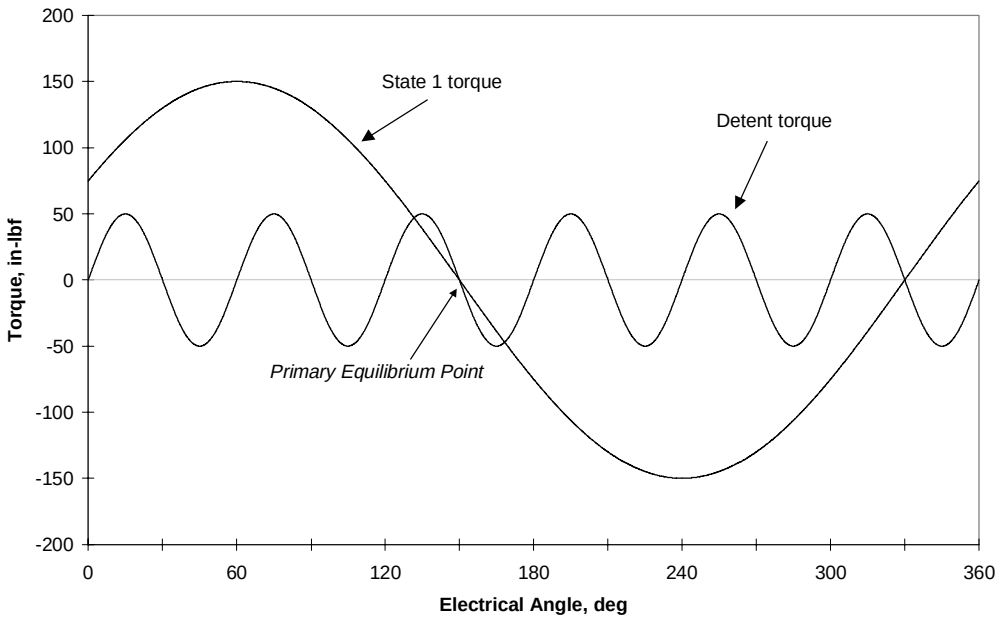

FIGURE A.1: DETENT AND STATE #1 TORQUES VS. ROTOR ELECTRICAL ANGLE

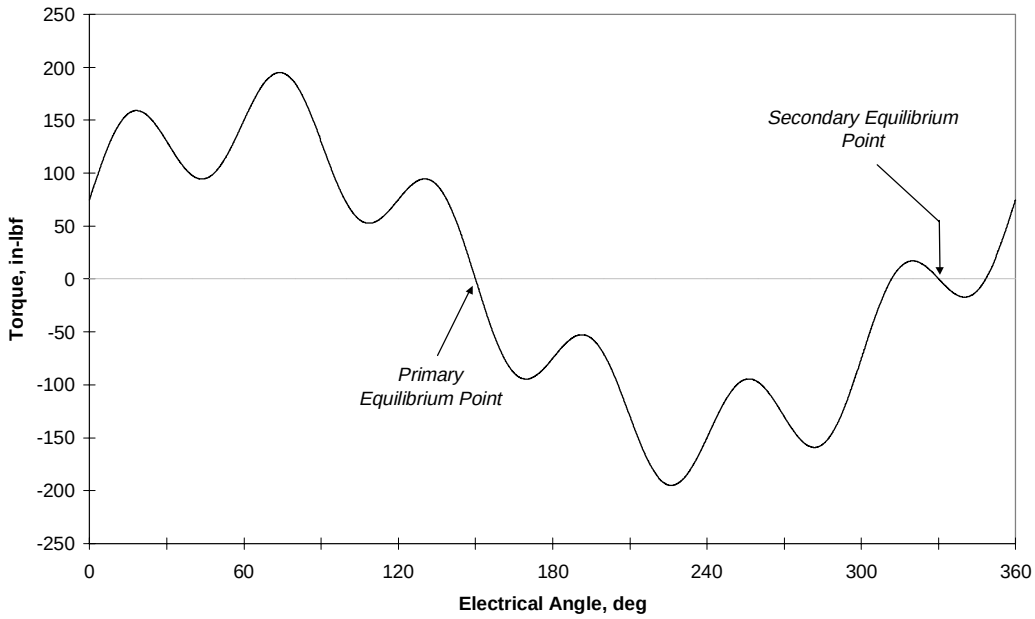

FIGURE A.2: COMPOSITE TORQUE VS. ROTOR ELECTRICAL ANGLE

Figure A.2 shows the composite torque of these two sources. For nearly 180^{o}_{e} in both directions from the equilibrium point, the composite torque of the detent permanent magnets and the state 1 electromagnets are restoring forces to the equilibrium point at 150^{o}_{e}. Note that there is a narrow secondary equilibrium region centered at 330^{o}_{e}. The width of this secondary equilibrium region is dependent on the motor parameters, and is defined by the solution to the transcendental relation

$$\frac{-T_{powered}}{T_{detent}} = \frac{\sin\left[C_m \bar{\theta}_e\right]}{\cos\left[C_e \bar{\theta}_e\right]} \qquad \textbf{(A.6}$$

For the motor configuration of interest the two solutions to Equation 5.6 between 0^{o}_{e} and 360^{o}_{e} are

$$-3 = \frac{\sin\left[180\bar{\theta}_e\right]}{\cos\left[30\bar{\theta}_e\right]}$$

$$\therefore \bar{\theta}_e \approx \begin{Bmatrix} 311.7^{\circ}_{e} \\ 348.3^{\circ}_{e} \end{Bmatrix} \qquad \textbf{(A.7}$$

Therefore, for approximately 161.7°_{e} on either side of the desired equilibrium point, the composite motor torque will be a restoring force. If the load inertia were to cause the rotor to fall out of phase with the equilibrium point by up to 161.7°_{e} in either direction, it will eventually settle to the correct position. This statement assumes that the same electrical state is maintained during this settling time and for this reason the Schaeffer Motor Driver incorporates a "Last Pulse Detector" which ensures that the last of a series of pulses stays on for as long as 100 milliseconds [private communication]. The rotor could fall out of phase with the equilibrium position by up to 5.39° (using Equation A.5 to convert electrical to mechanical degrees) and still recover to the correct location.

A.3 Stepping Operation of a Three Phase Motor

During operation in a single direction, the stepper motor drive electronics power the six electrical states consecutively. For clarity, the powered torques from only the first three states are shown in Figure A.3. The rotor will stabilize at each of the equilibrium points (marked as 1,2, and 3) corresponding to the current state. Once the rotor has achieved the desired rotation, the electrical power can be removed from the motor windings and the permanent magnet detent torque can be used to maintain the rotor position.

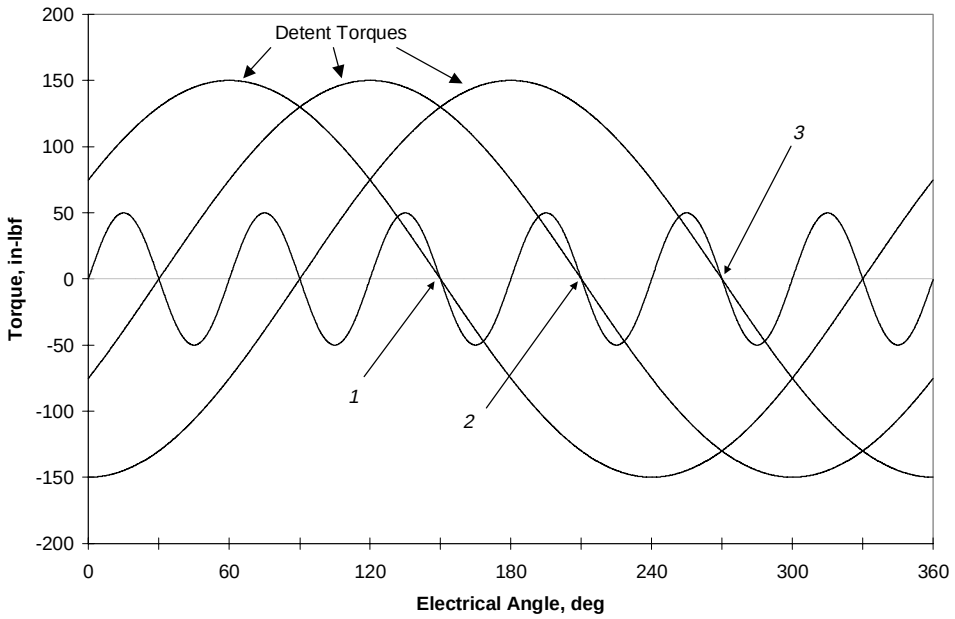

FIGURE A.3: DETENT, STATES #1, #2, AND #3 TORQUES VS. ROTOR ELECTRICAL ANGLE

The detent torque does not require electrical power but is generally much less than the composite torque and sufficiently large disturbances will cause the rotor to slip to a different equilibrium position. However, powering the electrical state again would cause the rotor to achieve its previous position, if the rotor position was within the range specified by Equation A.6. Stepper motors are inherently underdamped, and therefore the choice of actuator should take into consideration the expected overshoot. This overshoot must be examined to see that it is acceptable from a system performance standpoint and also that it does not cause the rotor to slip and come to rest at a different equilibrium point than the one desired.

A.4 Motor-Load Dynamics

Using the simple rigid body physical model developed in Section 3, standard gear reduction principles yield the moment of inertia of the solar array wing reflected through the harmonic drive to the rotor as

$$I_{yy}^{SA} @ Rotor = \frac{I_{yy}^{SA}}{R^2} \approx 6.17 \times 10^{-5} \text{ lbf} - \text{in} - \text{s}^2 \qquad \textbf{(A.8}$$

The reflected load inertia is only slightly less than the rotor inertia ($I_R \approx 8.3\text{x}10^{-5}$ lbf-in-s^2) and warrants the more sophisticated modeling of the coupled stepper motor and output shaft load dynamics in Section 3.2.3.

Appendix B: Modal Frequencies of Lewis Finite Element Model

Mode Number	Modal Frequency (Hz)
1	0.297901
2	0.468151
3	1.049531
4	1.103733
5	1.677571
6	1.725550
7	1.964968
8	4.469271
9	4.973269
10	5.034933
11	5.697196
12	5.727159
13	9.514330
14	9.589122
15	11.74925
16	11.78386
17	17.06151
18	17.26538
19	19.09605
20	19.15505
21	19.39336
22	19.75395
23	23.86783
24	24.15030
25	26.43960
26	26.48198
27	31.22197
28	31.41235
29	34.52868
30	34.89009
31	40.85143
32	40.86887
33	41.36383
34	41.64475
35	42.52631
36	47.98235
37	48.58402
38	48.80582
39	49.72838
40	51.44397
41	51.74523
42	52.57273
43	53.08799
44	53.19312

Mode Number	Modal Frequency (Hz)
45	54.54561
46	54.55496
47	57.89866
48	58.39659
49	60.71121
50	61.17287
51	64.19898
52	64.71624
53	65.18632
54	66.00910
55	66.10107
56	66.20857
57	66.33535
58	66.44436
59	69.45025
60	69.60864
61	70.59897
62	71.48188
63	73.39683
64	74.33906
65	74.87919
66	75.31638
67	75.99451
68	76.83908
69	76.94752
70	79.79381
71	79.94364
72	81.61653
73	82.43846
74	82.58076
75	83.16011
76	84.21708
77	85.10975
78	85.45368
79	85.51268
80	87.14651
81	87.25028
82	87.68699
83	89.00592
84	89.44977
85	89.47207
86	89.66619
87	89.96201
88	90.85836
89	91.08218

Mode Number	Modal Frequency (Hz)
90	91.27055
91	91.42578
92	92.12127
93	92.74441
94	92.93291
95	94.17017
96	94.56207
97	95.17544
98	95.88823
99	97.16349
100	98.18956
101	98.31394
102	98.41007
103	98.78435
104	99.69010
105	101.8710
106	102.3199
107	102.4502
108	104.5725
109	106.0651
110	106.3290
111	107.3103
112	107.6709
113	108.1076
114	108.1819
115	109.7548
116	110.1198
117	113.3281
118	114.6113
119	114.9526
120	115.4971
121	116.0151
122	116.9398
123	117.1381
124	119.3052
125	119.3512

Mode Number	Modal Frequency (Hz)
126	119.4839
127	120.8883
128	121.5600
129	121.8896
130	122.0094
131	122.6839
132	123.0976
133	124.0886
134	125.1805
135	125.4099
136	126.0566
137	127.9412
138	129.4753
139	129.9970
140	130.5938
141	130.6799
142	130.8793
143	131.6988
144	132.3342
145	134.0331
146	134.5332
147	134.7790
148	135.3067
149	135.7669
150	135.9420
151	136.2022
152	137.5837
153	137.8179
154	138.9227
155	139.1206
156	139.6903
157	140.6596
158	140.8990
159	142.4252
160	144.1907
161	146.4973
162	149.1704
163	149.5050

Appendix C: Comparison Of Jitter Analysis Results

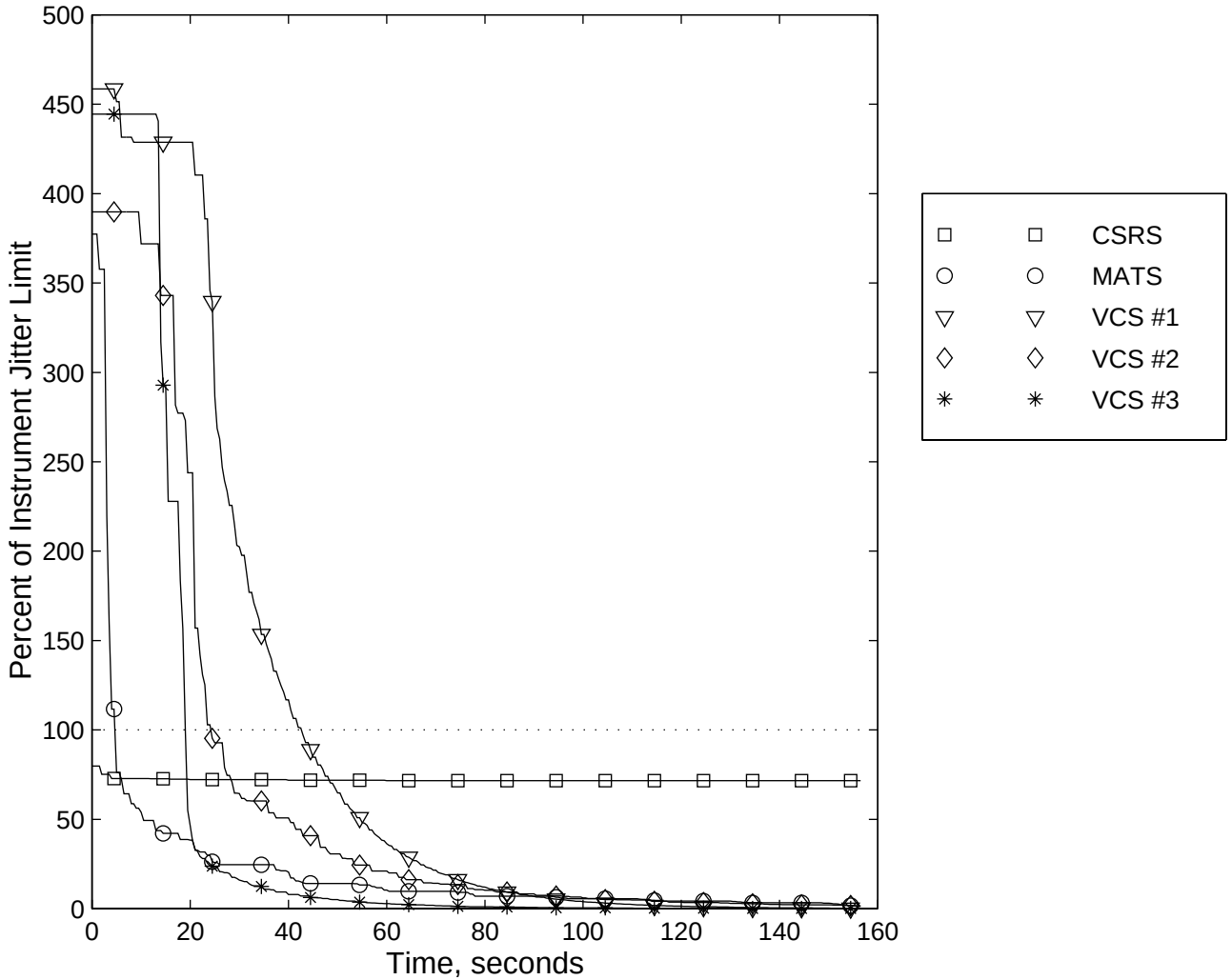

FIGURE C.1: HSI *X*-ROTATION JITTER LEVELS (0.05 SECOND WINDOW)

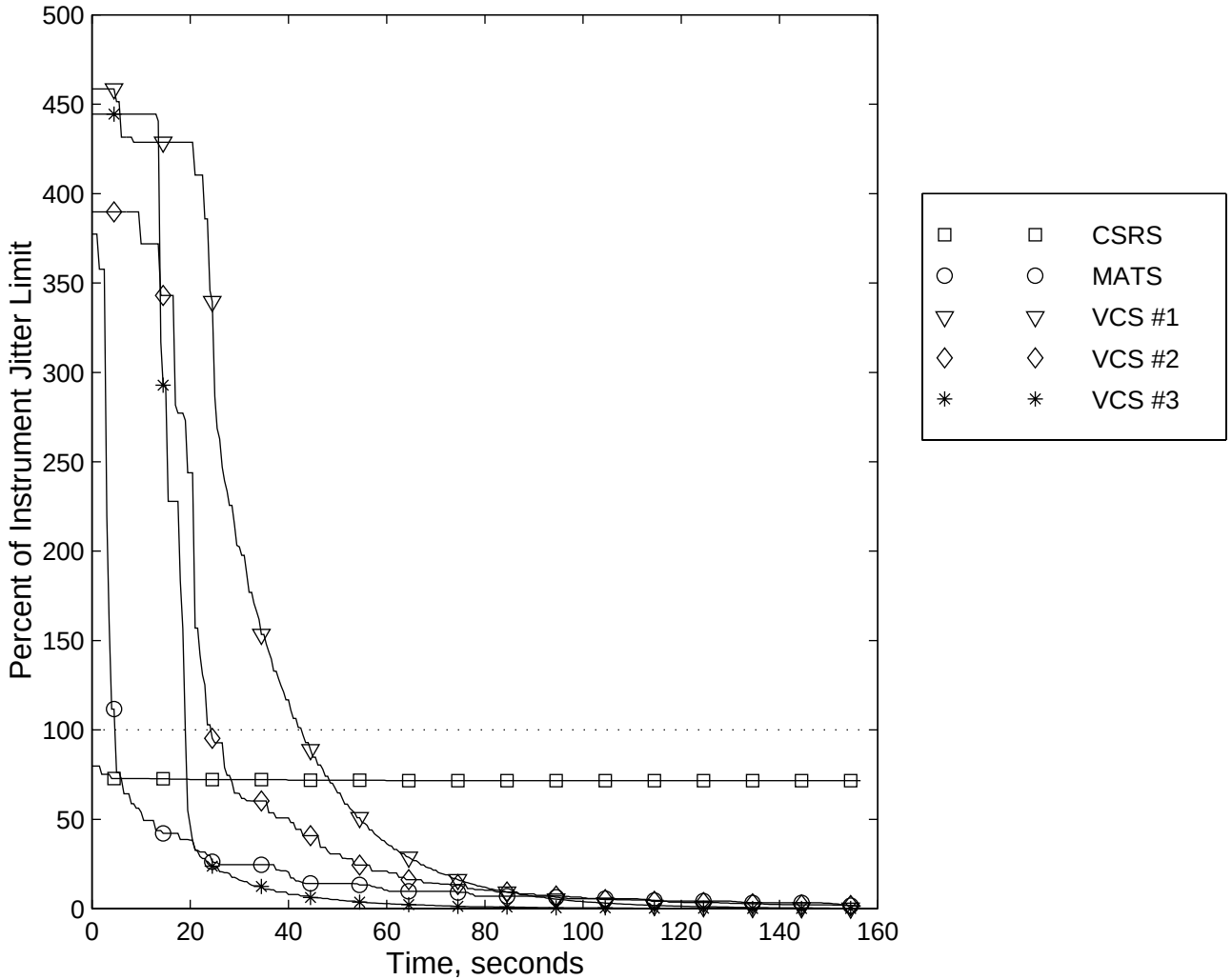

FIGURE C.2: LEISA *X*-ROTATION JITTER LEVELS (0.05 SECOND WINDOW)

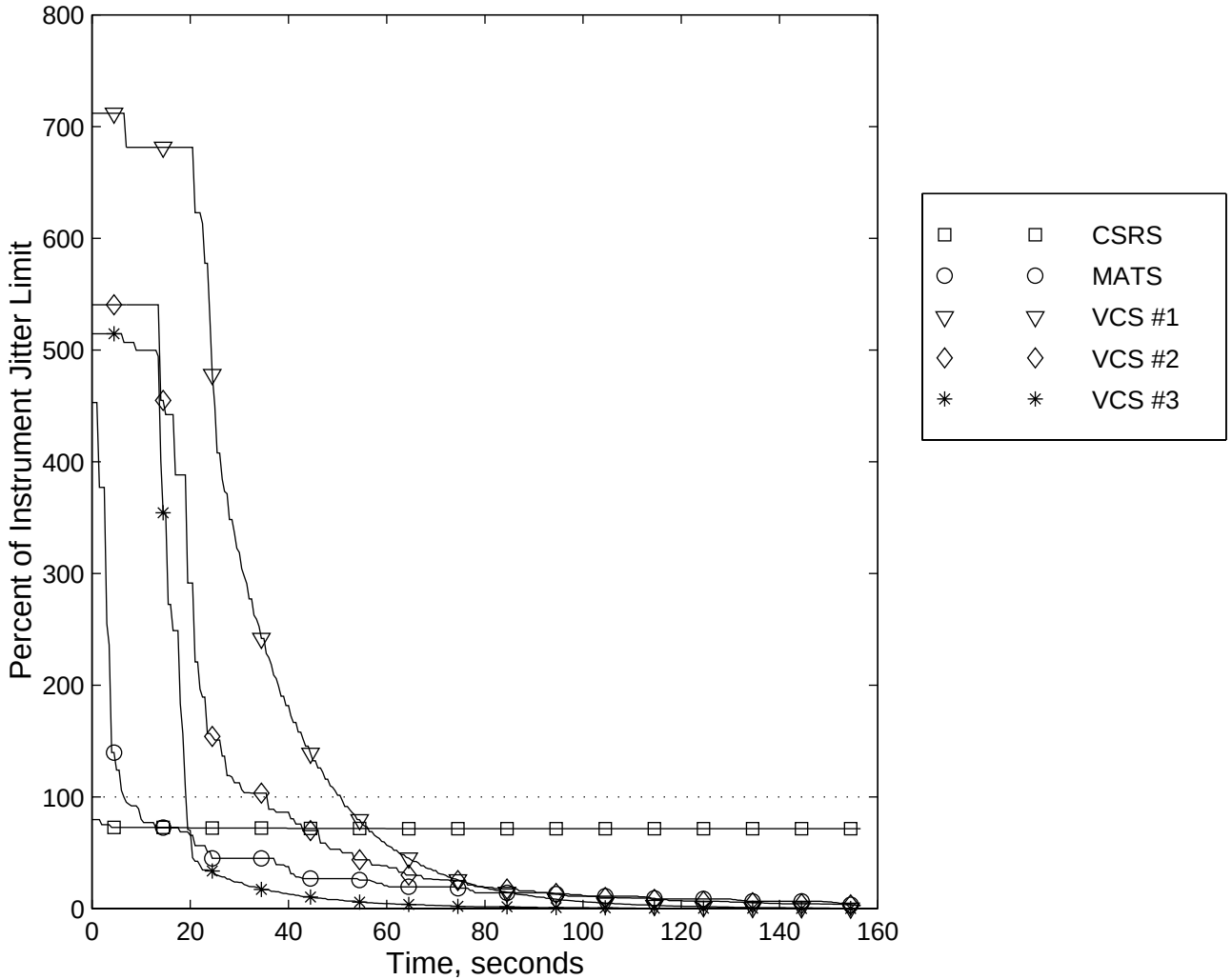

FIGURE C.3: HSI *X*-ROTATION JITTER LEVELS (0.1 SECOND WINDOW)

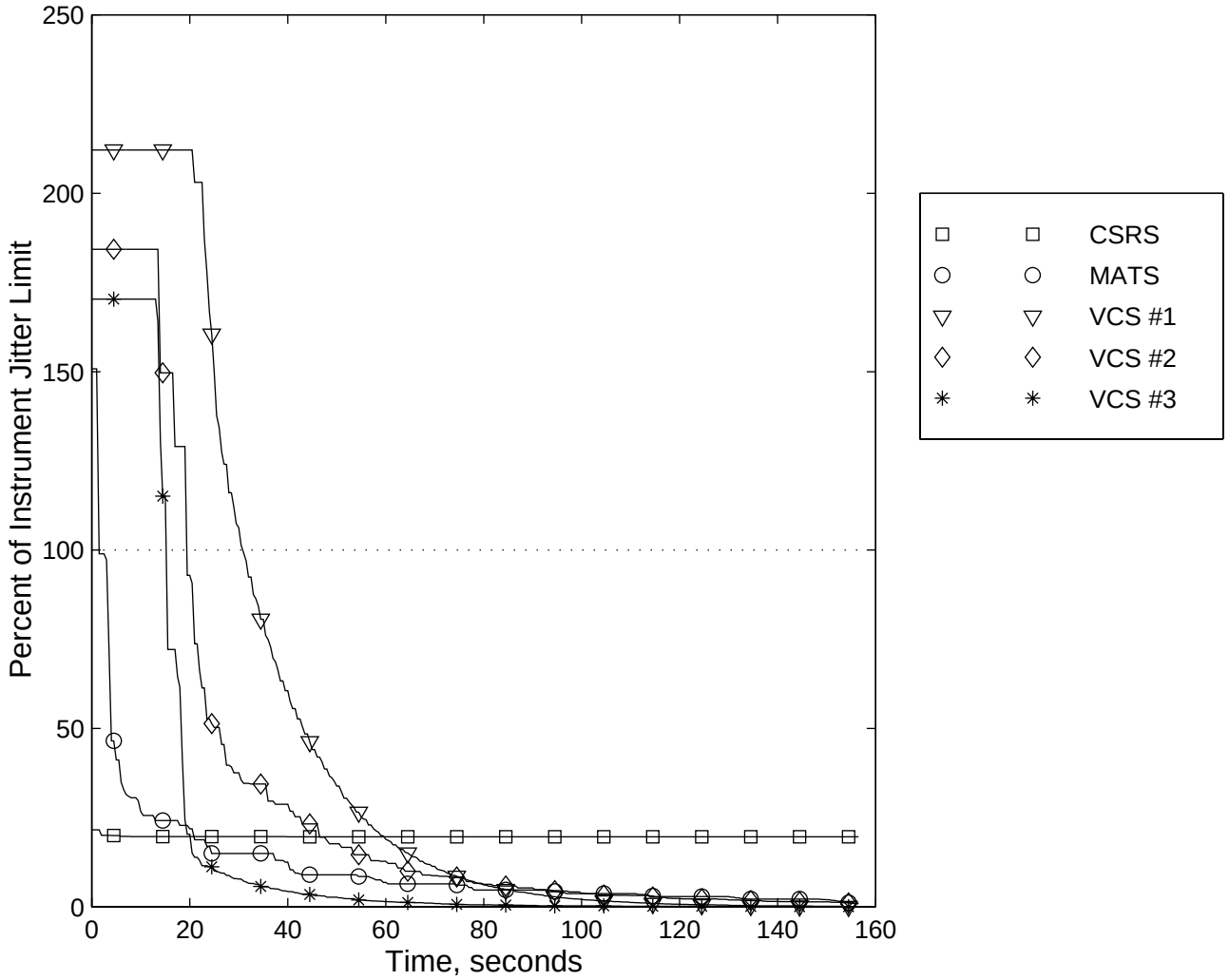

FIGURE C.4: LEISA *X*-ROTATION JITTER LEVELS (0.1 SECOND WINDOW)

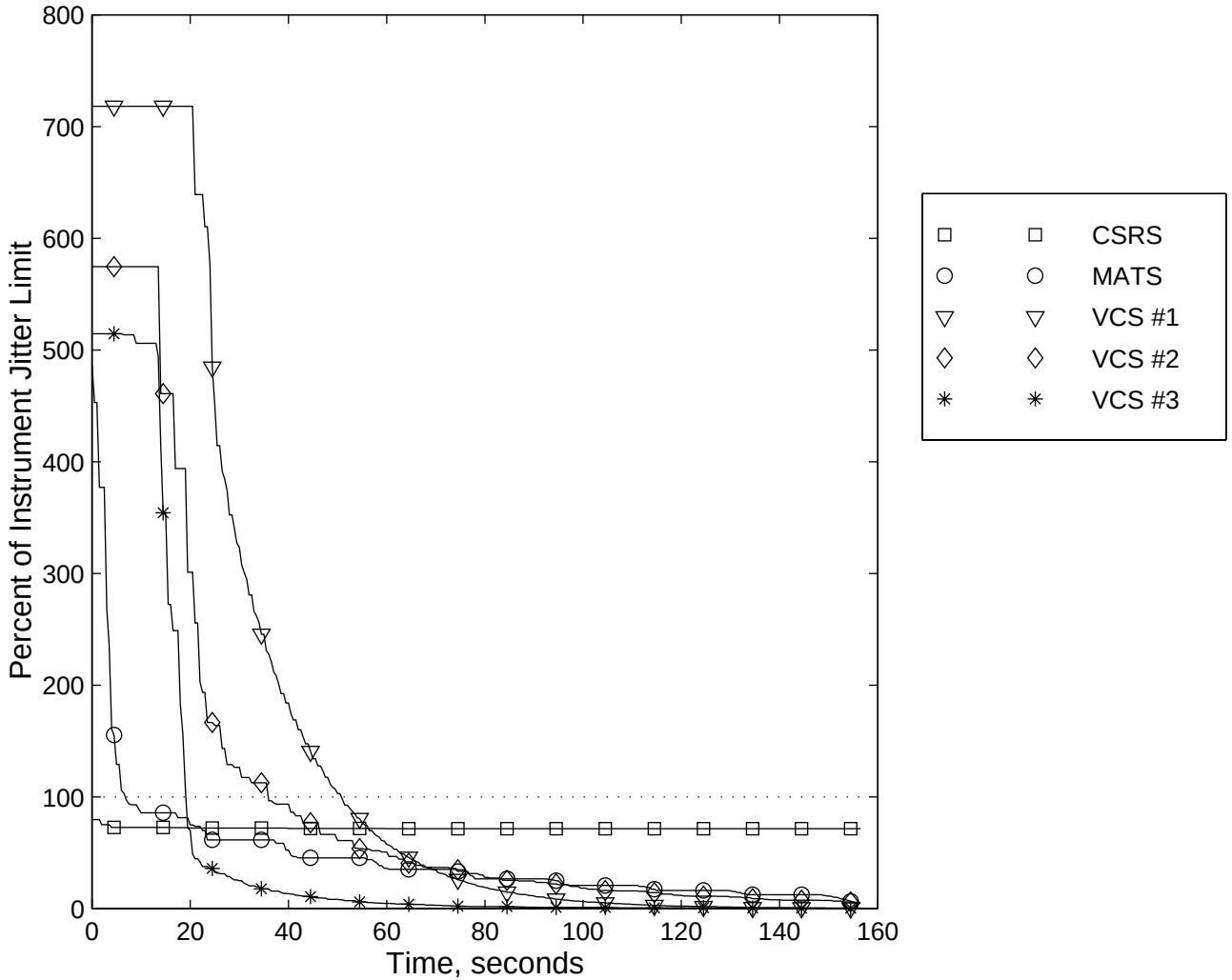

FIGURE C.5: HSI *X*-ROTATION JITTER LEVELS (0.2 SECOND WINDOW)

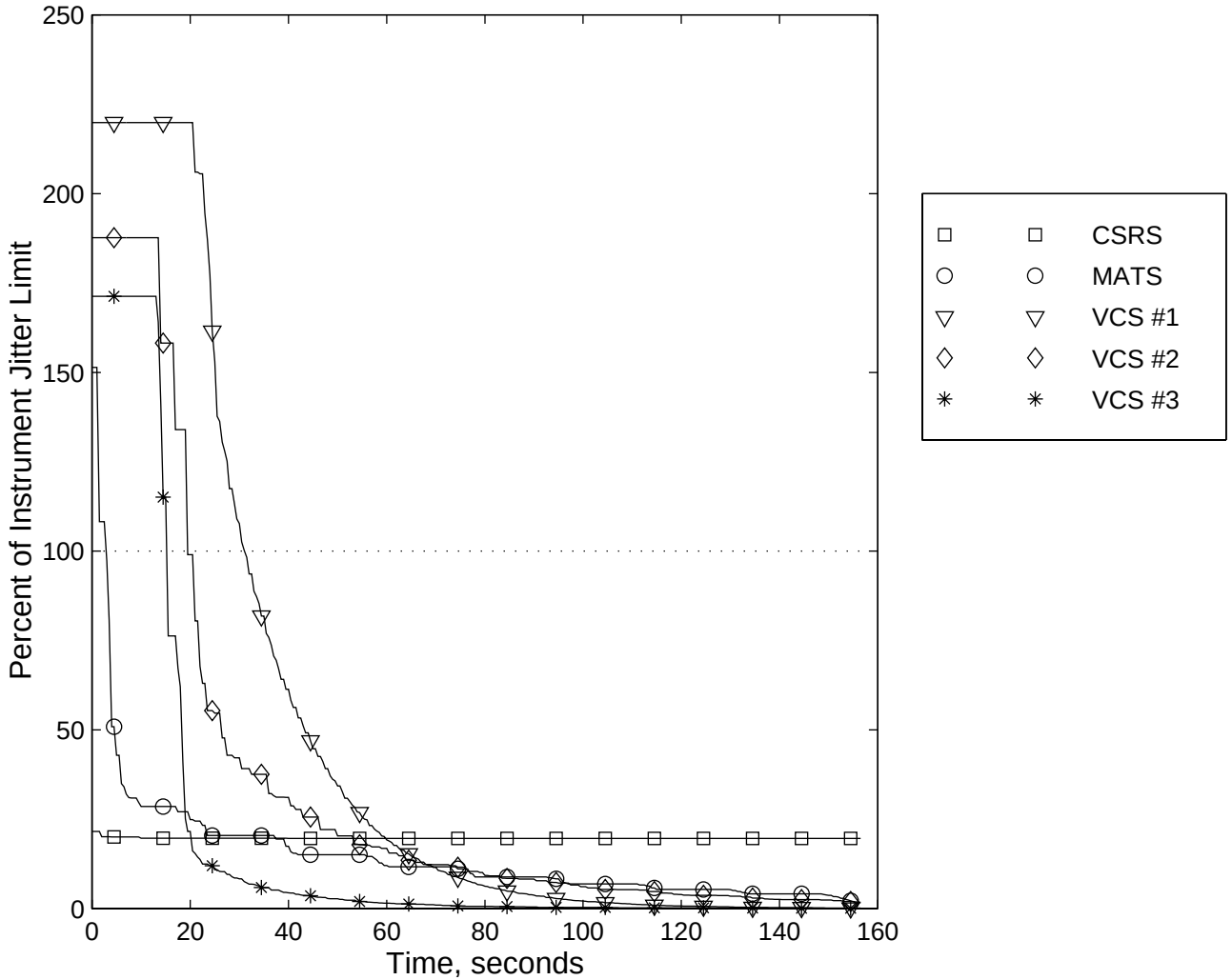

FIGURE C.6: LEISA *X*-ROTATION JITTER LEVELS (0.2 SECOND WINDOW)

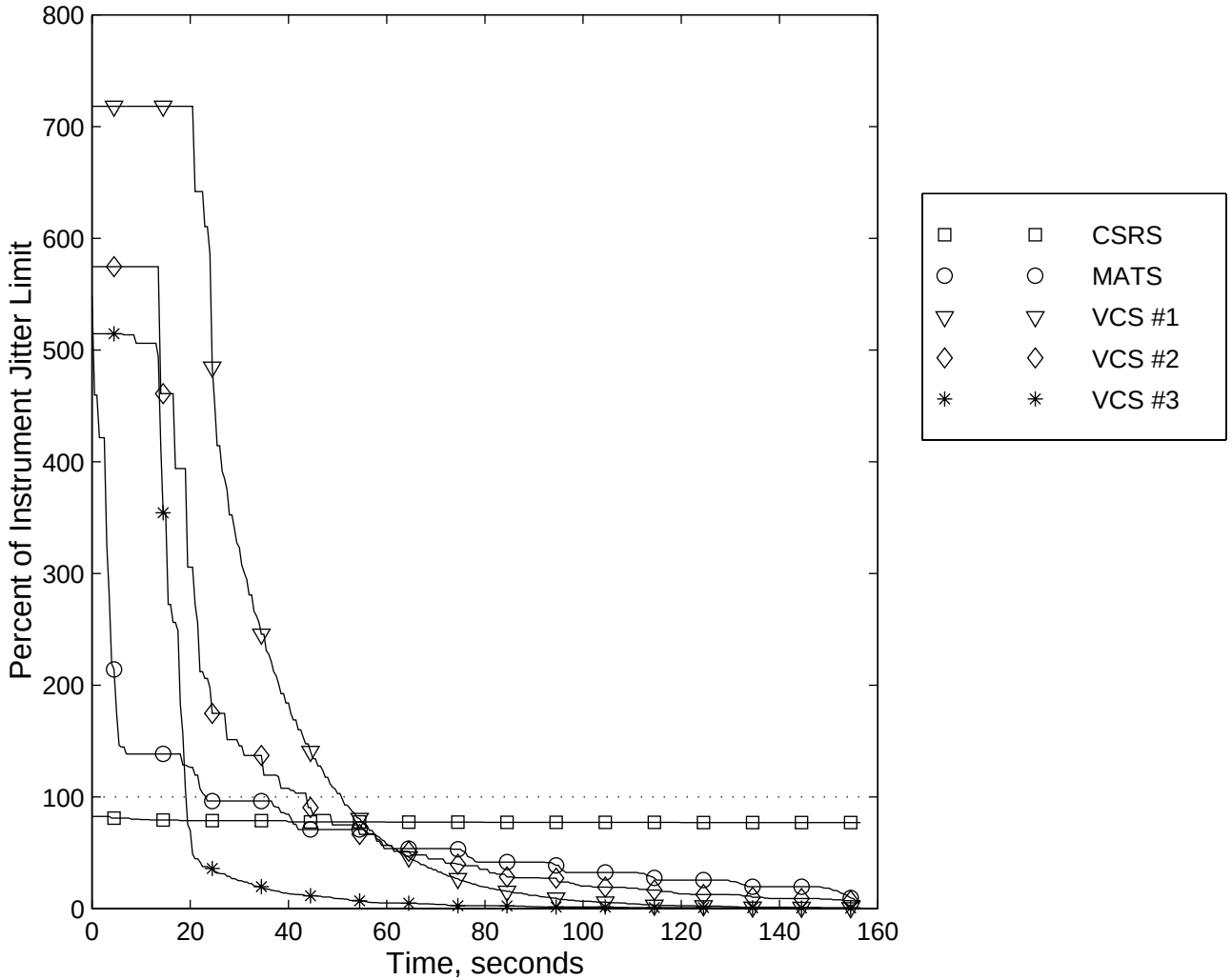

FIGURE C.7: HSI *X*-ROTATION JITTER LEVELS (0.5 SECOND WINDOW)

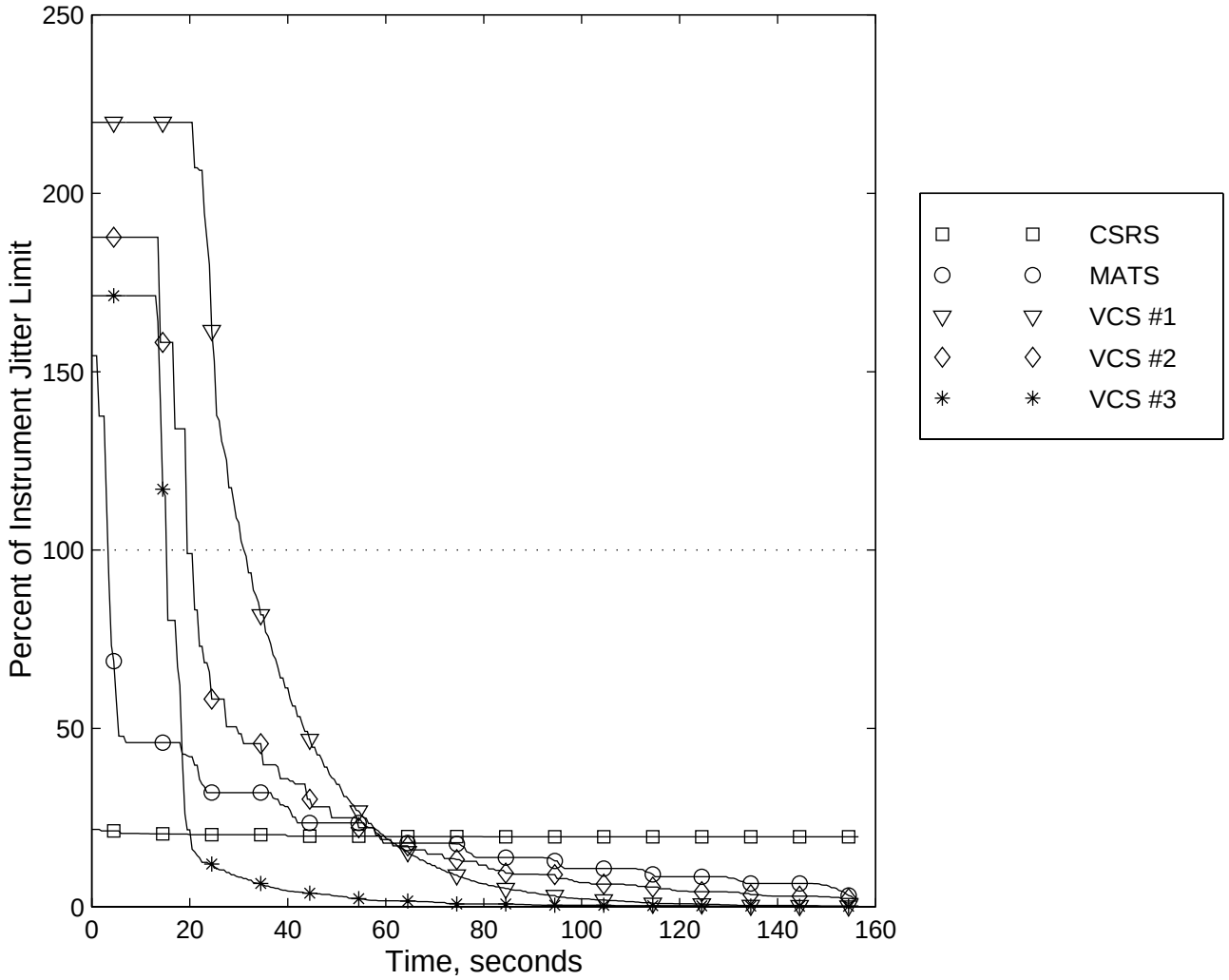

FIGURE C.8: LEISA *X*-ROTATION JITTER LEVELS (0.5 SECOND WINDOW)

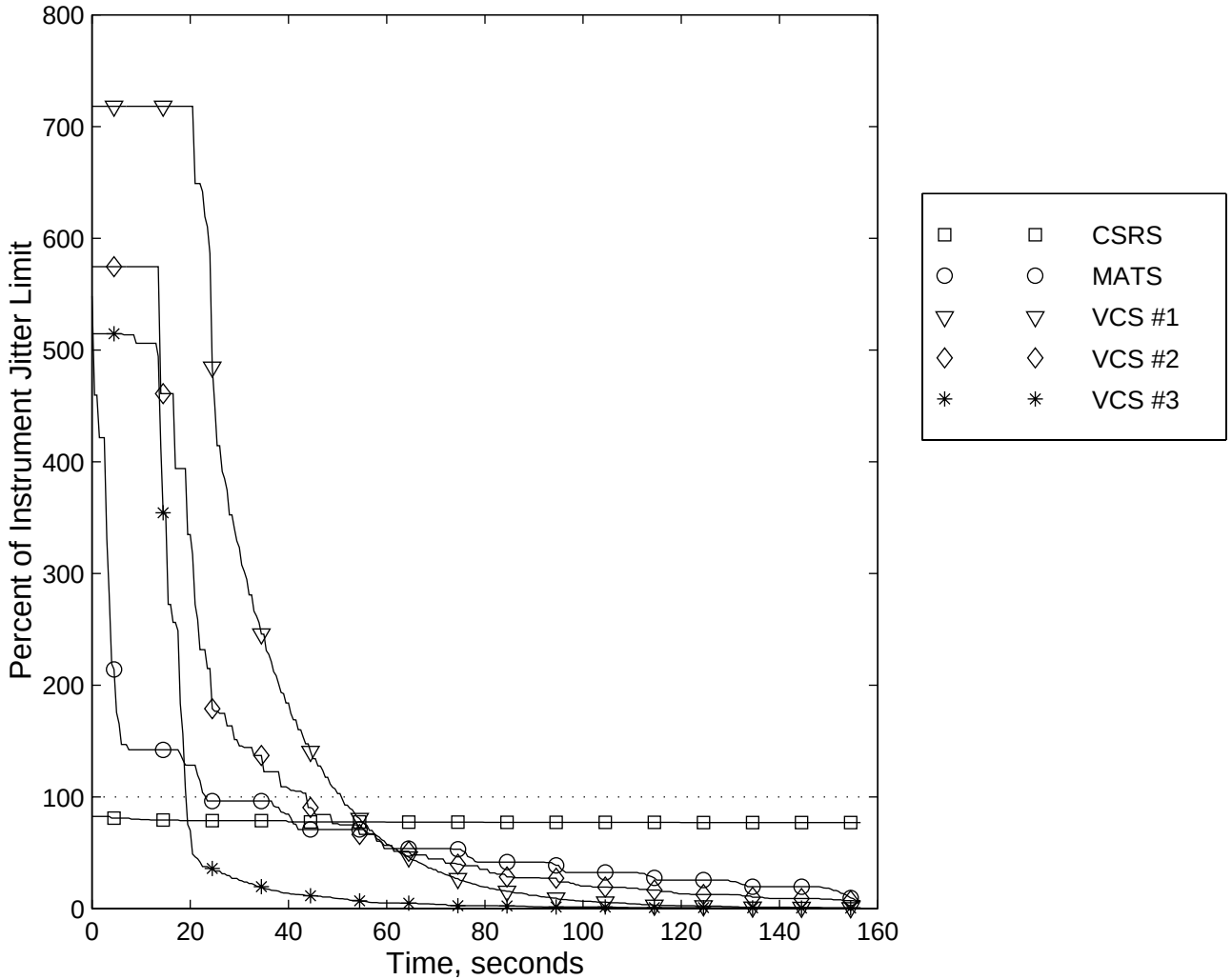

FIGURE C.9: HSI *X*-ROTATION JITTER LEVELS (1 SECOND WINDOW)

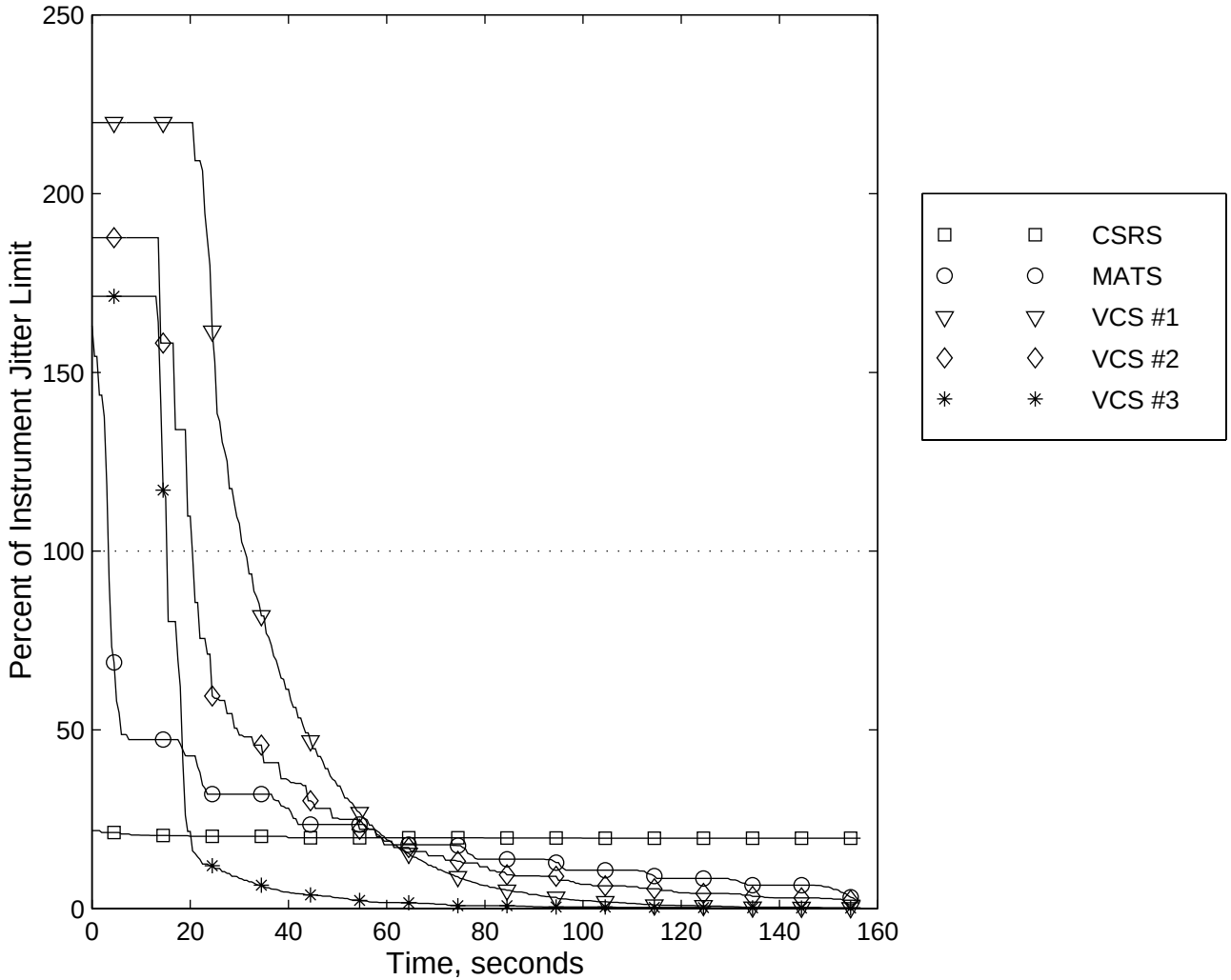

FIGURE C.10: LEISA *X*-ROTATION JITTER LEVELS (1 SECOND WINDOW)

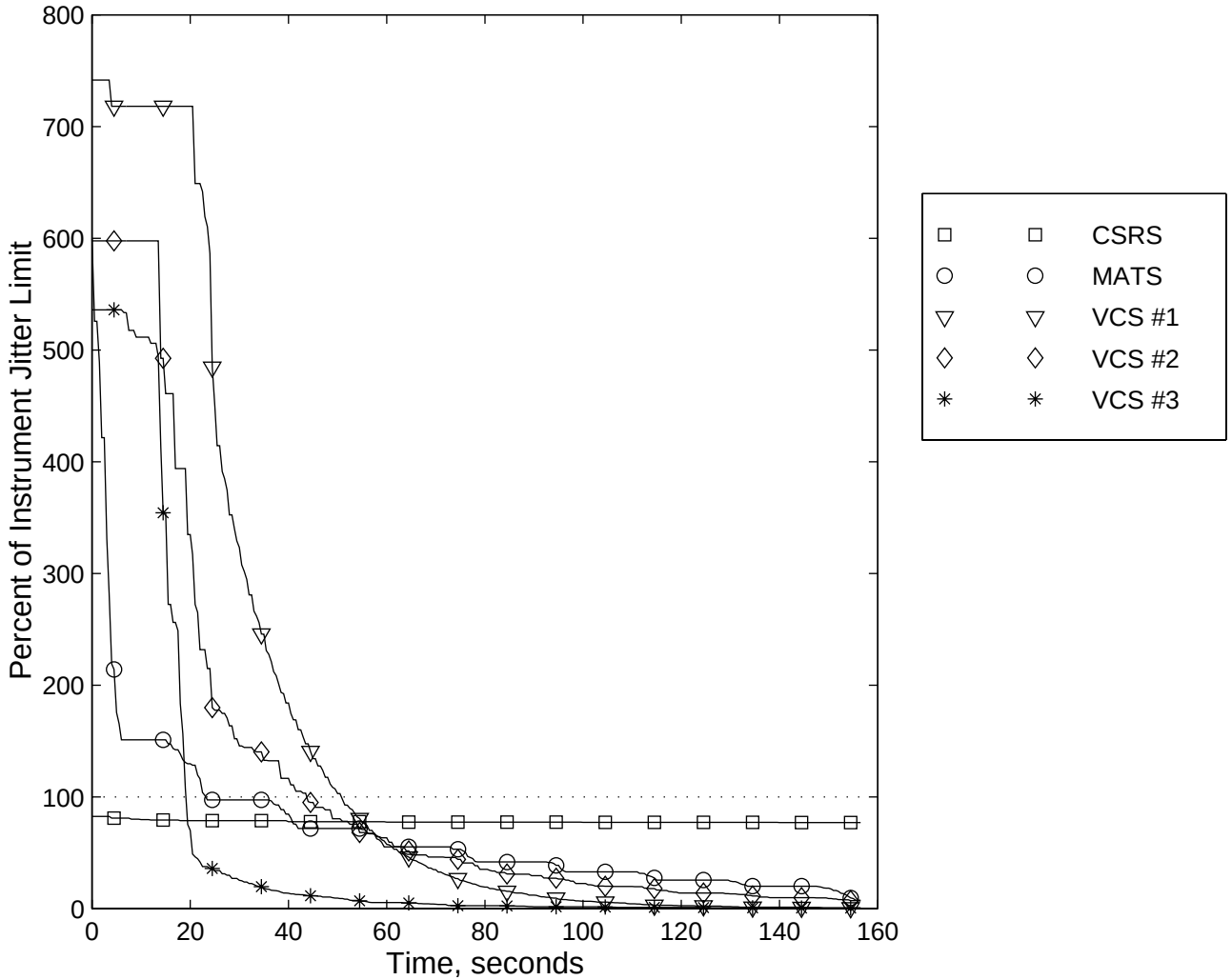

FIGURE C.11: HSI *X*-ROTATION JITTER LEVELS (3.5 SECOND WINDOW)

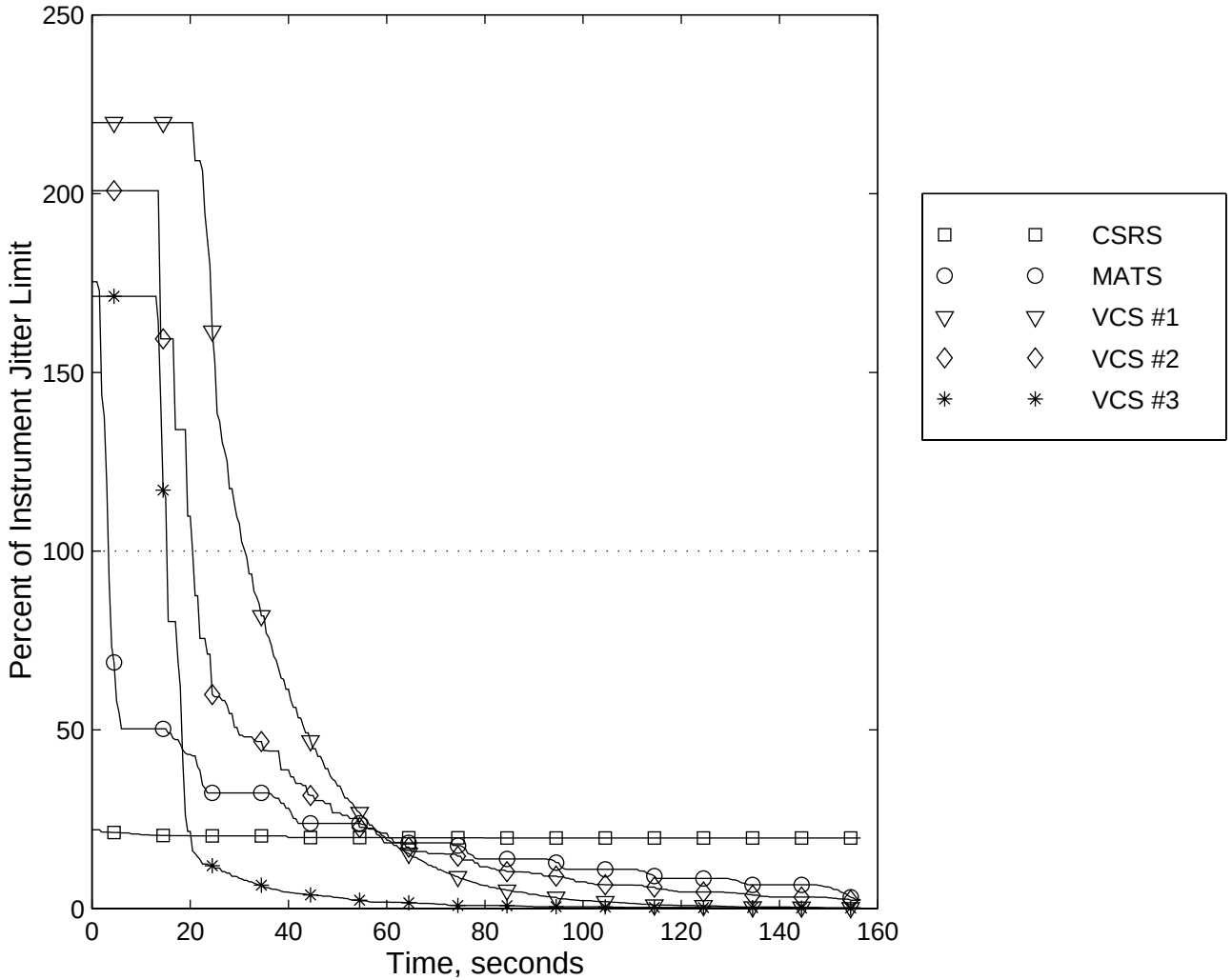

FIGURE C.12: LEISA *X*-ROTATION JITTER LEVELS (3.5 SECOND WINDOW)

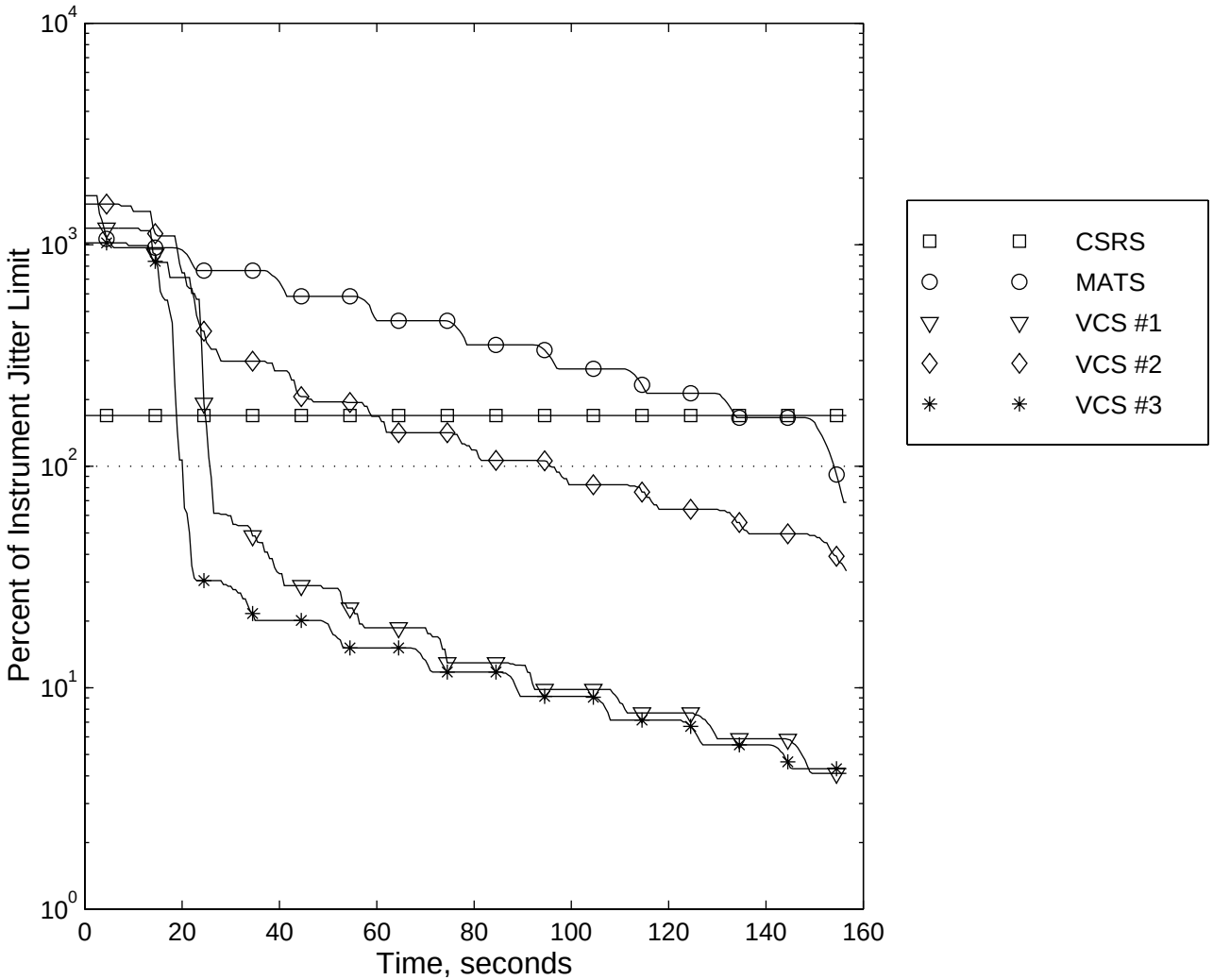

FIGURE C.13: HSI *Y*-ROTATION JITTER LEVELS (0.05 SECOND WINDOW)

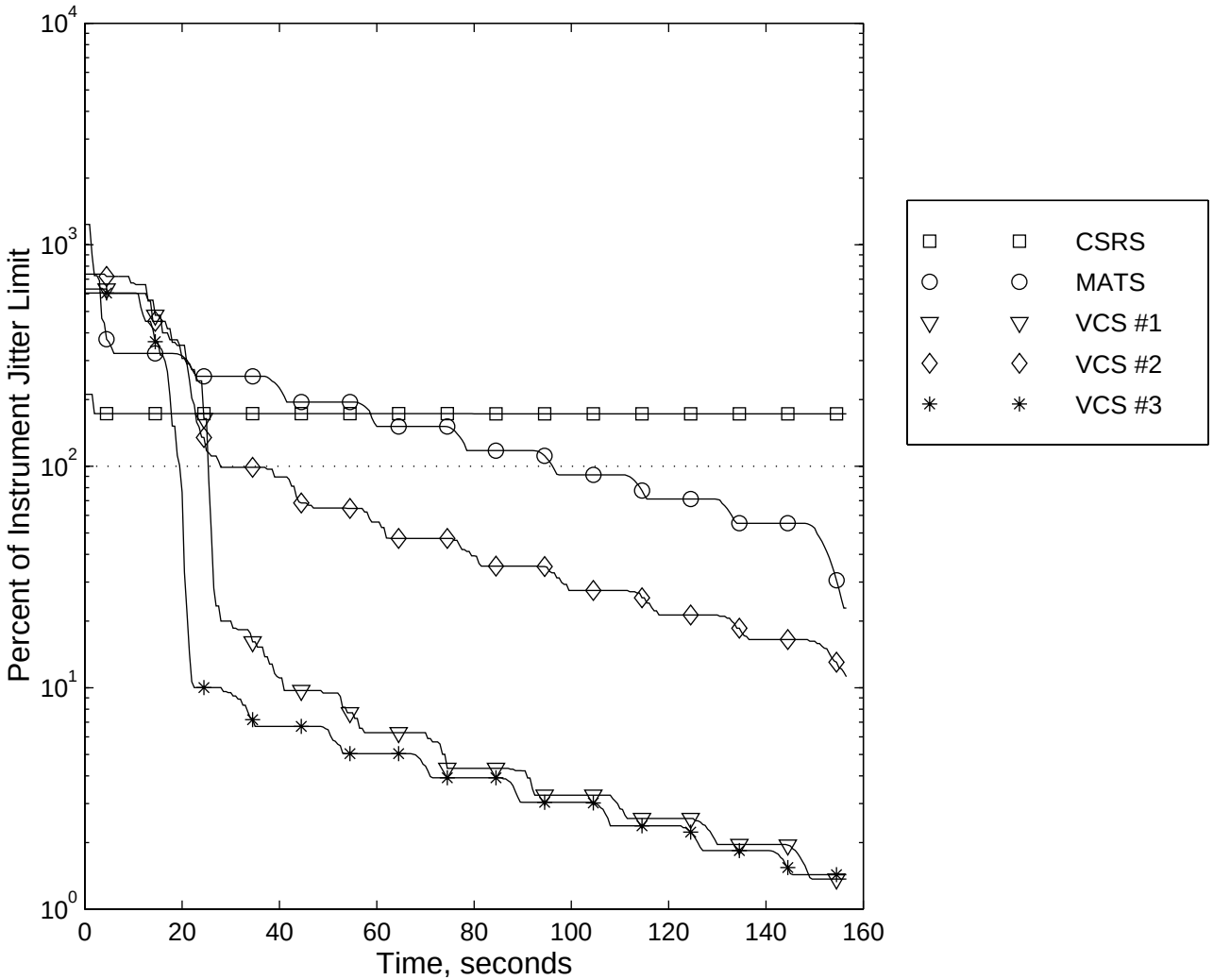

FIGURE C.14: LEISA *Y*-ROTATION JITTER LEVELS (0.05 SECOND WINDOW)

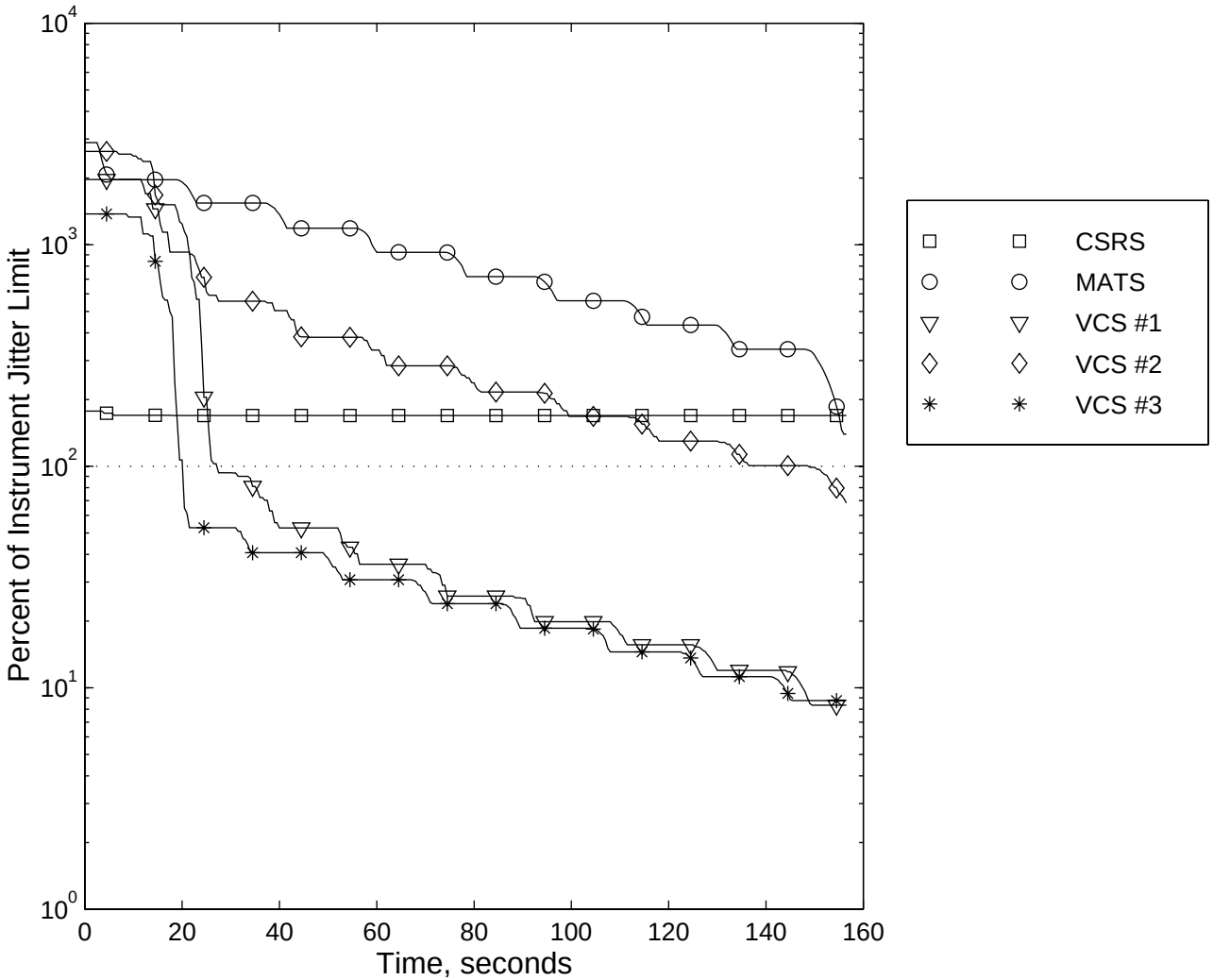

FIGURE C.15: HSI *Y*-ROTATION JITTER LEVELS (0.1 SECOND WINDOW)

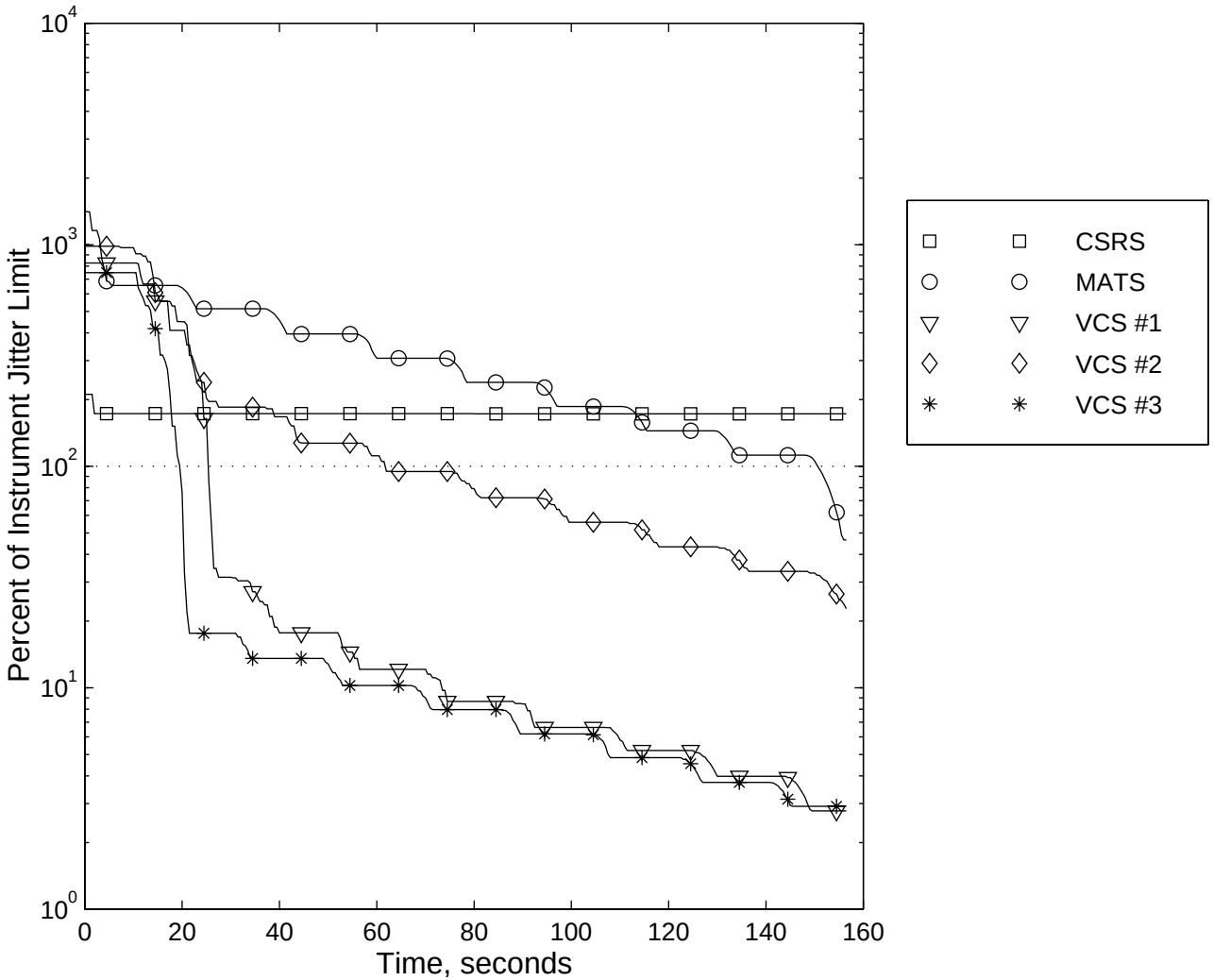

FIGURE C.16: LEISA *Y*-ROTATION JITTER LEVELS (0.1 SECOND WINDOW)

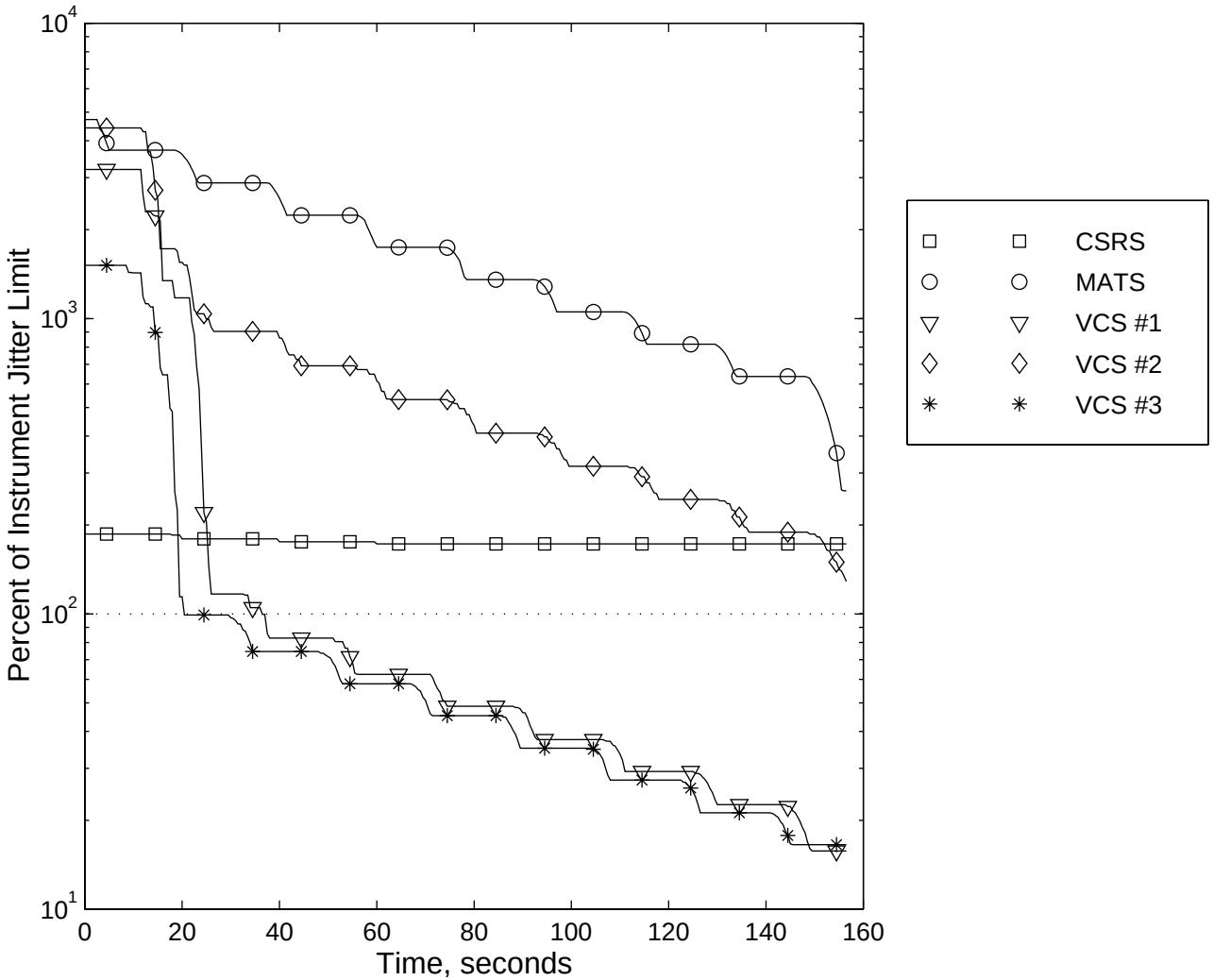

FIGURE C.17: HSI *Y*-ROTATION JITTER LEVELS (0.2 SECOND WINDOW)

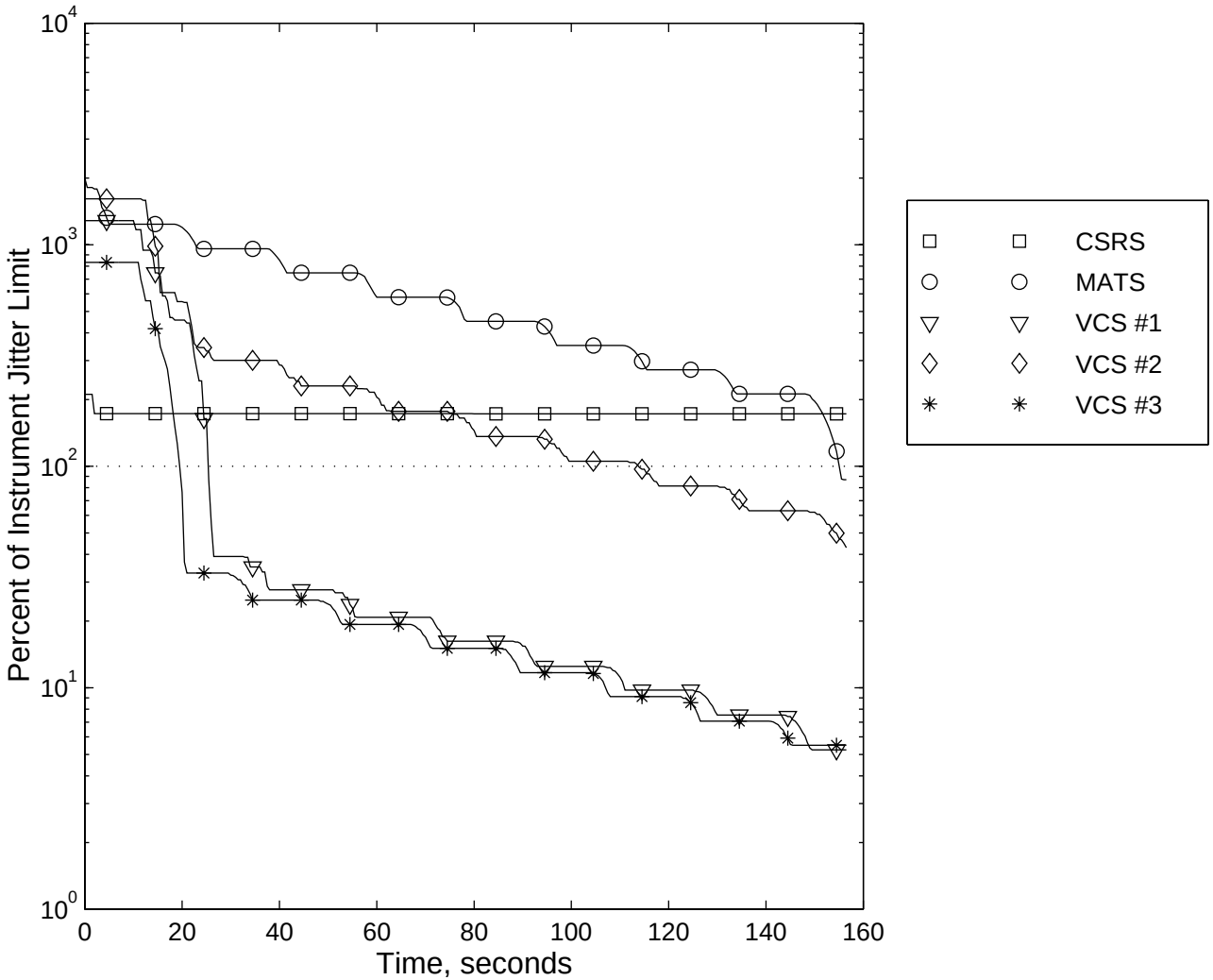

FIGURE C.18: LEISA *Y*-ROTATION JITTER LEVELS (0.2 SECOND WINDOW)

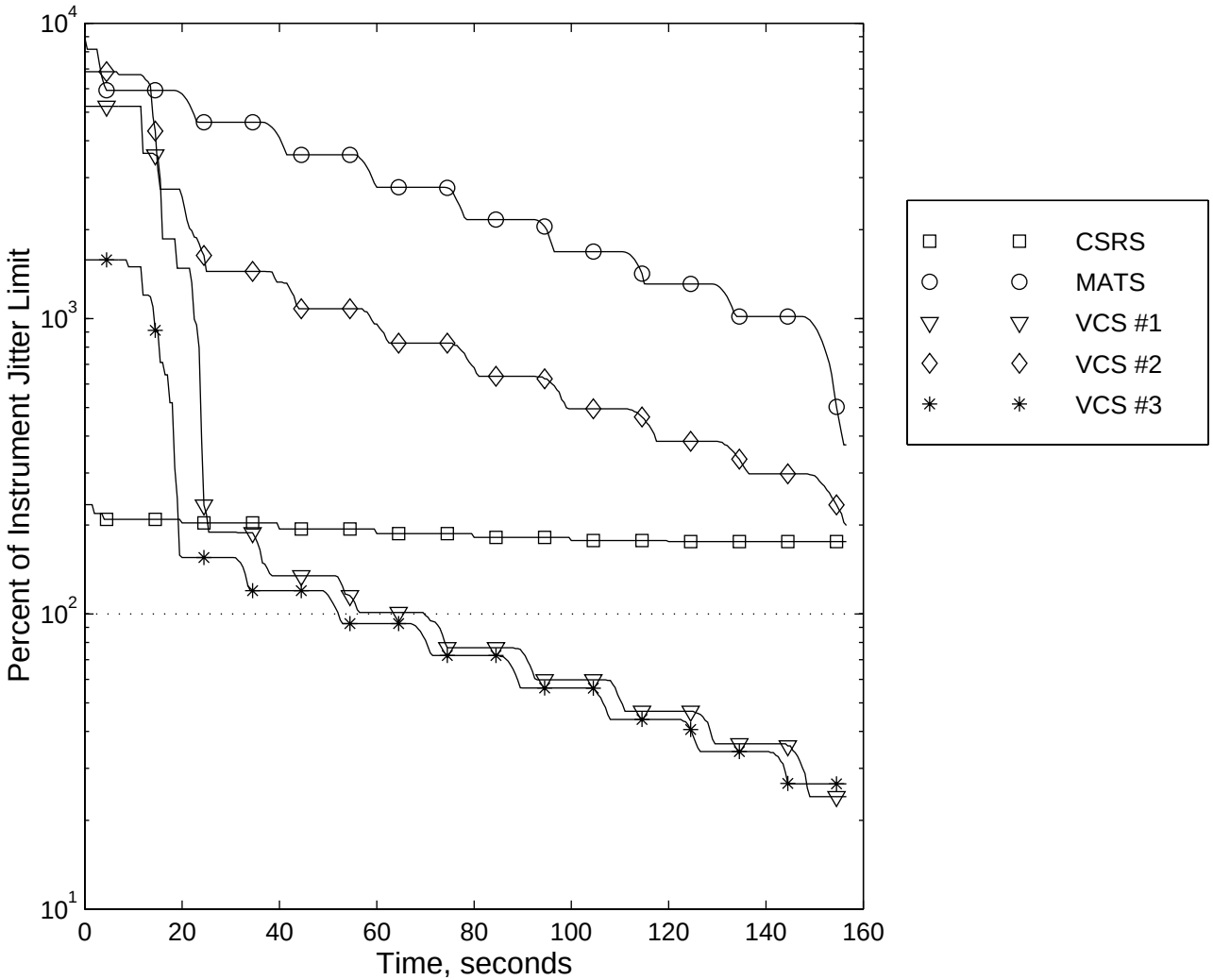

FIGURE C.19: HSI *Y*-ROTATION JITTER LEVELS (0.5 SECOND WINDOW)

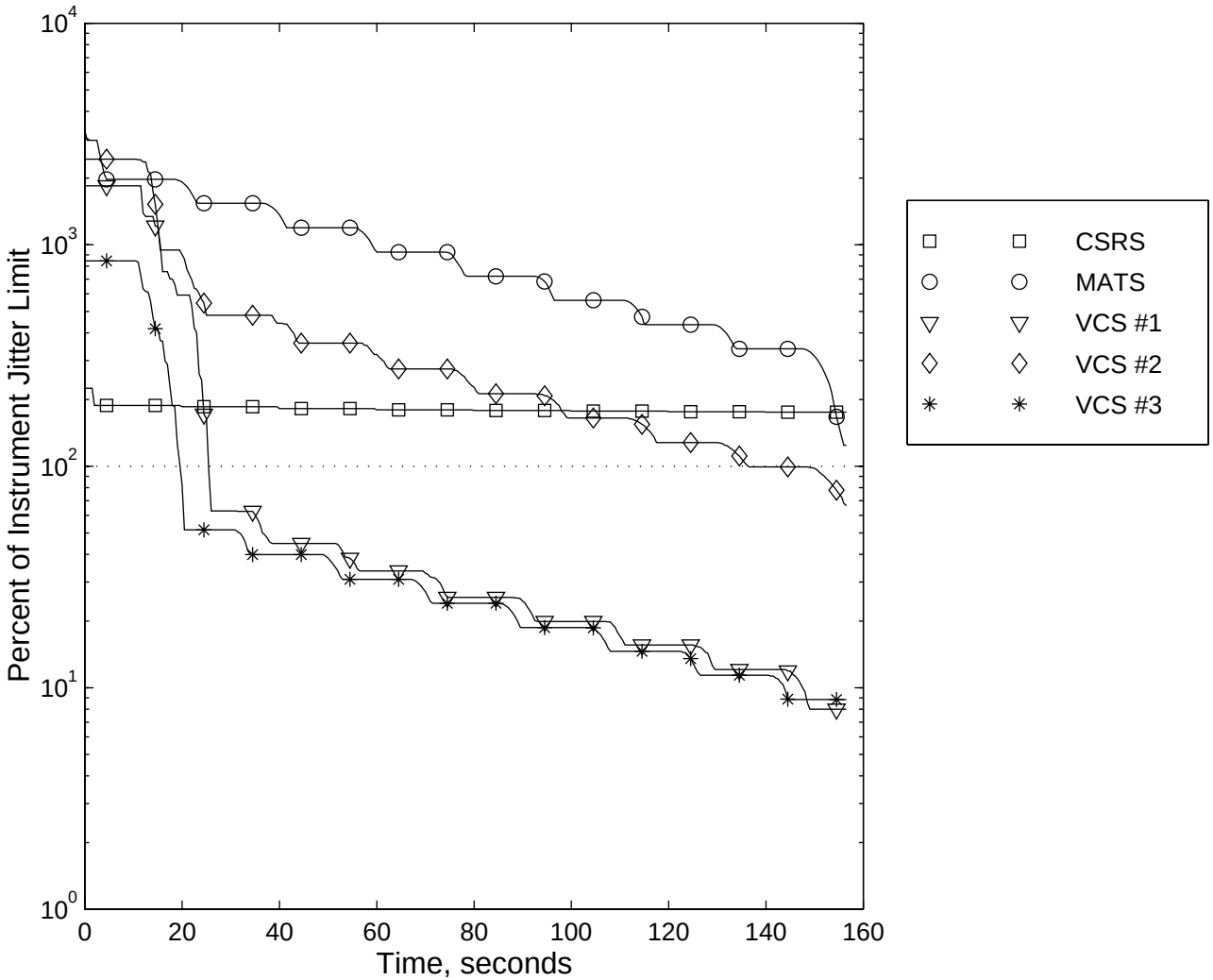

FIGURE C.20: LEISA *Y*-ROTATION JITTER LEVELS (0.5 SECOND WINDOW)

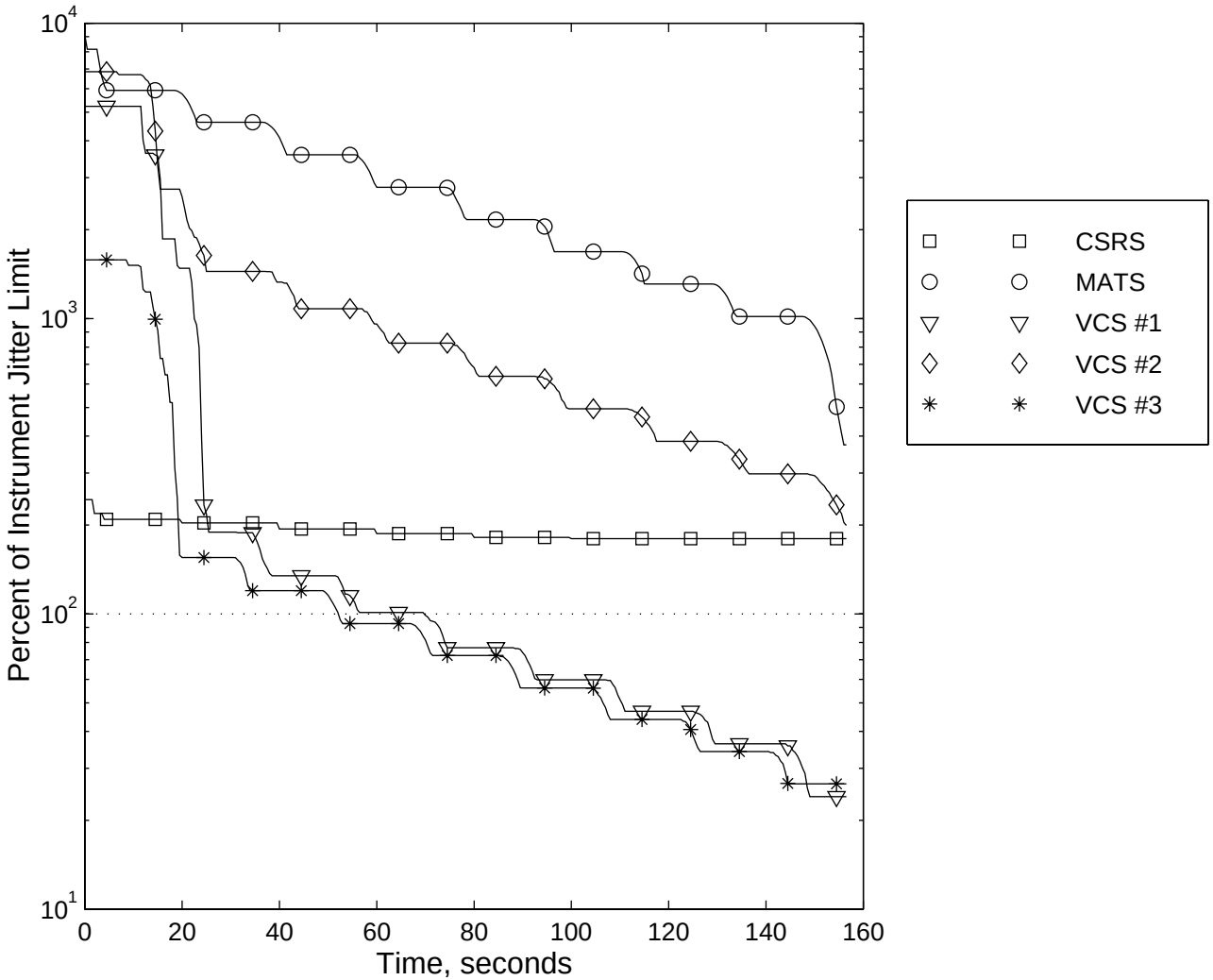

FIGURE C.21: HSI *Y*-ROTATION JITTER LEVELS (1 SECOND WINDOW)

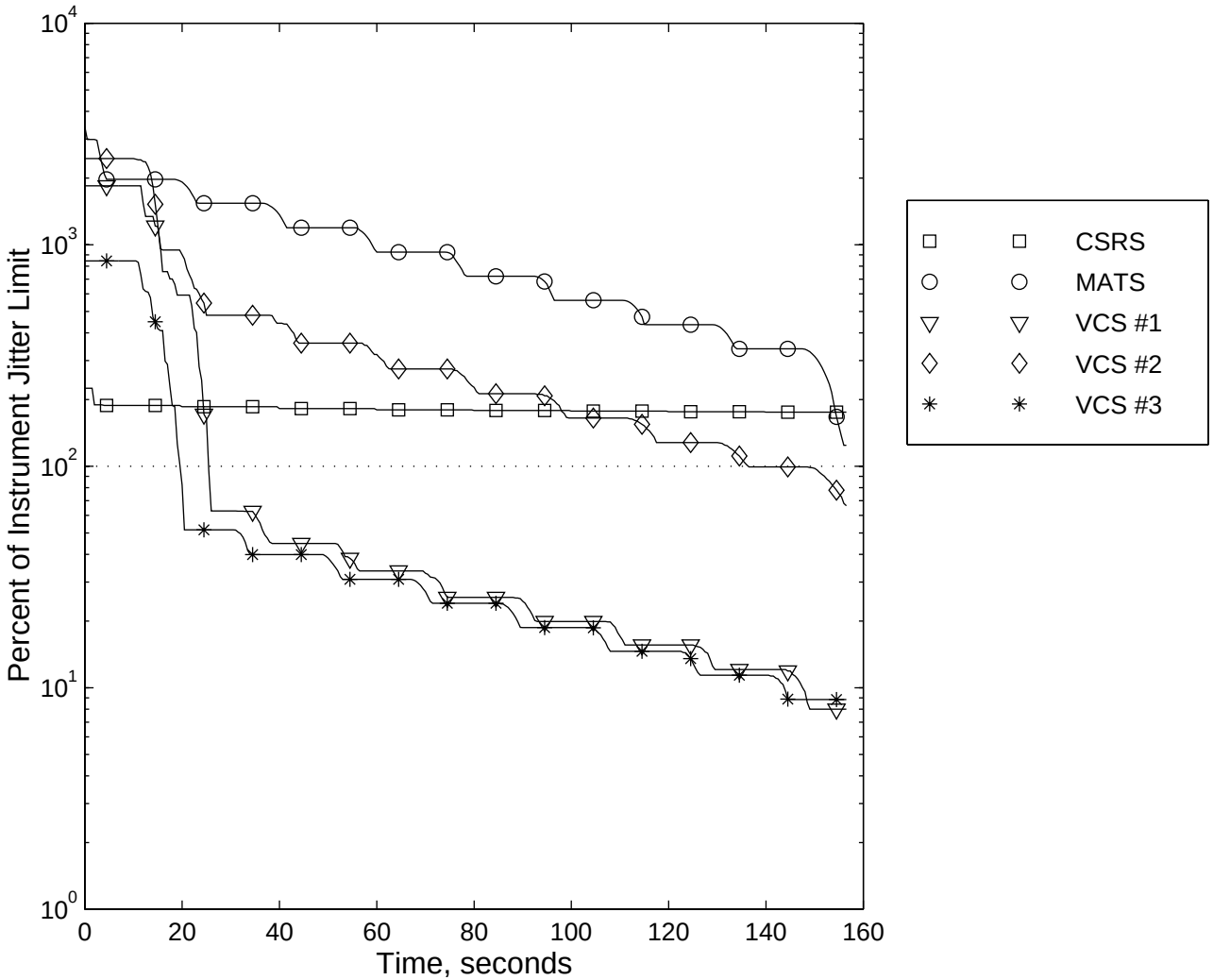

FIGURE C.22: LEISA *Y*-ROTATION JITTER LEVELS (1 SECOND WINDOW)

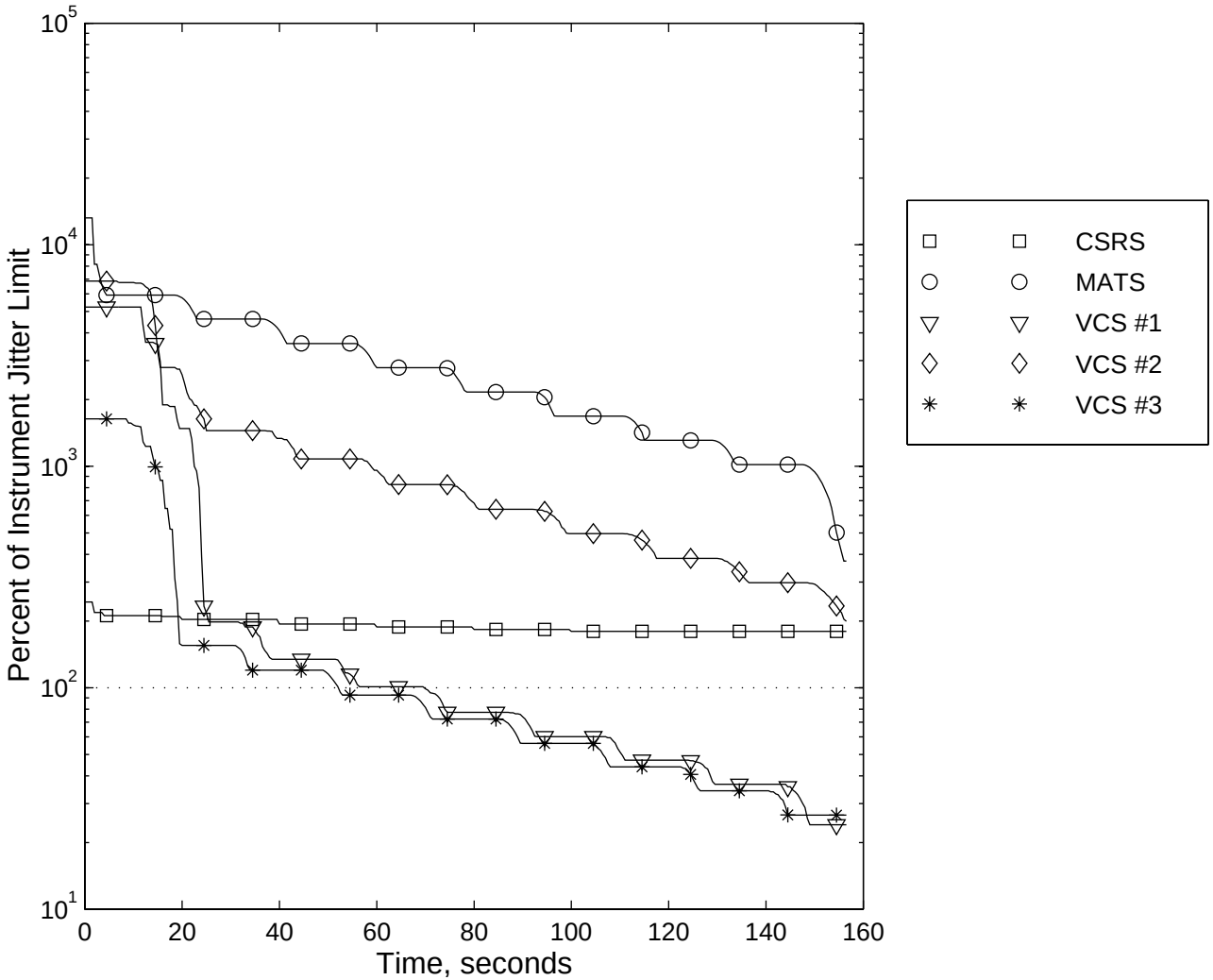

FIGURE C.23: HSI *Y*-ROTATION JITTER LEVELS (3.5 SECOND WINDOW)

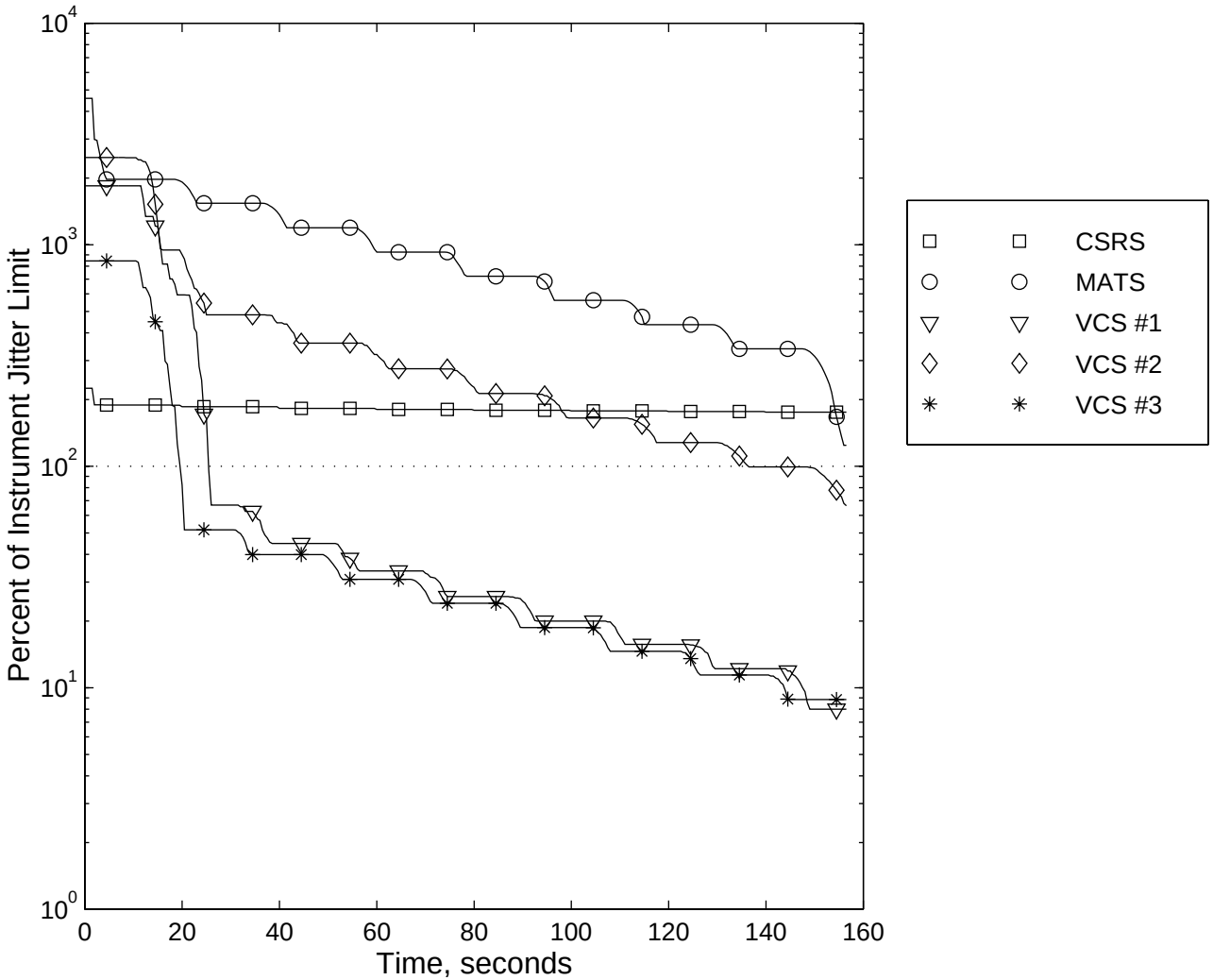

FIGURE C.24: LEISA *Y*-ROTATION JITTER LEVELS (3.5 SECOND WINDOW)

REPORT DOCUMENTATION PAGE

Form Approved
OMB No. 0704-0188

Public reporting burden for this collection of information is estimated to average 1 hour per response, including the time for reviewing instructions, searching existing data sources, gathering and maintaining the data needed, and completing and reviewing the collection of information. Send comments regarding this burden estimate or any other aspect of this collection of information, including suggestions for reducing this burden, to Washington Headquarters Services, Directorate for Information Operations and Reports, 1215 Jefferson Davis Highway, Suite 1204, Arlington, VA 22202-4302, and to the Office of Management and Budget, Paperwork Reduction Project (0704-0188), Washington, DC 20503.

1. AGENCY USE ONLY (Leave blank)

2. REPORT DATE
August 1998

3. REPORT TYPE AND DATES COVERED
Contractor Report

4. TITLE AND SUBTITLE
Input Shaping to Reduce Solar Array Structural Vibrations

5. FUNDING NUMBERS
NCC1-104

632-10-14-28

6. AUTHOR(S)
Michael J. Doherty and Robert H. Tolson

7. PERFORMING ORGANIZATION NAME(S) AND ADDRESS(ES)
The George Washington University
Joint Institute for Advancement of Flight Sciences
NASA Langley Research Center
Hampton, VA 23681-2199

8. PERFORMING ORGANIZATION REPORT NUMBER

9. SPONSORING/MONITORING AGENCY NAME(S) AND ADDRESS(ES)
National Aeronautics and Space Administration
Langley Research Center
Hampton, VA 23681-2199

10. SPONSORING/MONITORING AGENCY REPORT NUMBER
NASA/CR-1998-208698

11. SUPPLEMENTARY NOTES
The information presented in this report was submitted to the School of Engineering and Applied Science of The George Washington University in partial fulfillment of the requirements for the Degree of Master of Science, April 1998. Langley Technical Monitor: Kenny B. Elliott.

12a. DISTRIBUTION/AVAILABILITY STATEMENT
Unclassified-Unlimited
Subject Category 18 Distribution: Standard
Availability: NASA CASI (301) 621-0390

12b. DISTRIBUTION CODE

13. ABSTRACT (Maximum 200 words)
Structural vibrations induced by actuators can be minimized using input shaping. Input shaping is a feedforward method in which actuator commands are convolved with shaping functions to yield a shaped set of commands. These commands are designed to perform the maneuver while minimizing the residual structural vibration. In this report, input shaping is extended to stepper motor actuators. As a demonstration, an input-shaping technique based on pole-zero cancellation was used to modify the Solar Array Drive Assembly (SADA) actuator commands for the Lewis satellite. A series of impulses were calculated as the ideal SADA output for vibration control. These impulses were then discretized for use by the SADA stepper motor actuator and simulated actuator outputs were used to calculate the structural response. The effectiveness of input shaping is limited by the accuracy of the knowledge of the modal frequencies. Assuming perfect knowledge resulted in significant vibration reduction. Errors of 10% in the modal frequencies caused notably higher levels of vibration. Controller robustness was improved by incorporating additional zeros in the shaping function. The additional zeros did not require increased performance from the actuator. Despite the identification errors, the resulting feedforward controller reduced residual vibrations to the level of the exactly modeled input shaper and well below the baseline cases. These results could be easily applied to many other vibration-sensitive applications involving stepper motor actuators.

14. SUBJECT TERMS
Jitter; Control; Input shaping; s/c vibration; Precision pointing

15. NUMBER OF PAGES
136

16. PRICE CODE
A07

17. SECURITY CLASSIFICATION OF REPORT
Unclassified

18. SECURITY CLASSIFICATION OF THIS PAGE
Unclassified

19. SECURITY CLASSIFICATION OF ABSTRACT
Unclassified

20. LIMITATION OF ABSTRACT